UNIVERSIDADE FEDERAL DO CEARÁ
CENTRO DE CIÊNCIAS
PROGRAMA DE PÓS-GRADUAÇÃO EM QUÍMICA

RAIMUNDO NONATO FERNANDES MOREIRA FILHO

INJECTABLE HYDROGEL BASED ON NATURAL POLYMERS FOR DRUG DELIVERY AND TISSUE ENGINEERING APPLICATIONS

FORTALEZA
2024

RAIMUNDO NONATO FERNANDES MOREIRA FILHO

INJECTABLE HYDROGEL BASED ON NATURAL POLYMERS FOR DRUG DELIVERY AND TISSUE ENGINEERING APPLICATIONS

Tese apresentada ao Programa de Pós-Graduação em Química da Universidade Federal do Ceará, como requisito parcial à obtenção do título de doutor em Química. Área de concentração: Química.

Orientador: Prof.ª Dr.ª Judith Pessoa Feitosa de Andrade
Coorientador: Prof. Dr. Rodrigo Silveira Vieira

FORTALEZA

2024

Dados Internacionais de Catalogação na Publicação
Universidade Federal do Ceará
Sistema de Bibliotecas
Gerada automaticamente pelo módulo Catalog, mediante os dados fornecidos pelo(a) autor(a)

M839i Moreira Filho, Raimundo Nonato Fernandes.
Injectable Hydrogel Based on Natural Polymers for Drug Delivery and Tissue Engineering Applications / Raimundo Nonato Fernandes Moreira Filho. – 2024.
124 f. : il. color.

Tese (doutorado) – Universidade Federal do Ceará, Centro de Ciências, Programa de Pós-Graduação em Química, Fortaleza, 2024.
Orientação: Profa. Dra. Judith Pessoa Feitosa de Andrade.
Coorientação: Prof. Dr. Rodrigo Silveira Vieira.

1. Biomaterials. 2. Hydrogels. 3. Polymers. 4. Chitosan. 5. Guar gum. I. Título.

CDD 540

RAIMUNDO NONATO FERNANDES MOREIRA FILHO

INJECTABLE HYDROGEL BASED ON NATURAL POLYMERS FOR DRUG DELIVERY AND TISSUE ENGINEERING APPLICATIONS

Tese apresentada ao Programa de Pós-Graduação em Química da Universidade Federal do Ceará, como requisito parcial à obtenção do título de Doutor em Química.

Aprovada em: 12/11/2024.

BANCA EXAMINADORA

Prof.ª Dra. Jeanny da Silva Maciel
Universidade Federal do Ceará (UFC)

Prof.ª Dra. Pablyana Leila Rodrigues da Cunha
Universidade Federal do Ceará (UFC)

Dr. Francisco Fabio Pereira de Souza
Universidade Federal do Ceará (UFC)

Prof.ª Dra. Mariana Agostini de Moraes
Universidade Estadual de Campinas (Unicamp)

AGRADECIMENTOS

O presente trabalho foi realizado com apoio da Coordenação de Aperfeiçoamento de Pessoal de Nível Superior – Brasil (CAPES), Código de Financiamento 001.

Agradeço à Profa. Dra. Judith Pessoa Feitosa de Andrade, pela orientação, pela confiança depositada em meu trabalho e pela oportunidade de integrar seu grupo de pesquisa. Ao Prof. Dr. Rodrigo Silveira Vieira, pela coorientação, pela disponibilidade e pelas valiosas contribuições ao longo de todas as etapas deste estudo.

Aos colegas dos laboratórios, pelas discussões produtivas, pelas críticas construtivas e pelo constante apoio durante o desenvolvimento desta pesquisa.

RESUMO

Hidrogéis injetáveis emergem como materiais promissores na biomedicina, devido às suas propriedades únicas, como alto teor de água e semelhança estrutural com a matriz extracelular, além da capacidade de serem aplicados *in situ*, otimizando tratamentos médicos. Nos últimos anos, o desenvolvimento de hidrogéis baseados em polímeros naturais tem ganhado destaque, impulsionado pela busca por materiais mais biocompatíveis e funcionais. Neste contexto, o presente trabalho investigou o potencial de um hidrogel injetável baseado em quitosana e goma guar, ambos modificados quimicamente para melhorar suas propriedades funcionais. Foram avaliadas diferentes formulações de hidrogéis compostos por *N*-succinil quitosana (NSQ) e goma guar oxidada (GGOx) para aplicações biomédicas específicas. Os sistemas foram caracterizados detalhadamente quanto às suas propriedades químicas, físicas e morfológicas. Inicialmente, estudou-se o impacto da reticulação devido a variação dos grupos funcionais entre as macromoléculas na biodegradabilidade e biocompatibilidade. Posteriormente, lidocaína foi incorporada na formulação mais promissora (75:25 NSC:GMOx) para a liberação controlada do fármaco, visando o desenvolvimento de um sistema eficaz para alívio de dores em pacientes no pós-operatório de cirurgias musculoesqueléticas, com resultados que demonstraram uma liberação prolongada de lidocaína. Por fim, uma terceira formulação com nanofibras de celulose bacteriana (NCB) incorporadas ao hidrogel NSQ/GGOx objetivando melhorar suas propriedades mecânicas para aplicações em engenharia de tecidos foi explorada. Ensaios de intumescimento, reologia e estresse-relaxamento demonstraram uma melhoria significativa na estabilidade e nas propriedades mecânicas do novo material. Todos resultados indicaram o grande potencial dos hidrogéis de NSQ/GGOx para uma ampla gama de aplicações biomédicas, especialmente na liberação controlada de fármacos e na engenharia de tecidos.

Palavras-chave: biomateriais; hidrogéis; polímeros; quitosana; goma guar.

ABSTRACT

Injectable hydrogels have emerged as promising materials in biomedicine due to their unique properties, such as high-water content and similarity to the extracellular matrix, along with the advantage of in situ application via syringes, which optimizes treatment. In recent years, research has intensified in the pursuit of developing and enhancing polymeric materials suitable for injectable hydrogels, with a focus on natural polymers. In this context, the present work explored the potential of an injectable hydrogel based on chitosan and guar gum, both chemically modified. Different formulations of hydrogels composed of *N*-succinyl chitosan (NSC) and oxidized guar gum (OxGG) were evaluated for specific biomedical applications. All systems were extensively characterized in terms of chemical, physical, and morphological aspects. Initially, the impact of cross-linking concentration between the macromolecules on the material's properties was studied, focusing on biodegradability and biocompatibility. Subsequently, lidocaine was incorporated into the most promising formulation to investigate controlled drug release, aiming to develop an effective system for pain relief in patients after musculoskeletal surgeries, with results demonstrating prolonged lidocaine release. Finally, to enhance the mechanical properties of the hydrogel composed of NSC and OxGG for tissue engineering applications, bacterial cellulose nanofibers (BCF) were added to the formulation, which, through rheological and compressibility tests, showed significant improvement in the material's stability and mechanical properties. The results demonstrated the high potential of this system for various biomedical applications, especially in drug delivery and tissue engineering.

Keywords: biomaterials; hydrogels; polymers; chitosan; guar gum.

LISTA DE FIGURAS

Figure 1 — Graphs of clinical trials using injectable hydrogels worldwide……. 14
Figure 2 — Schematic representation of the phases of this work…….…….. 16
Figure 3 — Schiff base reaction formation mechanism……..…….. 22
Figure 4 — Chitosan succinylation reaction with succinic anhydride…… 25
Figure 5 — Chemical structure of guar gum (galactomannan)…….. 26
Figure 6 — Oxidation reaction guar gum using sodium periodate……..……. 27
Figure 7 — Chemical structure of cellulose chain…… 28
Figure 8 — Graphs showing plasma concentration of different drug treatment apllications over time……..…….. 30
Figure 9 — Schematic representation of the direct cell viability……..... 44
Figure 10 — Samples of 75C25G hydrogels prepared for the compressibility assay……... 45
Figure 11 — ^{1}H NMR spectrum of NSC at 25°C in D_2O/DCl…… 46
Figure 12 — Titration graph using volume of NaOH 1 mol/L…… 47
Figure 13 — GPC curve for GM and OxGM solution in 0.1 mol/L $NaNO_3$……. 48
Figure 14 — FTIR spectra of NSC, OxGM, 75C25G, 50C50G and 25C75G…. 49
Figure 15 — HR C 1s XPS spectrum of NSC, OxGM, 75C25G, 50C50G, and 25C75G samples……..……. 51
Figure 16 — Thermogravimetric analysis (A) and derived weight (B) of NSC, OxGM, and (75C25G, 50C50G and 25C75G) hydrogels under synthetic air……..……... 52
Figure 17 — Evolution of storage (G') and loss (G'') modulus over time……..…. 54
Figure 18 — Swelling behaviors of the NSC/OxGM hydrogels with different polymer ratios in PBS buffer (0.01 M and pH 7.4)…….…… 56
Figure 19 — Weight loss (%) related to the degradation of the different freeze-dried hydrogels in PBS and PBS/Lysozyme (*) over 28 days…….. 57
Figure 20 — SEM images of different volumetric ratios of NSC/OxGM during the degradation process in PBS/Lysozyme media (4.0 kV, 500 µm)……..…….. 59
Figure 21 — Pore size distribution for the different ratios of the freeze-dried hydrogels…… 60
Figure 22 — Cell viability of the L929 fibroblasts cells when co-cultured with the

studied hydrogels for 24 and 48 h (in % compared to DMEM control, n= 4) (*p < 0.05)…… 62
Figure 23 — Direct cell viability of the nHDF fibroblasts (in % compared to DMEM control, n= 4) (*p < 0.05)…….…... 63
Figure 24 — Relative cell population growth based on the cells at day 1 (24h)….. 64
Figure 25 — Representative compressive stress-strain curve for 75C25G hydrogels…… 65
Figure 26 — Self-healing behavior of 75C25G hydrogels…….. 66
Figure 27 — Chemical structure of lidocaine molecule…….. 70
Figure 28 — Graphical abstract of the studied injectable hydrogel being used as drug delivery carrier…… 72
Figure 29 — Pictures illustrating the *in vitro* experimental release system……. 75
Figure 30 — FTIR of hydrogel (NSCOxGM), lidocaine (LD), and lidocaine loaded hydrogel (NSCOxGM+LD)…….. 76
Figure 31 — TGA of hydrogel (NSCOxGM), lidocaine (LD) and lidocaine loaded hydrogel (NSCOxGM+LD)…….. 77
Figure 32 — SEM images of NSC-OxGM hydrogel magnitude 350x (a), 2000x (b); and NSC-OxGM/LD hydrogel magnitude 350x (c) and 2000x (d)……..…… 78
Figure 33 — Sustained-release profile of lidocaine from NSC-OxGM hydrogels according to initial mass (%) in 37 °C PBS solution….. 80
Figure 34 — Release profile data (dots) and Korsmeyer-Peppas model (red line). The model was obtained using OriginPro with the parameters shown in the table…… 80
Figure 35 — Cell viability of L929 in contact with the extractive of the materials. 81
Figure 36 — Schematic representation of a bacterial cellulose reinforced-hydrogel based on *N*-succinyl chitosan and dialdehyde galactomannan…….…… 86
Figure 37 — Schematic representation of the BCF fabrication…….. 88
Figure 38 — Illustrations of the BCF suspension in NSC solution before and after the ultrasonic crush process…… 89
Figure 39 — FTIR spectrum of NSC, OxGG, BCF, NSC/OxGG, and NSC/OxGG/BCF…….. 94

Figure 40 — C 1s spectra of NSC, OxGG, BCF, NSCOxGG, and NSCOxGGBCF……. 96
Figure 41 — TGA of the biopolymers NSC, OxGG, BCF, NSCOxGG, and NSCOxGGBCF……. 97
Figure 42 — TGA and DGA of freeze-dried NSC/OxGG, and NSC/OxGG/BCF hydrogels…… 98
Figure 43 — SEM imagens of NSC/OxGG and NSC/OxGG/BCF…….. 99
Figure 44 — Swelling capacity of NSC/OxGG and NSC/OxGG/BCF hydrogels in PBS at 37 ºC. The data are presented as mean ± standard deviation (n = 3)……. 100
Figure 45 — Shear storage (G') and loss (G'') modulus as a function of time for NSC/OxGM (orange) and NSC/OxGM/BCF (cyano)……. 102
Figure 46 — Storage modulus (G') NSCOxGG and NSCOxGGBCF hydrogels over time……. 103
Figure 47 — (A) Initial stress-strain curves and (B) Young's Modulus values of NSC/OxGG and NSC/OxGG/BCF hydrogels…… 104
Figure 48 — (A) Stress/Strain and (B) Stress/Time curves of the NSC/OxGG and NSC/OxGG/BCF hydrogels…… 105
Figure 49 — Cell viability of nHDF cultured with different time extracts from NSC/OxGG and NSC/OxGG/BCF hydrogels. Data are presented as mean ± standard deviation. Statistical significance is indicated as *p < 0.05; **p < 0.01…… 107
Figure 50 — Microscopic images of the fibroblast cultivated with different time extractives NSC/OxGG and NSC/OxGG/BCF hydrogels…… 108

LISTA DE TABELAS

Table 1 — Summary of chitosan-based hydrogels as biomaterial in the literature .. 24

Table 2 — Different transport exponent ‘n’ related to geometric characteristics and release mechanism…… 31

Table 3 — Composition of the studied hydrogels and their ratio of functional groups…… 39

Table 4 — Values of Ve and MM for GM and OxGM…….. 48

Table 5 — Atomic composition of biopolymers NSC, OxGG, and hydrogels 75C25G, 50C50G, and 25C75G obtained through XPS…… 50

Table 6 — Thermal events of NSC, OxGM, 75C25G, 50C50G, and 25C75G according to temperature range (ºC) and mass loss (%)…….…….. 53

Table 7 — Porosity and average pore size, determined by liquid displacement and measured by ImageJ® software, respectively…… 62

Table 8 — Summary of the reported natural polymer-based injectable hydrogels for local anesthetic delivery system……... 72

Table 9 — Atomic composition of biopolymers NSC, OxGG, BCF, and hydrogels NSCOxGG, and NSCOxGGBCF obtained through XPS…… 97

Table 10 — Thermal events of NSC, OxGM, BCF, NSCOxGG, and NSCOxGGBCF according to temperature range (ºC) and mass degradation (%)……. 99

SUMÁRIO

1 GENERAL INTRODUCTION 13
2 GENERAL OBJECTIVES 17
2.1 Specific objectives 17
3 LITERATURE REVIEW 19
3.1 Biomaterials and biomedical devices 19
3.2 Biocompatibility and biodegradability of biomaterials 19
3.3 Injectable hydrogels 20
3.4 Polymeric biomaterials 22
3.4.1 Chitosan and N-succinyl chitosan 23
3.4.2 Guar Gum and Oxidized guar gum 26
3.4.3 Bacterial cellulose nanofibers 27
3.5 Drug delivery system 29
3.6 Biomaterials in Tissue engineering 31
CHAPTER 1: IMPACT OF THE CROSSLINKING DEGREE ON CHITOSAN / GUAR GUM-BASED INJECTABLE HYDROGELS 33
ABSTRACT 33
1 INTRODUCTION 34
2 MATERIALS AND METHODS 36
2.1 MATERIALS 36
2.2 Synthesis of *N*-succinyl chitosan 36
2.2.1 Determination of degree of substitution (DS) 37
2.3 Oxidation of galactomannan 37
2.3.1 Degree of oxidation and molar mass for galactomannan 38
2.4 Preparation of the NSC/OxGM hydrogels 39
2.5 Fourier Transform infrared spectroscopy (FTIR) 39
2.6 X-Ray Photoelectron Spectroscopy 40
2.7 Thermogravimetric analysis (TGA) 40
2.8 Gelation time via rheology 40
2.9 Evaluation of swelling behavior 41
2.10 *In vitro* biodegradation study 41
2.11 Morphology and porosity 42
2.12 Indirect cell viability 42

3 RESULTS AND DISCUSSION 46
3.1 NMR of *N*-succinyl chitosan 46
3.2 Degree of oxidation and molar mass of OxGM 47
3.3 Fourier Transform infrared (FTIR) spectroscopy 48
3.4 X-Ray Photoelectron Spectroscopy 49
3.5 Thermogravimetric analysis (TGA) 52
3.6 Gelation time via rheology 53
3.7 Evaluation of swelling degree 55
3.8 *In vitro* biodegradation study 56
3.9 Morphology and porosity 58
3.10 Indirect cell viability 61
3.11 Direct cell viability 62
3.12 Mechanical properties of hydrogels 64
4 CONCLUSION 67
CHAPTER 2: LIDOCAINE RELEASE FROM INJECTABLE HYDROGEL BASED ON CHITOSAN / GUAR GUM FOR POSTOPERATIVE PAIN MANAGEMENT 68
ABSTRACT 68
1 INTRODUCTION 69
2 MATERIALS AND METHODS 73
2.1 Materials 73
2.2 Hydrogel formulation 73
2.3 FTIR and TGA of lidocaine-loaded hydrogels 74
2.4 Scanning Electronic Microscopy (SEM) 74
2.5 *In vitro* lidocaine release 74
2.6 Cytotoxicity 75
3 RESULTS AND DISCUSSION 76
3.1 FTIR and TGA of lidocaine-loaded hydrogel 76
3.2 Morphology and Porosity 77
3.3 *In vitro* drug release 79
3.4 Cell viability 81
4 CONCLUSION 82
CHAPTER 3: INJECTABLE HYDROGEL BASED ON CHITOSAN / GUAR GUM REINFORCED WITH BACTERIAL CELLULOSE NANOFIBER FOR TISSUE ENGINEERING 83

ABSTRACT.....83
1 INTRODUCTION.....84
2 MATERIALS AND METHODS.....87
2.1 Materials.....87
2.2 Bacterial cellulose nanofiber fabrication.....87
2.3 Nanocomposite hydrogel fabrication.....88
2.4 Fourier Transform Infrared (ATR-FTIR).....89
2.5 X-ray Photon Spectrum (XPS).....90
2.6 Thermogravimetric analysis (TGA).....90
2.7 Scanning Electron Microscopy (SEM).....90
2.8 Swelling capacity.....91
2.9 Rheological behavior.....91
2.10 Stress-Relaxation Assay.....91
2.11 Indirect cell viability.....92
2.12 Statistical analysis.....93
3 RESULTS AND DISCUSSION.....94
3.1 Fourier Transform Infrared (ATR-FTIR).....94
3.2 X-ray Photon Spectrum (XPS).....95
3.3 Thermogravimetric analysis (TGA).....97
3.4 Scanning Electron Microscopy (SEM).....98
3.5 Swelling capacity.....100
3.6 Rheological behavior.....101
3.7 Stress-relaxation assay.....103
3.8 Cell viability.....106
4 CONCLUSION.....109
REFERENCE.....110
APPENDIX A.....124

1 GENERAL INTRODUCTION

Injectable hydrogels are highly attractive class of biomaterials, representing one of the most extensively investigated and versatile technologies in numerous biomedical applications such as drug delivery and tissue engineering. Their versatility arises from their tunable structure, a feature that is possible due to significant advancements in materials engineering, polymer science, and chemistry. These ongoing developments continually introduce novel polymers, innovative crosslinking method, diverse hydrogel fabrication strategies, and new applications for improving healthcare.

Since their first practical application in the 1960s, injectable hydrogels have been employed in several fields of biomedical sciences. Over the past half-century, they have transitioned from experimental use to widespread industrial applications. Today, numerous hydrogel-based products are available on the market, offering a broad spectrum of functionalities, ranging from drug delivery systems and wound dressings to cancer treatment modalities and tissue engineering scaffolds (Cascone; Lamberti, 2020).

The global hydrogel market data reflects this growth, with a valuation of USD 26 billion in 2022, and it is projected to reach USD 48.12 billion by 2032, growing at a compound annual growth rate (CAGR) of 6.40% from 2023 to 2032 (Precedence Research). This expansion is mainly driven by the increasing consumption of personal care and hygiene products, as well as the growing demand for advanced biomedical applications.

Figure 1 shows an overview of clinical trials that mentioned a hydrogel. In total, 425 trials were conducted, with 202 of them focused on hydrogels used in soft contact lenses. After excluding these, 223 trials remained, addressing a broad spectrum of medical applications. These trials were categorized based on their use of hydrogels: those employing hydrogels as tissue substitutes or mechanical supports to augment existing tissues ("Regen Tissue") were analyzed separately from those using hydrogels as dressings or barriers to facilitate the healing of abrasions, burns, or ulcers ("Regen Wound"). Of the 223 non-lens hydrogel clinical trials, 8 involved hydrogel coils

for cardiovascular applications, 99 employed hydrogel patches, and 116 utilized bulk hydrogels. Among the bulk hydrogel trials, 31 involved injectable hydrogels. Notably, 28 injectable hydrogel have received clinical approval, and 3 were undergoing clinical trials (Mandal *et al.*, 2020).

Figure 1 — Graphs of clinical trials using injectable hydrogels worldwide

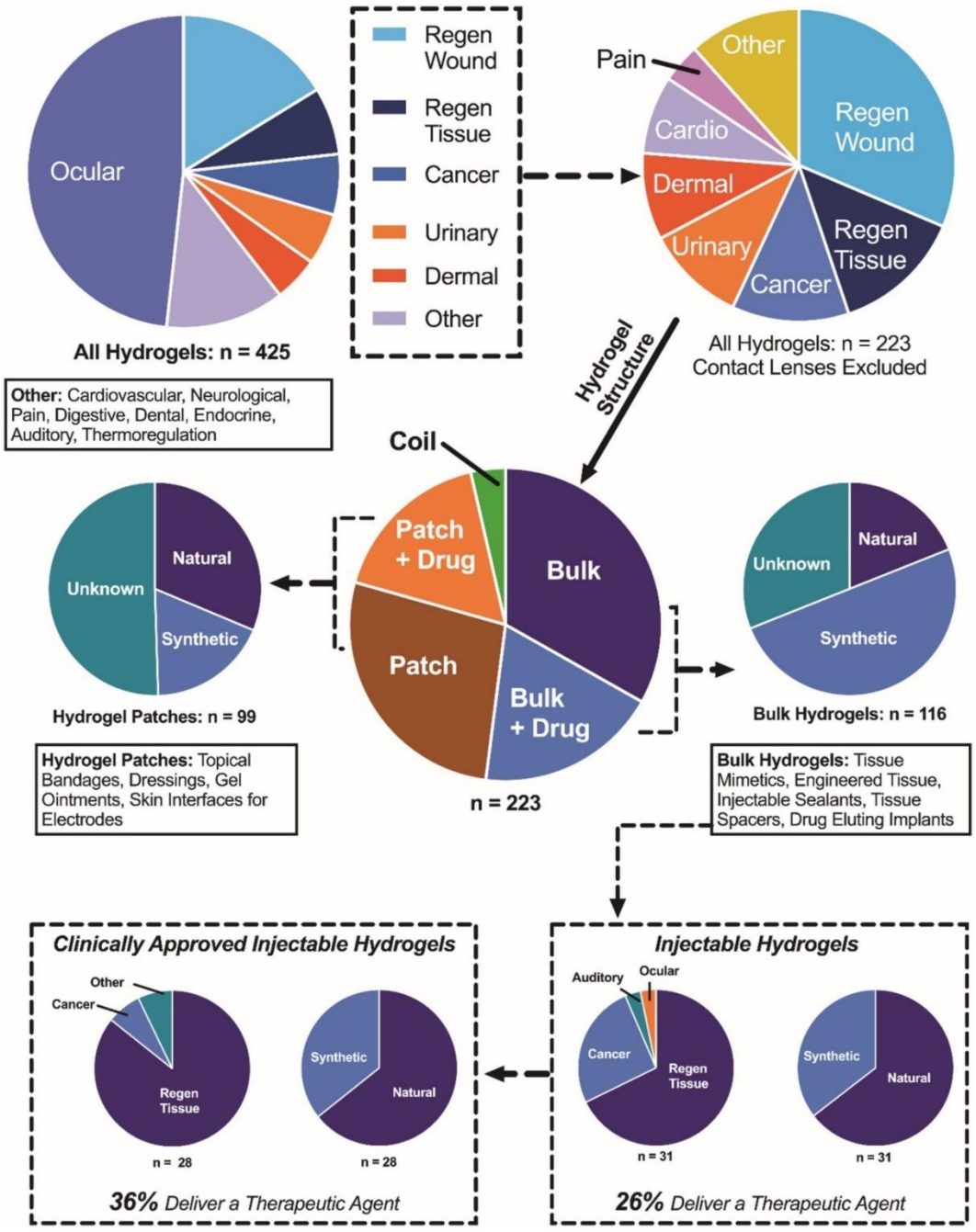

Source: Mandal *et al.*, 2020

Natural polymer-derived hydrogels are among the most used due to their high biocompatibility and easy/fast gelation mechanisms. Polymers such as collagen, gelatin, hyaluronic acid, alginate, and chitosan have been extensively studied in the biomedical field. For example, Liu *et al.*, 2023 developed an injectable hydrogel based on alginate/fibrin to locally deliver cardiomyocytes and Vascular Endothelial Growth Factor (VEGF) to the infarcted heart tissue. This system effectively promoted angiogenesis and improved cardiac function after myocardial infarction.

However, despite such advantages, injectable hydrogels based on natural polymers also face significant challenges, given their reliance on polymers characteristics, such as mechanical properties, stability, degradability and compatibility.

Overall, the application of hydrogels in healthcare remains a highly active area of research, with an increasing number of technologies advancing to clinical evaluation. The future of injectable hydrogels holds significant potential for further innovation and expansion across a wide range of therapeutic applications.

In this work, we investigated the potential of a hydrogel based on chitosan and guar gum for biomedical applications, both subjected to chemical modifications. *N*-succinyl chitosan (NSC), a water-soluble chitosan derivative, was crosslinked with aldehyde groups introduced in oxidized guar gum (OxGM). During the experimental phase, different hydrogel formulations were evaluated based on their intended applications, specifically drug delivery and tissue engineering (Figure 2). Throughout the doctoral research, the formulation was optimized and thoroughly characterized. The first phase (Chapter 1) focused on the evaluation of the polymeric ratio between the two modified natural polymers, which significantly influenced the crosslinking degree and the resulting hydrogel properties. With the optimized NSC/OxGM formulation, we further explored its biomedical applications. In the context of drug delivery (Chapter 2), lidocaine, a local anesthetic, was incorporated to develop a promising system for postoperative pain management. For tissue engineering (Chapter 3), bacterial cellulose nanofibers were added to the hydrogel to enhance its mechanical properties, which are crucial for this application.

Figure 2 – Schematic representation of the phases of this work

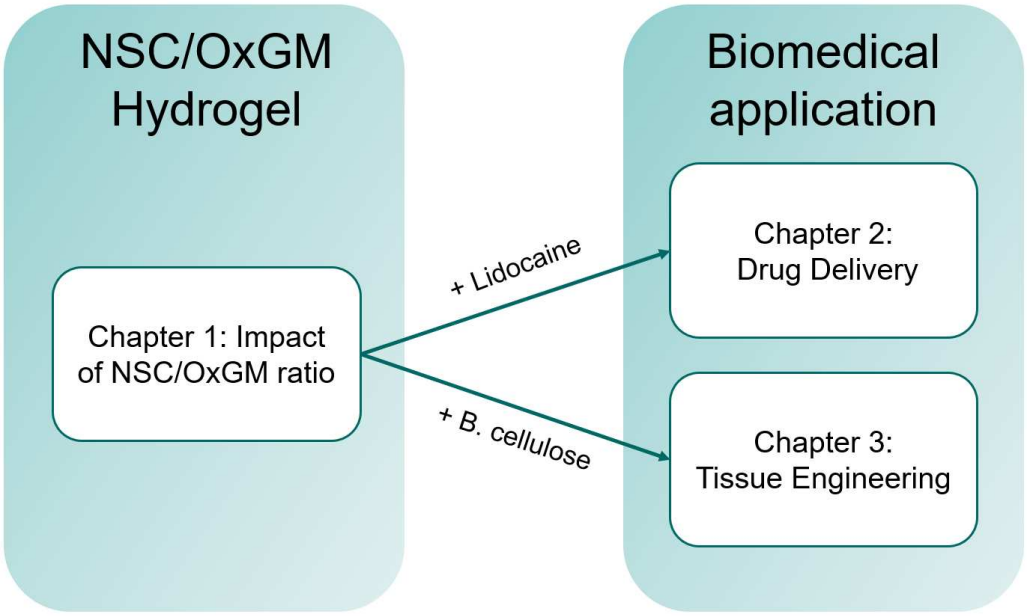

Source: Own elaboration

2 GENERAL OBJECTIVES

The main objective of this study is to investigate the biomedical potential of a natural-based injectable hydrogel formulated from *N*-succinyl chitosan (NSC) and oxidized guar gum (OxGM). This research aims to evaluate the hydrogel's physicochemical properties, biodegradability, biocompatibility, and mechanical performance. By exploring the interaction between the hydrogel components and biological systems, the study seeks to provide valuable insights into the effectiveness of this novel material for various biomedical applications, including drug delivery and tissue engineering.

2.1 Specific objectives

This study was divided into three chapters, each one with different objective as part of the process to optimize the hydrogel formulation. The specific objectives of this work are:

Chapter 1: IMPACT OF THE CROSSLINKING DEGREE ON CHITOSAN / GUAR GUM-BASED INJECTABLE HYDROGELS

Evaluate how the crosslinking degree affects the properties of NSC/OxGM hydrogels and identify the optimal formulation with enhanced biodegradability and biocompatibility for potential applications in tissue engineering and drug delivery;

- Characterize the physical, chemical, and morphological properties of NSC/OxGM hydrogels with different crosslinking degrees using FTIR, XPS, TGA, SEM, and swelling capacity;
- Determine the rheological behavior, gelation time and degradation rate of NSC/OxGM hydrogels with different crosslinking degrees in physiological conditions;
- Evaluate the cytotoxicity and cell adhesion on NSC/OxGM hydrogels with varying crosslinking degrees.

Chapter 2: LIDOCAINE RELEASE FROM INJECTABLE HYDROGEL BASED ON CHITOSAN / GUAR GUM FOR POSTOPERATIVE PAIN MANAGEMENT

Assess the potential of NSC/OxGM hydrogels as a delivery system for lidocaine in postoperative pain management;

- Characterize the chemical, physical, and morphological properties of NSC/OxGM hydrogels containing lidocaine using FTIR, TGA, and SEM;
- Study the cytotoxicity of the system NSC/OxGG + lidocaine;
- Evaluate and mathematically model the release kinetics of lidocaine from NSC/OxGM hydrogels.

Chapter 3: INJECTABLE HYDROGEL BASED ON CHITOSAN / GUAR GUM REINFORCED WITH BACTERIAL CELLULOSE NANOFIBER FOR TISSUE ENGINEERING

Evaluate the potential of NSC/OxGG hydrogels mechanically reinforced with bacterial cellulose nanofibers for tissue engineering applications;

- Characterize the chemical properties of the hydrogel composition using FTIR, XPS, and TGA;
- Assess morphological changes in the hydrogels through SEM images;
- Analyze the rheological behavior and mechanical properties of the hydrogels;
- Evaluate the biocompatibility of the studied hydrogels.

3 LITERATURE REVIEW

3.1 Biomaterials and biomedical devices

Biomaterials are synthetic or natural materials that are used as implants, devices or equipment that are in contact with biological system. It significantly affects human health, the economy and many scientific fields. Biomaterials and medical devices are widely used as prostheses in cardiovascular, orthopedic, dental, ophthalmological and reconstructive surgery, and in other applications such as surgical sutures, bioadhesive and controlled drug release. Due to devices fabricated from biomaterials, millions of lives have been saved and the quality of life improved for millions more (Wagner *et al.*, 2020).

Biomaterials can be classified based on their chemical composition into metals, ceramics, polymers, and composites. Metals, such as titanium, stainless steel, silver, gold, and cobalt-chromium alloys, are primarily used in load-bearing applications, including dental implants, joint replacements for hips and knees, and bone plates and pins. Some metallic alloys have active roles in stents, heart valves for cardiovascular applications, and orthodontic arches for maxillofacial treatments. Ceramics, including calcium phosphates, porcelain, bioactive glasses, alumina, and carbons, are highly biocompatible and inert, with exceptional hardness and compression resistance, making them ideal for surface coatings on dental and orthopedic implants to reduce wear. Composites, like hydroxyapatite-collagen and polyvinyl chloride-glass fillers, combine different materials (such as metals, ceramics, or polymers) to synergistically enhance mechanical properties compared to homogeneous biomaterials (Pires *et al.*, 2023).

3.2 Biocompatibility and biodegradability of biomaterials

The essential characteristic to validate a material as a biomaterial is biocompatibility, which is the ability of materials to properly interact with a host and not cause undesirable biological responses that could culminate, for example, in the rejection of the material by the human body. Biocompatible materials should not irritate

the surrounding tissue, provoke inflammatory responses, incite allergic or immunological reactions, or be carcinogenic (Pires *et al.*, 2023). The tissue response to an implant depends on a several factors ranging from the chemical, physical and biological properties of the materials to the shape and structure of the implant. In the case of biodegradable biomaterials, their active biocompatibility must be demonstrated over time. The chemical, physical, mechanical and biological properties of a biodegradable material will vary with time and produced degradation products can have different levels of tissue compatibility compared to the initial material.

Given the complexity and diverse applications of polymeric biomaterials, no single polymeric system can be deemed an ideal biomaterial. This highlights the necessity for developing a broad spectrum of biodegradable materials tailored to meet the specific and unique requirements of individual medical applications, ensuring optimal performance in implant fabrication.

Both synthetic and natural polymers have been extensively investigated as biodegradable biomaterials. Biodegradation of polymeric biomaterials involves cleavage of hydrolytically or enzymatically sensitive bonds in the polymer leading to polymer erosion. Depending on the mode of degradation, polymeric biomaterials can be further classified into hydrolytically degradable polymers and enzymatically degradable polymers. Most of the naturally occurring polymers undergo enzymatic degradation. The rate of *in vivo* degradation of enzymatically degradable polymers however, varies significantly with the site of implantation depending on the availability and concentration of the enzymes. Chemical modification of these polymers also can significantly affect their rate of degradation (Alizadeh-Osgouei; Li; Wen, 2019).

3.3 Injectable hydrogels

During the last decade, hydrogels have been widely explored as biomaterial in the area of tissue engineering and drug delivery due to their unique properties, including three-dimensional network, high water content, high similarity to the extracellular matrix (ECM) and flexibility. The 3D matrix is composed of cross-linked hydrophilic polymers capable of retaining water in their network structure. Polymers act as a framework to support the structure of hydrogels.

Despite these unique properties, applications of traditional hydrogels are limited since these preformed hydrogels have to be implanted subcutaneously which causes a lot of inconvenience to patients. To solve this problem, in situ-forming and injectable hydrogels that undergo a sol-to-gel transition before and after injection into the body have been developed (Li; Yang; Lee, 2021). Injectable hydrogels made of low-viscosity polymers can be applied through syringes at the desired location (*in situ*) of the patient and mold themselves into the shape of the cavity when solidified, providing a safer and non-invasive procedure (Hu *et al.*, 2017).

Once *in situ*, the hydrogel solidification may occur through physical crosslinking, associated with electrostatic force, hydrophobic interaction and hydrogen bond, or chemical crosslinking, where there is covalent bond formation through chemical reaction between functional groups of the polymeric chain, such as Schiff base (Hu; Wang; Xiao, 2019). Physical hydrogels often present low mechanical strength due to the several flaws and heterogeneity of polymeric structure and also have poor reproducibility of properties such as pore size, dissolution rate, and functionalization via chemical reaction (Padmanabhan; Nair, 2015).

Schiff base reaction (Figure 3) have been widely used to synthetize new materials for injectable hydrogels and porous scaffold for biomedical applications (Maciel *et al.*, 2019). Imine bond is obtained through reaction between carbonylic group (aldehyde and ketone) and primary amine group (Xin; Yuan, 2012). This reaction is particularly interesting for biomedical hydrogel because it can quickly occur in mild condition (physiological temperature and pH) and water is the only subproduct, which can substitute potential toxic crosslinking agent, such as glutaraldehyde and carbodiimide, that may decrease the biocompatibility of the material (Khunmanee; Jeong; Park, 2017).

Injectable hydrogels crosslinked via Schiff base reaction have high biodegradability rate due to its poorly stability upon hydrolysis (Xin; Yuan, 2012). Biodegradability is one of the most important properties for implantable hydrogel, since these biomaterials should preferably be absorbed by the surrounding tissues without the necessity of surgical removal. In addition, they should be gradually degraded into nontoxic product within a certain period of time followed by complete excretion from the body (Dwivedi *et al.*, 2017).

Figure 3 – Schiff base reaction formation mechanism

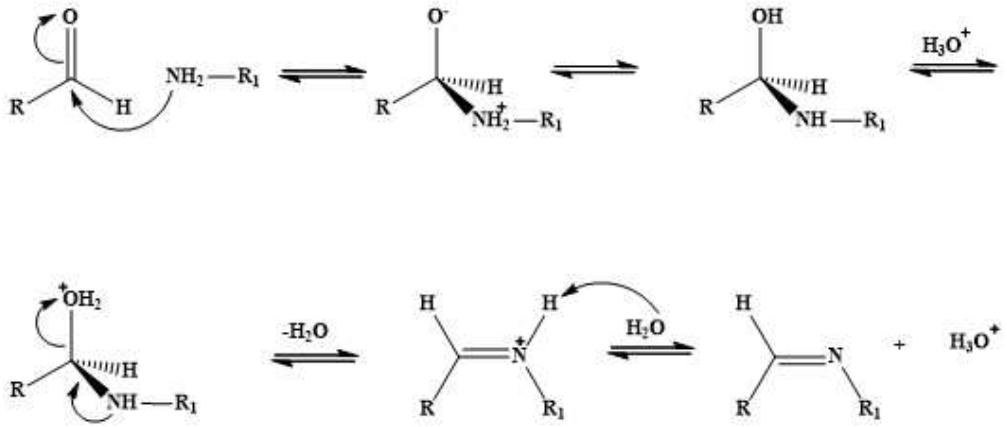

Source: Own elaboration

There are many published researches on hydrogels crosslinked by Schiff base reaction for biomedical application, mainly natural polymers, such as hyaluronic acid (Li, S. *et al.*, 2020), gelatin/alginate (Emami *et al.*, 2021), and chitosan, one of the most used polysaccharide, from drug delivery (Dalei *et al.*, 2023) to tissue engineering (Nezhad-Mokhtari; Akrami-Hasan-Kohal; Ghorbani, 2020).

3.4 Polymeric biomaterials

Polymers are the most explored material in the biomedical and pharmaceutical fields. The main factor is the enhanced biocompatibility and biodegradability feature. In addition, polymers have advantages compared to metals, alloys and ceramics, given their great manufacturability and versatility, and can be used in the most diverse forms such as films, sheets, membranes, hydrogels, fibers/nanofibers, sponges, microparticles, nanoparticles (NPs), among others (SONG *et al.*, 2018).

A polymer is a macromolecule constituted of repeating structural units (monometer), which are typically linked by covalent chemical bonds. Synthetic polymers are mainly derived from the petrochemical industry, being produced from non-renewable resources. There are several problems associated with petroleum-derived polymers, as growing economic and environmental concerns related to waste

disposal, the awareness of its finitude, soaring petroleum costs, and most of them are non-biodegradable in nature, causing accumulation and pollution (Patel; Chakraborty, 2016).

Natural polymers can be classified into polysaccharides, proteins, and microbial polymers based on their chemical structure and source. Polysaccharides are formed through glycosidic linkages between monosaccharides, with examples including chitin/chitosan, hyaluronic acid, alginate, and starch. Proteins are large biomolecules composed of one or more amino acid chains, with collagen, gelatin, and silk fibroin as notable examples. Certain microorganisms naturally produce polymers, such as polysaccharides and polyesters. Through genetic engineering, the biotechnology industry can modify microorganisms to produce polymers of significant interest for various applications (PIRES *et al.*, 2023).

3.4.1 Chitosan and N-succinyl chitosan

Several natural polymers have been investigated for use as hydrogel and chitosan, a cationic polysaccharide obtained from chitin, is one of the most explored macromolecules in biomedical field, including as wound dressing (Xue *et al.*, 2019), in the treatment against tumor cells (Choi *et al.*, 2019), matrix for tissue engineering and drug release, such as anesthetics (Foley *et al.*, 2013). Table 1 summarizes several examples of chitosan-based hydrogels utilized in biomedical applications, highlighting the various chitosan modifications and crosslinkers that have been explored.

Chitosan consists of a linear polymeric chain obtained through the deacetylation of chitin in an alkaline medium, the second most abundant polysaccharide in nature, after cellulose, and is mainly present in the exoskeleton of marine invertebrates. Chitosan structure is composed of D-glucosamine and N-acetyl-D-glucosamine units linked by β-(1′4)-glycosidic bonds, the ratio between the two units determines the degree of deacetylation. Chitosan macromolecules have unique favorable biological properties, such as antimicrobial and antioxidant action, which, combined with biocompatibility, non-toxicity and low cost, have led to extensive exploration in the biomedical area (Muxika *et al.*, 2017; Shariatinia, 2019).

Table 1 — Summary of chitosan-based hydrogels as biomaterial in the literature

Chitosan	**Crosslinking agent**	**Application**	**Comments**	**Ref**
Double-quaternized chitosan	Polyurethane	Wound dressing	To improve the rheological behavior, swelling attributes, and printability, cellulose nanofibrils were introduced into the matrix for 3D printing	Laurén *et al*, 2024
Quaternized chitosan	Oxidized hyaluronic acid	Biomedicine	Good antibacterial activity against *E. coli* and *S. aureus.* Self-healing ability	Yang *et al*, 2024
Methacrylated Zwitterionic chitosan	Thiol-functionalized graphene	Smart conductive sensors	Good cytocompatibility	Salimiyan *et al*, 2023
Carboxymethyl chitosan	Oxidized hyaluronic acid	3D printing	Favorable mechanical strength	Yu *et al*, 2023
N-succinyl chitosan	Oxidized guar gum	Wound dressing	Antibacterial and *in vivo* healing property	Oliveira *et al*, 2023
N-succinyl chitosan	Oxidized pectin	Biomedicine	Good hemocompatibility	Bazghaleh *et al*, 2022
Carboxyethyl chitosan	Dialdehyde cashew gum	Tissue engineering	Good biodegradability and biocompatibility	Ferreira *et al*, 2021

Nevertheless, the fact that chitosan is only soluble in acidic media is a significant disadvantage for use as biomedical applications. The amino groups of chitosan macromolecule have pKa values around 6.5, so for pH above this value this group does not undergo protonation, which makes solubility difficult (Bashir *et al.*, 2016).

Chemical modification of this polysaccharide is an interesting strategy for improving the physicochemical and biological properties of the biomaterial. Thus, the insolubility of chitosan in neutral media could be circumvented by adding carboxyl groups to the polymeric chain to increase its interaction with water, turning it hydrophilic (Hattori *et al.*, 2017).

N-succinyl chitosan (NSC) is one of the hydrophilic derivatives of chitosan that can be obtained through the inclusion of succinyl groups in the D-glucosamine units of the macromolecule (reaction with succinic anhydride) (Figure 4), which is soluble in a physiological environment (pH 7.4) due to the formation of carboxylate ions ($-COO^-$). Its degree of substitution (DS) can be controlled by environmental conditions and NSC with degree of substitution range of 0.45-0.8 exhibit water solubility in the pH range of 4.0-7.0 (Bashir *et al.*, 2015).

Figure 4 — Chitosan succinylation reaction with succinic anhydride

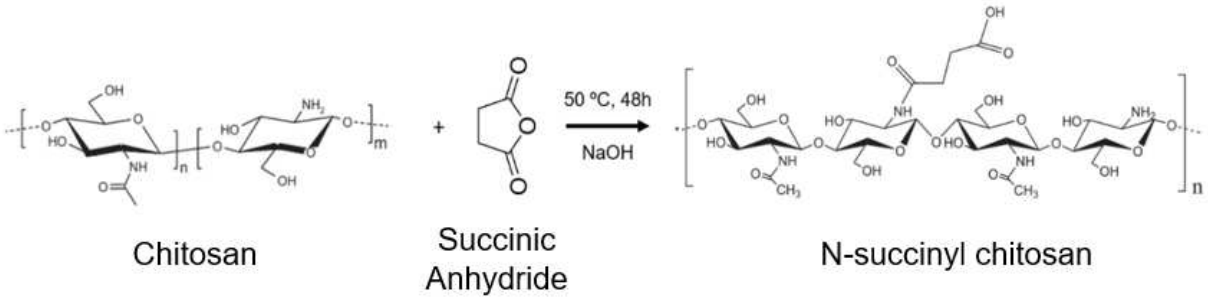

Source: Own elaboration

Hydrogels composed of NSC are well-known in the literature and are commonly cross-linked with other polymers, such as hyaluronic acid, alginate and oxidized starch (Physico-chemical characterization of pH-sensitive N-Succinyl chitosan-g-poly (acrylamide-co-acrylic acid) hydrogels and in vitro drug release studiesBashir *et al.*, 2017).

It has been reported that biodegradability of chitosan is granted by enzymes such as lysozyme, a glycosidic hydrolase present in the human body, which hydrolyzes the β (1–4) linkages between *N*-acetylglucosamine and glucosamine (Padmanabhan; Nair, 2015). The biodegradation of chitosan by lysozyme leads to the formation of D-

glucosamine and glycosaminoglycan of variable length which have low cytotoxicity toward mammalian cells (Kean; Thanou, 2010).

3.4.2 Guar Gum and Oxidized guar gum

Galactomannan (GM) is a neutral polysaccharide mainly extracted from seeds of L*eguminosae* family. It consists of a main D-mannopyranose (M) chain bonded via β-(1→4) glycosidic bonds and D-galactopyranose (G) residues linked to the main chain by α-(1→6) glycosidic bonds (Figure 5).

It serves as an energy and water reservoir for the seeds. It has been used in several functions, including rheological modifier, thickening and emulsifying agent in several segments (food and pharmaceutical industry, civil construction, among others). Besides, more recently, it is gaining interest as a biomaterial, mainly as a support for cell growth in tissue engineering and crosslinking agent for injectable hydrogels for drug release. The main sources of GM for technological purposes are guar gum, locust bean gum and tara gum, which are abundant in tropical countries, including Brazil.

Many derivatives of GM are reported in the literature, such as carboxymethyl (DALEI 2022), hydroxypropyl (Yin *et al.*, 2018), sulfated (Kazachenko *et al.*, 2021) and oxidized galactomannan (Yu *et al.*, 2022). GM oxidation is an interesting process to obtain a cross-linking agent (OxGM) because of the presence of aldehyde groups, which reacts with NH_2 groups of NSC, for example, forming covalent bonds (Schiff bonds) (Galante *et al.*, 2018).

Figure 5 ─ Chemical structure of guar gum (galactomannan)

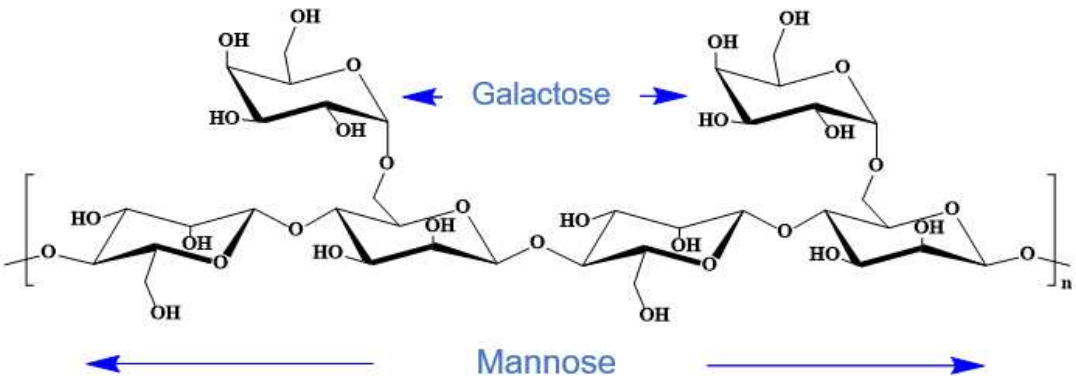

Source: Own elaboration

Oxidation reaction using sodium periodate (Figure 6) is widely used in many polysaccharides for its functionalization. It is a simple method to add aldehyde groups in the chain of macromolecules by selective oxidation of vicinal diols (Reakasame; Boccaccini, 2018). GM is a potential candidate for oxidation using sodium periodate, since its main and side chains have vicinal hydroxyls. The introduction of aldehyde groups in the GM allows this polysaccharide to act as a macro cross-linking agent for other biopolymers rich in amino groups, such as chitosan, via the Schiff base reaction.

Figure 6 ─ Oxidation reaction guar gum using sodium periodate

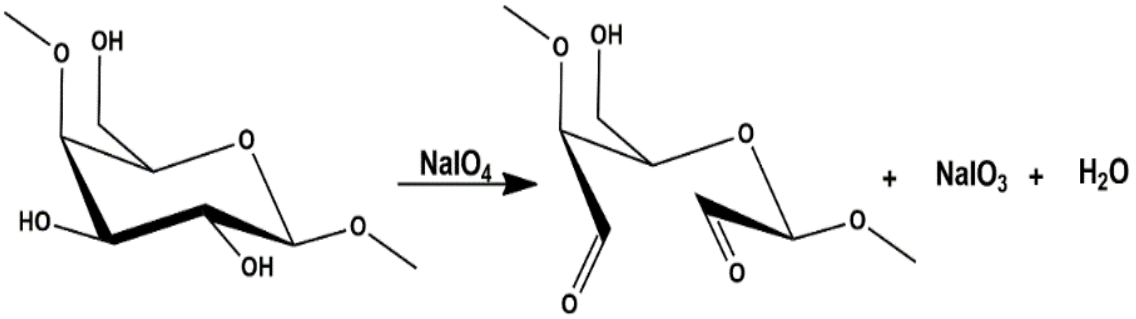

Source: Own elaboration

3.4.3 Bacterial cellulose nanofibers

Cellulose is the most abundant polysaccharide on Earth and has numerous applications in modern industry. Traditionally, cellulose has been sourced from plants, but its refinement typically involves aggressive processes to remove non-cellulose materials such as lignin and hemicellulose. Bacterial cellulose (BC), however, emerges as an alternative source of cellulose that requires no chemical or mechanical refining. With its high water-holding capacity, high crystallinity, high tensile strength, and three-dimensional network structure, BC nanofibers (BCF) are a promising biomaterial for nanocomposites and a candidate for use as reinforcement in tissue engineering applications (Vasconcelos *et al.*, 2020).

Cellulose is a natural polymer composed of β-D-glucose units linked by the elimination of water through the combination of H and OH- groups (Figure 7). The equatorial positions of the hydroxyls on the cellulose chain allow them to form lateral

hydrogen bonds, resulting in a highly ordered structure ideal for fiber-forming polymers. The interchain hydrogen bonds create crystalline regions, providing a strong and stable structure, which gives the resultant fiber good strength and insolubility in most solvents. In the non-crystalline region, the chains are more spread and available for hydrogen boding with other molecules, such as water. An interesting property of cellulose is its ability to absorb water (swell) without dissolving (Abdul Khalil *et al.*, 2015).

Figure 7 — Chemical structure of cellulose chain

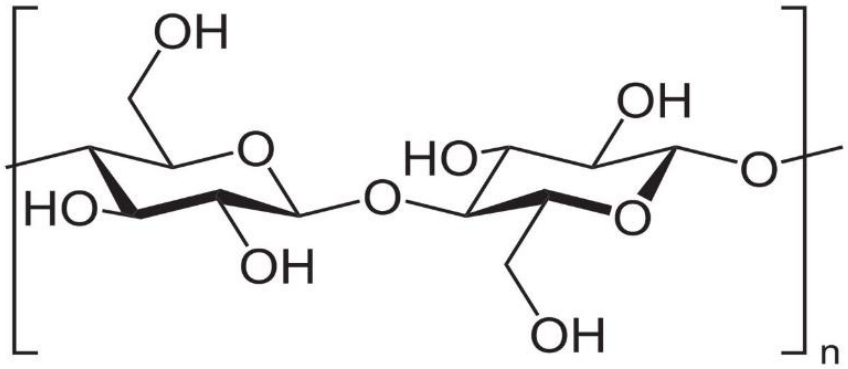

Source: Own elaboration

Due to its unique properties and excellent biocompatibility, BCF has attracted considerable interest in the biomedical field. BCF can be easily molded while retaining its intrinsic properties, a crucial characteristic for biomaterials. Its biomedical applications include wound dressings (Wahid *et al.*, 2021), drug delivery systems (Ullah *et al.*, 2019), and even filament for surgical sutures (Wu *et al.*, 2018).

Bacterial cellulose (BC) exhibits structural characteristics of nanofibers that closely resemble the collagenous fibers found in bone tissue. Specifically, BC has a density of 1600 kg/m³, a Young's modulus of 138 GPa, and a tensile strength of 2 GPa (Chen *et al.*, 2022). These properties promote favorable cellular responses when interacting with surrounding tissue and do not trigger inflammatory reactions upon implantation. Bella and co-workers (Bella; Widiyanti; Aminatun, 2020) investigated the preparation and properties of BC-chitosan-glycerol composites. Their findings from morphology, tensile strength, swelling, degradation, and cytotoxicity tests revealed that the BC-chitosan-glycerol composite possesses characteristics suitable for use as an artificial dura mater.

3.5 Drug delivery system

Drug delivery systems are able to release bioactive molecules to achieve a desired therapeutic response in patients. Traditional systems, such as tablets, capsules, and ointments, have suffered from poor bioavailability and fluctuations in plasma drug level and are not able to achieved controlled release. It is necessary to maintain the plasma drug concentration above the minimum effective concentration (MEC) and below the toxic concentration to achieve maximum efficacy and safety (Adepu *et al.*, 2021).

As shown in

Figure 8, multiple doses in regular times results in fluctuation in plasma drug levels and often reaches below effective level and above toxic levels. Another approach is a single dose greater than the required dose, which leads to adverse effects. Hence, a controled drug delivery system are required to maintain the plasma drug concentration at a constant rate whithin the safety window and offer the desired therapeutic effect for a longer duration of time.

Drug release from hydrogel are an atractive strategy because the porous three-dimensional structure allows the incorporation of drugs while creating a diffusion barrier. The release of drugs from hydrogels are related to three phenomenon: i) degradation: polymer chain breakage *via* hydrolytic or enzymatic degradation, releasing incorporated drugs, ii) swelling: when the molecule diffusion is faster than the hydrogel swelling, the latter conditioning the release, iii) diffusion: when hydrogel swelling faster than diffusion phenomeon. Drug diffusion is governed by the pore size in the hydrogel matrix. The higher swelling rate, the bigger the pores, and the faster the small size drug diffusion through the hydrogel (Peers; Montembault; Ladavière, 2020).

Kinetic models can be useful to study *in vitro* drug release from hydrogels and to predict *in vivo* bioavailability behavior. There are several kinetic models reported in the literature, but few take into account the physical and chemical characteritics of the system.

Figure 8 ─ Graphs showing plasma concentration of different drug treatment apllications over time

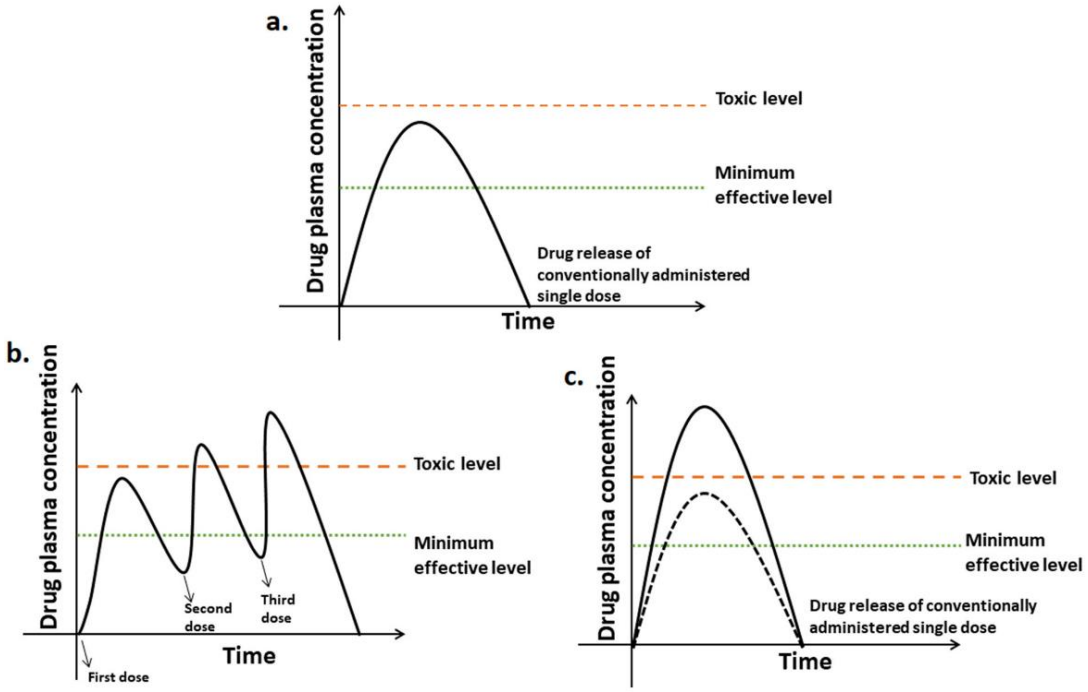

Source: ADEPU *et al.*, 2021

The Korsmeyer-Peppas equation (1986) (1), or power law, is a non-linear, semi-empirical model that consider diffusion caused by concentration gradient (Fickian), and also different release mechanims, such as degradability and swelling (non-Fickian diffusion), and geometric characteristics of the drug delivery system. It is the most used fitting model for drug delivery from hydrogels-based systems.

$$\frac{M_t}{M_\infty} = k_P \times t^n \qquad (1)$$

where M_t/M_∞ is the drug release fraction at time t, k_P is the kinetic constant and n is the transport exponent related to the release mechanism (Table 2). To the determination of the exponent n the portion of the release curve where $M_t/M_\infty < 0.6$ should only be used (Wu *et al.*, 2019).

Table 2 ─ Different transport exponent ‘n’ related to geometric characteristics and release mechanism

Transport exponent (n)			Release mechanism
Planar	Cylindrical	Spherical	
n < 0,5	n < 0,45	n < 0,43	Semi- Fickian
n = 0,5	n = 0,45	n = 0,43	Fickian
0,5 < n < 1	0,45 < n < 0,89	0,43 < n < 0,85	Non-fickian
n = 1	n = 0,89	n = 0,85	Zero-order
n > 1	n > 0,89	n > 0,85	Case 2 – Super Transport

Source: WU *et al.*, 2019

3.6 Biomaterials in Tissue engineering

Tissue engineering is a field focused on developing functional tissues through the integration of cells, scaffolds, biomaterials, and biologically active components. The primary goal is to create constructs that can restore or enhance the function of damaged tissues. The concept of tissue engineering was first introduced in the late 1980s during a meeting organized by the National Science Foundation in the USA. The term "tissue engineering" gained recognition in 1991 with the publication of the paper "Functional Organ Replacement: The New Technology of Tissue Engineering." A significant milestone was reached in 2008 when the first fully tissue-engineered organ, a trachea, was successfully transplanted into a 30-year-old woman, marking a major advancement in the field (Eldeeb; Salah; Elkasabgy, 2022).

Tissue engineering can be categorized into *ex vivo* and *in situ*, depending on how the material is fabricated and applied. *Ex vivo* tissue engineering involves isolating cells, which are then seeded onto an external scaffold within a controlled environment, often in bioreactors, to promote cell proliferation and, in the case of stem cells, differentiation into the desired tissue type. Once the tissue is formed, it is implanted into the target area, where parameters like the size and shape of the defect are crucial. The scaffold may degrade over time, allowing the newly regenerated tissue to replace it (Blume *et al.*, 2022; Fu *et al.*, 2021). This approach requires scaffolds with

strong mechanical properties and permits the use of various biomaterials. However, it also involves complex optimization of bioreactor conditions, high costs, potential donor site morbidity, and the risk of rejection at the implantation site. Despite these challenges, ex vivo engineering is the primary method for developing non-regenerating tissues, such as cardiac and neural tissues (Chandika *et al.*, 2020).

In contrast, *in situ* tissue engineering offers a simpler approach by pre-fabricating a scaffold from biocompatible biomaterials, and implanting it directly into the target tissue without prior cell seeding. This method relies on the proliferation and attachment of surrounding cells, promoting the host's tissue regeneration. However, the regenerated tissue may suffer from poor mechanical properties due to the lack of control over cellular differentiation (Gaharwar; Singh; Khademhosseini, 2020; Li; Ma; Gao, 2015).

The objective of tissue engineering is to repair and regenerate damaged tissues using various approaches. Biomaterials, defined as any material or construct that interacts with biological systems, play a crucial role in this process. Regardless of their origin, biomaterials must be biocompatible to prevent immune responses, sterilizable for safe integration into host tissues, biodegradable to naturally degrade after completing their function, and bioactive to stimulate tissue regeneration. These characteristics are essential for the successful application of biomaterials in tissue engineering.

CHAPTER 1: IMPACT OF THE CROSSLINKING DEGREE ON CHITOSAN / GUAR GUM-BASED INJECTABLE HYDROGELS

ABSTRACT

Evaluating the biodegradability and biocompatibility of hydrogels is essential for identifying materials suitable for biomedical applications. This study describes the fabrication of hydrogels utilizing physiological-soluble chitosan (N-succinyl chitosan, NSC) crosslinked with dialdehyde guar gum (Oxidized Galactomannan, OxGM) via the Schiff-base reaction. Hydrogels with varying volumetric ratios of NSC/OxGM, resulting in distinct NH_2/CHO functional group ratios and crosslinking degrees, underwent comprehensive characterization using Fourier-transform infrared spectroscopy (FTIR), X-ray photoelectron spectroscopy (XPS), thermogravimetric analysis (TGA), swelling, and scanning electron microscopy (SEM). Gelation time (tgel) was assessed by rheological analysis (crossover G'=G''), where tgel increased with higher crosslinking density, reaching a maximum value of ~80 s. Biodegradation analysis in phosphate-buffered saline (PBS) with lysozyme (13 mg/L) revealed that the crosslinking degree significantly influenced degradation, with lower crosslinking associated with an elevated degradation profile. Moreover, cell viability assays with fibroblastic cells demonstrated minimal cytotoxicity, but an increase in free aldehyde groups correlated with decreased cell viability. For the most crosslinked hydrogel, the compressive test yielded a Young's modulus value of 67.2 kPa (± 8.5). These results suggested that the all hydrogels exhibit favorable biodegradability but only the highest crosslinked one was citocompatible, making it promising candidate for diverse biomedical applications.

Keywords: Biomaterials, polymers, polysaccharides, hydrogels, chitosan

1 INTRODUCTION

Material science is advancing rapidly, particularly with regard to the discovery of innovative products for biomedical applications. Natural polymers are highly attractive materials for use in medical devices and pharmaceutical applications due to their superior biological properties, including good biocompatibility and biodegradability (Bil *et al.*, 2020; Xing *et al.*, 2019). In addition, natural polymers obtained from renewable and non-fossil origins represent sustainable alternatives to traditional synthetic polymers produced from oil-derived monomers (Galante *et al.*, 2018).

Biocompatibility and biodegradability are two of the most important requirements for implantable materials used in biomedical applications. Ideally, these materials should not produce a toxic or immunological response in the human body (Ressler, 2022), and the surrounding tissues should absorb them without the need for surgical procedures. As such, the material should be gradually degraded into nontoxic products within a specific period, followed by complete excretion from the body. For tissue engineering, the biodegradation rate must be as similar as possible to tissue formation. While cells produce their own natural matrix structure, the scaffold should provide structural integrity for the cells and eventually disappear, leaving the newly formed tissue (Dwivedi *et al.*, 2017). Drug-loaded implants made with biodegradable polymer matrixes allow molecules to be gradually released from the matrix for a sustained drug delivery, which can occur by diffusion and erosion. The polymeric matrix acts as a diffusion barrier to slow drug release, and release rates can increase as that barrier degrades (Bil *et al.*, 2020; Gu; Burgess, 2014). Therefore, knowledge of biodegradation kinetics is crucial when designing new biomaterials for their safe use in medical devices.

Hydrogels, with their unique properties, such as three-dimensional networks, high water content, ability to retain and diffuse molecules, and similarity to the extracellular matrix (ECM), have gained significant attention in tissue engineering and drug delivery (Hu *et al.*, 2017). The application of hydrogels for improving healthcare is a highly active research area, with a growing number of technologies being evaluated in humans (Mandal *et al.*, 2020).

Schiff base reactions have been widely utilized for injectable hydrogels as

a crosslinking method for novel materials in biomedical applications (Maciel *et al.*, 2019; X. Junpeng, L. Yi, 2019). An imine bond is obtained through the reaction between the carbonylic group (aldehyde and ketone) and the primary amine group (Xin; Yuan, 2012). Hydrogels crosslinked via Schiff base reactions have excellent biodegradability rates, compared to irreversibly crosslinked ones, due to their poor stability upon hydrolysis (Xin; Yuan, 2012).

The synthesis of *N*-succinyl chitosan (NSC) addresses the solubility limitation of chitosan in acidic media, resulting in a hydrophilic derivative that is soluble in the physiological environment (pH 7.4) (Physico-chemical characterization of pH-sensitive N-Succinyl chitosan-g-poly (acrylamide-co-acrylic acid) hydrogels and in vitro drug release studiesBashir *et al.*, 2017). This derivative is obtained using a simple preparation procedure, is free from toxic reagents, and has a low production cost (Bashir *et al.*, 2015). Oxidation reactions are used for the functionalization of polysaccharides. Due to the high reactivity of the introduced aldehyde groups, oxidized polysaccharides can react with amino-group-containing materials, such as chitosan, to form Schiff bases (Matsumura; Rajan, 2021).

In our current study, we explored the influence of the biopolymer and its respective volume ratio on NSC and OxGM based hydrogels. Our goal was to develop an optimal formulation for potential applications as biomaterials, including wound dressing, drug delivery systems, and bioink for 3D printing platforms in tissue engineering. Initially, chitosan underwent chemical modification to enhance its water solubility by introducing N-succinyl groups to the glucosamine units. Simultaneously, galactomannan was oxidized using sodium periodate ($NaIO_4$) to introduce reactive aldehyde groups along the polymeric chain, resulting in OxGM. Subsequently, NSC and OxGM were combined in different ratios. The resulting blend hydrogels underwent comprehensive characterization by Fourier transform Infrared spectroscopy (FTIR) and X-ray photoelectron spectroscopy (XPS) analysis, scanning electron microscopy (SEM) morphology observation, swelling test, in vitro biodegradation assay and rheological behavior analysis. Furthermore, their biocompatibility was evaluated using a indirect and direct cytotoxicity assay.

2 MATERIALS AND METHODS

All experiments were conducted at the Laboratory of Polymer (LabPol – DQOI-UFC) and the Laboratory of Biomaterials and Bioproducts (LPB – DEQ - UFC). The exceptions include the Scanning Electronic Microscopy (SEM) images, which were obtained at Central Analítica – UFC, Nuclear Magnetic Resonance (NMR) analysis, conducted at Centro Nordestino de Aplicação e Uso da Ressonância Magnética Nuclear (CENAUREMN – UFC), and X-ray Photoelectron Spectroscopy (XPS) analysis, which were performed at Laboratory of Biomaterials and Bioengineering (LBB - Université Laval, Canada).

2.1 Materials

Low molecular chitosan from shrimp shells (77% degree of deacetylation, Mw = 84.2 kDa), gum guar (galactomannan) and lysozyme from lyophilized chicken egg powder (>90%) were purchased from Sigma Aldrich, Brazil. Commercially available methanol, ethanol, acetone, ethylene glycol and glacial acetic acid were purchased from Synth, São Paulo, Brazil. Succinic anhydride (Sigma Aldrich, Brazil), sodium hydroxide (Vetec, Brazil), sodium periodate (Vetec, Brazil), and hydroxylamine hydrochloride (Vetec, Brazil) were all acquired in analytic grade (>99% purity).

2.2 Synthesis of *N*-succinyl chitosan

N-succinyl chitosan was synthesized following a modified protocol described by Bashir *et al.* (Bashir *et al.*, 2016). Initially, 2.0 g of chitosan was dissolved in 200 mL of 5.0% (v/v) acetic acid solution, with continuous magnetic stirring at 60 °C for 45 minutes. Subsequently, 100 mL of methanol was added into the system, followed by the addition of 7 g of succinic anhydride dissolved in 60 mL of acetone. The reaction was maintained at 50 °C for 48 hours. After the reaction period, the pH of the solution was adjusted to 12 using a 1.0 mol/L NaOH solution to deprotonate the carboxyl

groups, thereby enhancing the water solubility of NSC. After more 24 hours and at room temperature, the resulting product was precipitated by adding 800 mL of 95% (v/v) ethanol. The solid product underwent multiple washes with ethanol and acetone using a sintered plate funnel (N° 4) to eliminate excess reagents. The labeled product was then securely stored in a desiccator at room temperature.

2.2.1 Determination of degree of substitution (DS)

The degree of substitution (DS) of *N*-succinyl chitosan was determined using ^{1}H NRM spectroscopy (Bruker Avance – DPX 300 model spectrometer) with D_2O and DCL as solvent. 3-(trimethylsilyl)-1-propanesulfonic acid sodium salt (DSS) served as the internal standard. DS was calculated according to Equation 2 (Oliveira *et al.*, 2023).

$$DS\ (\%)=\left[(1-DD\times10^{-2})\times\frac{3}{4}\times\frac{(A\ \delta\ 2.67\ ppm)}{(A\ \delta\ 2.05\ ppm)}\right]\times100 \qquad (2)$$

where the resonances at δ 2.05 ppm corresponds to acetyl group protons (H_3CCONH-R) and δ 2.67 ppm to methylene protons (R-CO-CH_2-CH_2-COOH). The 3/4 ratio is associated with the 3 hydrogen atoms of the acetyl group and the 4 hydrogen atoms of the methylene groups.

2.3 Oxidation of galactomannan

Galactomannan was oxidized following the method described by YAN *et al.*, 2014. This involved the conversion of OH groups to CHO in the monosaccharide units of galactomannan (GM) through the use sodium periodate as the oxidizing agent. GM (1 g or 0.0062 mol of monosaccharide units) was dissolved in 200 mL distilled water and stirred for 24 h. Sodium periodate (0.66 g, or 0.0031 mols) was then added to achieve a theoretical oxidation degree of 50%. The reaction system was wrapped in

aluminum foil to protect it from light and prevent the photo-induced decomposition of periodate ions. The reaction was carried out for 6 hours and was interrupted by adding ethylene glycol to $NaIO_4$ in a 1:1 molar ratio. The resulting solution underwent dialysis against distilled water for 4 days using a cellulose membrane with an exclusion limit of 1.4×10^4 g/mol. The oxidized derivative was subsequently lyophilized.

2.3.1 Degree of oxidation and molar mass for galactomannan

To determinate the oxidation degree of OxGM, the method proposed by Zhao and Heindel (Zhao; Heindel, 1991) was employed. $NH_2OH{\cdot}HCl$ (0.25 mol/L) was added to the OxGM solution, followed by potentiometric titration using NaOH (1 mol/L). The degree of oxidation was calculated according to Equation 3, resulting in an oxidation degree of 52%.

$$\text{Degree of oxidation } (\%) = \frac{(C \times V) \times 162)}{2m} \times 100 \quad (3)$$

where V (mL) is the consumed volume of NaOH solution (1 mol/L); C (mol/L) the concentration of NaOH solution; m (g) the weight of OxGM, and 162 (g /mol) is the molar mass of the main monosaccharide repeating unit of galactomannan (galactose).

The molar mass (MM) of GM and OxGM species was estimated by gel permeation chromatography (GPC) using Shimadzu LC-20AD chromatograph equipped with RID-10A refractive index detector and PolySep linear column (7.8 mm × 300 mm) as the stationary phase. A $NaNO_3$ solution (0.1 mol/L) was used as eluent at a flow rate of 1 mL/min. The calibration curve (Equation 4) was obtained under the same experimental conditions with pullulan (Shodex Denko®) with molar mass in the range of 5.90×10^3 to 7.88×10^5 g/mol.

$$\text{Log MM} = (-1{,}12 \times Ve) + 14.33 \quad (4)$$

where Ve is the volume of elution (mL).

2.4 Preparation of the NSC/OxGM hydrogels

NSC was dissolved in distilled water with stirring for 30 min at 50 °C to prepare a 2.5 (% w/v) concentration solution. OxGM solution was prepared to obtain 2.5 (% w/v) in distilled water for 24h at 60 °C. Polymer solutions were mixed in different volumetric ratios of NSC/OxGM (Table 3) and 1 mL of each hydrogel was added to a 48-well plate and left to cross-link for 24 h.

Table 3 ─ Composition of the studied hydrogels and their ratio of functional groups.

Sample	NSC (mL)	OxGM (mL)	Molar ratio of -NH_2/-CHO
75C25G	0.75	0.25	9:10
50C50G	0.50	0.50	3:10
25C75G	0.25	0.75	1:10

The molar ratio of -NH_2/-CHO was determined by the molecular weight of monosaccharide units linked in the polymer. The number of amino groups was calculated through NMR integration analysis, following the methodology previously reported by our group (Oliveira *et al.*, 2023), while aldehyde groups were assessed by potential titration (APPENDIX A).

2.5 Fourier Transform infrared spectroscopy (FTIR)

The spectra of the polymers and copolymers were obtained using potassium bromide (KBr) pellets on the Shimadzu IR-Trace 100 spectrophotometer. The spectra were recorded in the region between 4000 and 400 cm^{-1} of wavenumber.

2.6 X-Ray Photoelectron Spectroscopy

XPS analyses were carried out using the Physical Electronics PHI 5600-ci equipment (Chanhassen, MN, USA). A standard aluminum X-ray source (1486.6 eV) was used to record survey spectra with charge compensation. High resolution C1 s XPS spectra were recorded using a standard magnesium X-ray source (1253.6 eV) without charge neutralization and then curve-fitted by referencing each spectrum to carbon at 285.0 eV. Detection was carried out at an angle of 45º concerning the surface normal, and the analyzed area was 0.5 mm^2. Three measurements for each sample were taken to confirm the homogeneity of the chemical composition.

2.7 Thermogravimetric analysis (TGA)

Thermal gravimetric analysis (TGA) was obtained using the Mettler-Toledo model (TGA/SDTA) 851^e. Samples were weighed in an analytical mill (~5 mg), placed in an alumina crucible and heated from 25 to 800 °C at a heating rate of 10 $°C \cdot min^{-1}$ under an oxidized atmosphere (synthetic air). TGA curves were derived using OriginPro® 8.5 software to obtain the differential thermogravimetry (DTG) curves.

2.8 Gelation time via rheology

The AR 550 rheometer (TA Instrument) was used to evaluate the gelation time by rheology. All formulated hydrogels were prepared with polysaccharides in aqueous solution, at a concentration of 2.5 (% w/v), and with different ratios of 75:25, 50:50, 25:75 (v/v). This experiment was performed by measuring the storage modulus (G') and loss modulus (G''), where t_{gel} corresponds to the crossing between them (G' = G''), the point at which there was a sol-gel transition (crossover), at a frequency of 1 Hz and shear stress of 5 Pa. The polymeric solutions were transferred to the rheometer and measurements started at t = 30 s after mixing the solutions.

2.9 Evaluation of swelling behavior

For the equilibrium swelling degree determination test, freeze-dried samples were previously weighed, then immersed in 30 mL of PBS solution (0.01 mol/L, pH= 7.4) for predetermined intervals. After immersion, samples were taken, and excess PBS was carefully removed from the surface using filter paper and then weighed. The percentage of fluid retention was calculated according to Equation 5:

$$M\% = \left(\frac{m_0 - m}{m_0}\right) x\ 100\% \quad (5)$$

where M_S is the mass of the swollen sample and M_D is the mass of the dry sample. The experiments were performed in triplicate.

2.10 *In vitro* biodegradation study

In vitro biodegradation study of the different rate mass of NSC:OxGM hydrogels was determined by weighing the samples at different times after PBS and PBS/Lysozyme solution immersion. Samples were freeze-dried and weighed (initial mass, m_0), and then immersed in Falcon tubes containing 30 mL of PBS buffer solution and PBS containing 13 µg/L lysozyme solution (similar to the concentration present in human serum) (Kenawy *et al.*, 2019). The system was kept under constant agitation at 37 ºC. The lysozyme solution was replaced every two days to maintain its enzymatic activity. The material was removed at specific times (1, 3, 7, 14, 21, and 28 days), freeze-dried and weighed again (m). The degradation rate (M%) was calculated according to Equation 6. The experiment was performed in triplicate (n=3).

$$M\% = \left(\frac{m_0 - m}{m_0}\right) x\ 100\% \quad (6)$$

2.11 Morphology and porosity

The morphology of the freeze-dried hydrogels, before and after degradation, was examined by scanning electron microscopy using the Quanta-FEG FEI 450 equipment. Samples were firstly frozen using liquid nitrogen to preserve the porous structure and manually fractured. Prior to analysis, samples were metalized with platinum under an argon atmosphere using a Polaron SC500 Sputter Coater. The images were obtained under high vacuum by tracking the signal of secondary electrons, operating with 4 kV of voltage acceleration and 10 mm of working distance.

Porosity was measured by the ethanol displacement method (Carlos *et al.*, 2021). First, samples were immersed in 30 mL of absolute ethanol and centrifuged for 10 min at 1200 rpm to facilitate ethanol permeation throughout the samples, as they floated in absolute ethanol. After centrifugation, excess ethanol was absorbed with filter paper and the samples were weighed at regular intervals until the weight became constant. The mass difference between the wet and dry sample was considered to represent the empty pores that the ethanol was able to occupy and porosity was calculated according to Equation 7:

$$\text{Porosity (\%)} = \left(\frac{m_F - m_I}{\rho_{et} \times V}\right) \text{x } 100 \qquad (7)$$

where m_F is the final mass and m_I is the initial mass, V is the volume of the samples measured using a pachymeter and ρ_{et} is the density of the ethanol (0.789 g/cm³). The assay was performed in triplicate. The pore diameter of the hydrogels was measured from SEM images using ImageJ® software.

2.12 Indirect cell viability

The *in vitro* biocompatibility of the hydrogels was analyzed by indirect method assay. L929 cells (mouse fibroblast cells) were cultured with DMEM media in a 95% humidity / 5% CO_2 incubator at 37 °C (standard culture condition) for 24 h. Meanwhile, the extracts of 1 mL sterilized hydrogel were obtained by immersing the

samples in 1 mL of DMEM culture medium (10% FBS and 1% penicillin-streptomycin) and incubated at 37 °C for 24 h, according to the procedure recommended by the International Organization for Standardization (ASTM 10993-12) (Biological Evaluation of Medical Devices—Part 5: Tests for In Vitro Cytotoxicity, 2009). A sufficient volume of medium was used to account for the swelling of the samples. After the incubation period, the extracts obtained were centrifuged, as a precautionary measure to remove residual pieces of hydrogel.

For the viability test, 100 µL of a cell suspension (10 × 10^4 cells/mL) of mouse fibroblasts (L929) in DMEM were added to each of the 96-well plates. The plates were incubated for 24 h in standard conditions for the cells to adhere to the plate surface. After incubation, the culture medium was removed and replaced with 100 µL of the sample extracts, with a further incubation period of 24 or 48 h, under identical conditions. The extracts were collected, and the wells were washed with sterile PBS. Then, 100 µL of culture medium containing 120 µL (25 mg/ 1 mL DMEM) of resazurin were added and left for 4 h under standard culture conditions. Finally, 100 µL of medium were collected, and the fluorescence intensity of the plates was measured using a spectrophotometer (SpectraMax i3x, Molecular Device, EUA), λ excitation = 560 nm and λ emission = 590 nm. The cell viability percentages were calculated from normalized values, based on the control fluorescence, according to Equation 8. The control was composed of cells that were exposed only to the supplemented DMEM medium (n = 4 samples/condition).

$$\text{Cells viability (\%)} = \frac{F_{sample}}{F_{control}} \text{ x } 100 \quad (8)$$

2.13 Direct cell viability

Neonatal human dermal fibroblasts (nHDF) were incubated in standard culture conditions in supplemented DMEM. Cells were subcultured when at 80% confluency, according to supplier protocols. Cells were used at passage 8 for the direct experiment.

Initially, 500 µL hydrogel was prepared in each well of a 24-well plate, followed by the addition of 500 µL of supplemented DMEM containing 1 × 10^6 cells/mL onto the hydrogel surface (Figure 9). The samples were incubated at 37 °C for predetermined time intervals. At each time point, the media was removed and a resazurin sodium salt in DMEM (0.01 $mg.mL^{-1}$) was added. The samples were then incubated for 4 hours at 37 °C, protected from light. After incubation, three 100 µL aliquots from each sample were transferred into a 96-well plate, and fluorescence was measured using a spectrophotometer (SpectraMax i3x, Molecular Device, EUA) (n = 3 samples/condition for each time point).

Figure 9 ─ Schematic representation of the direct cell viability

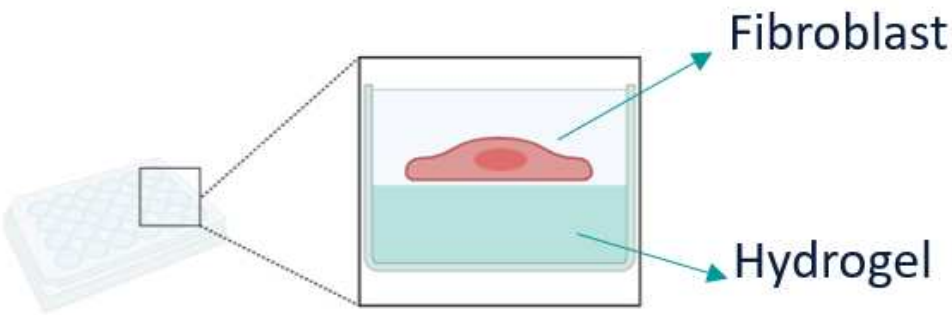

Source: Own elaboration

2.14 Analysis of the mechanical properties

For the analysis of the mechanical properties, we selected the most crosslinked hydrogel, as this represented the most optimal formulation based on the cytotoxicity test results. The 75C25G hydrogel was assessed using a TA. XT2i texture analyzer (Stable Micro Systems, UK), under a crosshead speed of 5 mm/min, set to 80% of strain at room temperature. Ten hydrogel samples, with a thickness of 30 mm and a diameter of 16 mm (Figure 10), were prepared in a mold as test specimens.

Figure 10 ─ Samples of 75C25G hydrogels prepared for the compressibility assay

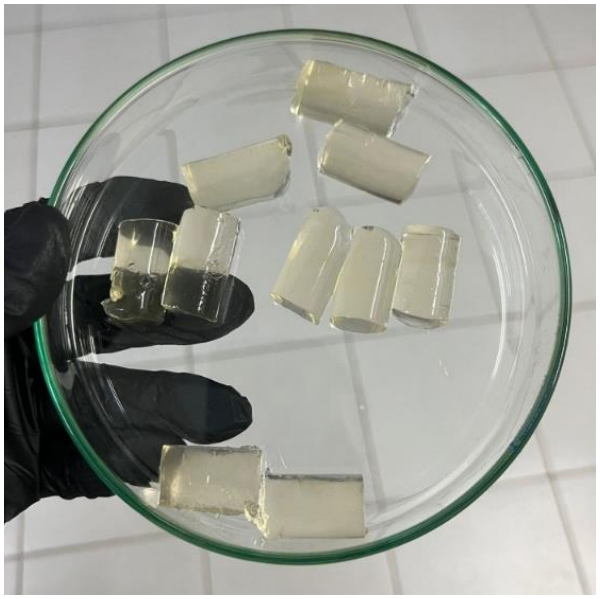

Source: Own elaboration

Both the compressive modulus (E) and compressive stress (σ_{MAX}) were calculated from the stress–strain curves. The compressive modulus was determined from the initial linear section of the stress–strain curve, specifically within the strain range of 0–20%. Compressive stress was defined as the stress point at which the material fractured.

2.15 Statistical Analysis

All experiments were performed at least in triplicate and data are presented as mean ± standard deviation (SD). Statistical analysis was performed using one-way analysis of variance (ANOVA) using Excel® and Origin® software. Differences between groups were considered significant when $p < 0.05$.

3 RESULTS AND DISCUSSION

3.1 NMR of *N*-succinyl chitosan

Nuclear magnetic resonance (NMR) was used to confirm the chemical modification of chitosan and to calculate the degree of substitution (DS) in the succinylated derivative through the relative integration of protons.

Figure 11 — ^{1}H NMR spectrum of NSC at 25°C in D_2O/DCl

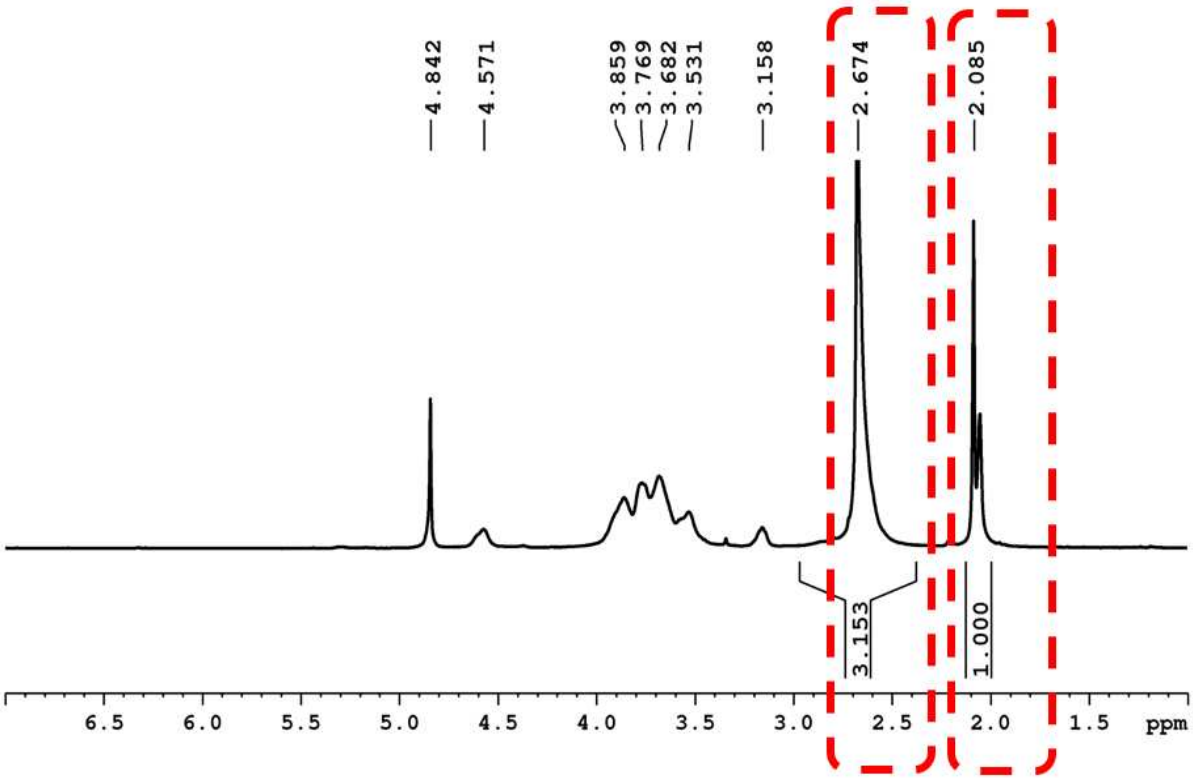

In the NSC spectrum (Figure 11), signals appeared at δ 2.06 – 2.09, 3.22 and 4.90 ppm that were attributed to the protons of the acetyl group, H_2 and H_1 of the N-acetyl-β-D-glucosamine units (the first two) and β-D -glucosamine (the latter), respectively (RINAUDO, 2006). The signal at δ 2.66 ppm was attributed to the methylene protons of the grafted succinyl group (SKORIK *et al.*, 2017). The degree of substitution was found to be 54.4%. The NSC spectrum confirms that the chitosan

structure is preserved in the derivative, with variations in intensity and displacement primarily due to chemical modification.

3.2 Degree of oxidation and molar mass of OxGM

The degree of oxidation represents the molar percentage of oxidized units in the modified polysaccharide. This is determined by reacting the oxidized derivatives (OxGM) with hydroxylamine hydrochloride ($NH_2OH \cdot HCl$), resulting in dehydration, oxime formation, and the release of HCl. The released HCl is then quantified through potentiometric titration using a standardized alkaline solution (NaOH 1 mol/L), as illustrated in Figure 12. While the theoretical degree of oxidation was calculated to be 50%, the experimental results showed a slightly higher oxidation degree of 54%.

Figure 12 – Titration graph using volume of NaOH 1 mol/L

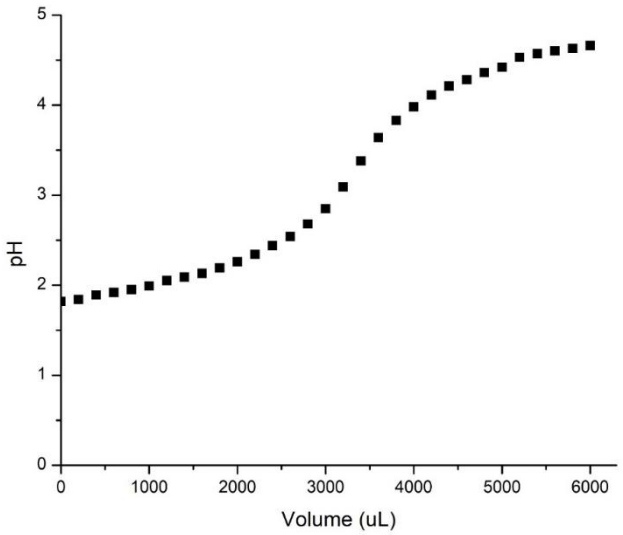

For GPC analysis, the chromatograms exhibited unimodal profiles as shown in Figure 13. The corresponding elution volume (Ve) and molar mass (MM) are detailed in Table 4.

Figure 13 – GPC curve for GM and OxGM solution in 0.1 mol/L $NaNO_3$.

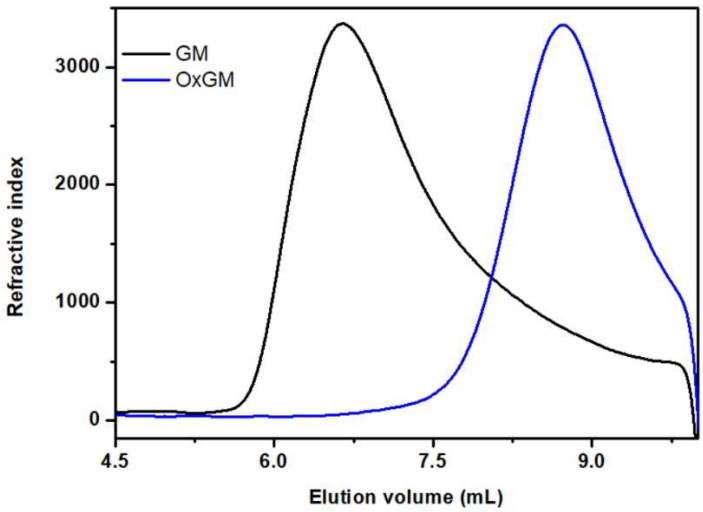

Table 4 – Values of Ve and MM for GM and OxGM

Sample	Ve (mL)	MM (Da)
GM	6.65	$5.31x10^6$
OxGM	8.72	$2.06x10^4$

Compared to GM, it was observed a decrease in the MW value for the oxidized derivative. Gomes; Rinaudo; Villar, (2007), had already reported a decrease in the molar mass of the oxidized alginate, due to the formation of free radicals, which cleave the chain of the functionalized polysaccharide. The most significant reduction was observed at the 50% degree of oxidation (2.3×10^5 to 3.5×10^4 g/mol) (Gomez; Rinaudo; Villar, 2007).

3.3 Fourier Transform infrared (FTIR) spectroscopy

The FTIR spectra of NSC, OxGM and freeze-dried hydrogels (75C25G, 50C50G and 25C75G) are shown in Figure 14. The bands observed at 3400 and 2927 cm^{-1} were attributed to the stretching of O-H and C-H bonds, respectively.

Characteristic bands associated with the pyranose ring were observed between 1160 and 1030 cm^{-1}, and were attributed to the stretching of C-O, C-O-C and C-C bonds (Oliveira *et al.*, 2023). The band at 1740 cm^{-1} for OxGM can be attributed to the stretching of the C═O linkage of the aldehyde groups (Carlos *et al.*, 2021). The stretching of the C═N imine bond (Schiff base) typically generates an absorption in the range of 1640 to 1690 cm^{-1}. However, this was difficult to distinguish due to the overlap with the amide band at 1660 cm^{-1} present in NSC. The absence of the band at 1740 cm^{-1} in the 75C25G spectrum may be attributed to its nearly complete consumption of aldehyde groups by the Schiff base reaction, in accordance with NH_2/CHO proportion of 9:10 showed in Table 3 (Maciel *et al.*, 2019).

Figure 14 ─ FTIR spectra of NSC, OxGM, 75C25G, 50C50G and 25C75G.

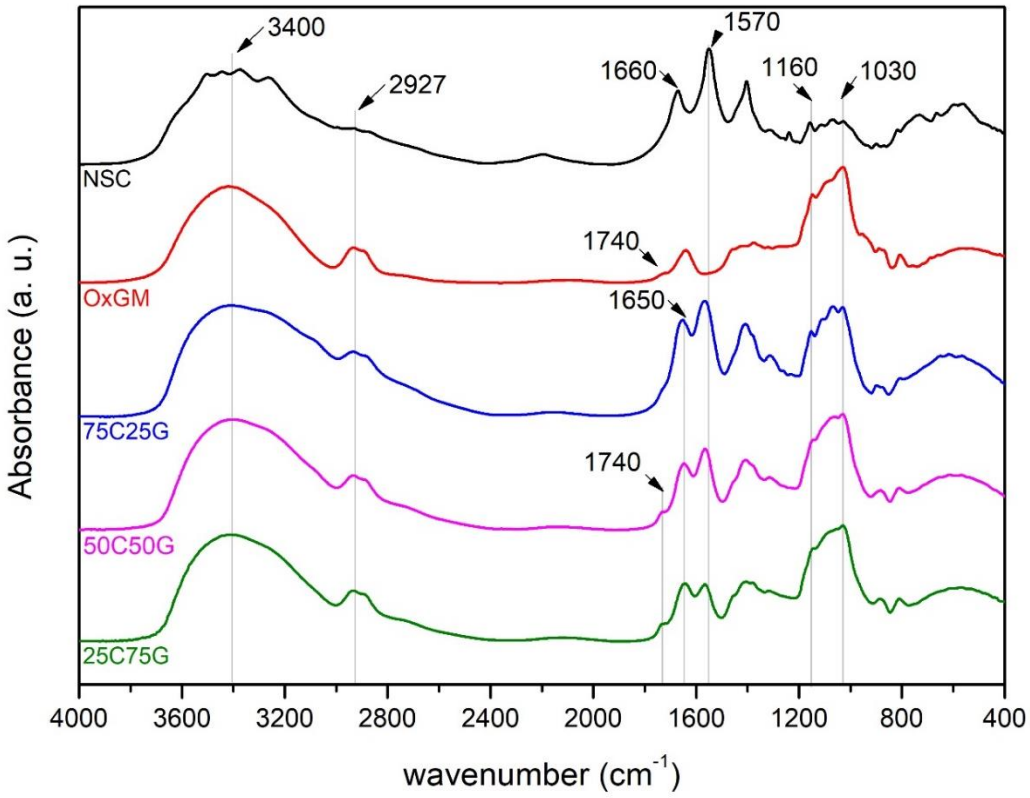

3.4 X-Ray Photoelectron Spectroscopy

The surface composition of both polymers and their blends was characterized by XPS survey analyses, and the results are presented in Table 5. While

the carbon and oxygen percentages were similar among all five samples, it should be noted that OxGM displayed a high oxygen amount due to the oxidation process. In addition, the presence of sodium in the atomic composition of NSC was attributed to the electrostatic equilibrium dynamics during the synthesis reaction, where pH was adjusted to 12, facilitating the formation of negatively charged COO^- groups. As might be expected, the hydrogels exhibited a higher amount of O and lower N percentage when OxGM content increased. The survey data cannot corroborate whether the crosslinking reaction occurred. Therefore, high-resolution spectra on C1s were done.

Table 5 ─ Atomic composition of biopolymers NSC, OxGG, and hydrogels 75C25G, 50C50G, and 25C75G obtained through XPS

	Atomic composition			
Sample	% C	% O	% N	% Na
NSC	59.6 (± 1.3)	30.4 (± 1.3)	4.6 (± 0.8)	5.5 (± 0.8)
OxGM	65.3 (± 0.7)	34.4 (± 0.6)	-	-
75C25G	63.0 (± 0.7)	31.4 (± 0.4)	4.4 (± 0.3)	2.2 (± 0.5)
50C50G	60.3 (± 1.3)	33.9 (± 0.9)	3.7 (± 0.5)	2.6 (± 1.3)
25C75G	61.5 (± 0.8)	37.1 (± 0.4)	1.4 (± 0.4)	-

In HR C1s, the peak centered at 288.3 eV in NCS was associated to *N*-succinyl group, O=C-NH_x, and the acetal moieties, C-O-C, of CS. The other peaks centered at 286.4 and 285.0 eV were attributed to C-N/C-O and C-C/C-H, respectively. For OxGM, the peaks centered at 285.0, 286.7 and 288.7 eV were associated with C-C/C-H, C-O and C=O/O-C-O (aldehyde group and acetal moieties), respectively. For NSC/OxGM hydrogels, the C 1s spectra were still deconvoluted in three peaks corresponding to C-C/C-H, C-O/C−N, and O=C-NHx/C-O-C/C=O groups from lower to higher binding energies, as for NCS and OxGM, but their respective proportions were different. In fact, when OxGM content was higher, the proportion of the peak at 286.5 eV from C-O/C-N bonds was higher, whereas the peak at 285.0 eV from C-C/C-H bonds decreased in 25C75G (52.4%), followed by 50C50G (43.0%), and was lowest

in 75C25G hydrogels (35.4%) (Figure 15). Surprisingly, 25C75G displayed a higher contribution of the band centered at 286.5 eV than crude OxGM, 52.4% versus 39.2%, and even higher than NCS, 36.5%. This could be correlated with the formation of imine bonds, whose binding energy ranged in this area (286.0-286.5 eV). In fact, higher is the concentration of OxGM, higher imine bonds could be formed. In addition, it is worth noting that the initial peak from OxGM at 288.7 eV was shifted to lower binding energies, 288.0-288.3 eV, meaning that the aldehyde contribution became negligible and acetals from OxGM and NCS predominate. Once again, this may be correlated with fact that the aldehyde groups from OxGM reacted with the amino moieties from chitosan, leading to imine formation (Zhou *et al.*, 2014).

Figure 15 ─ HR C 1s XPS spectrum of NSC, OxGM, 75C25G, 50C50G, and 25C75G samples.

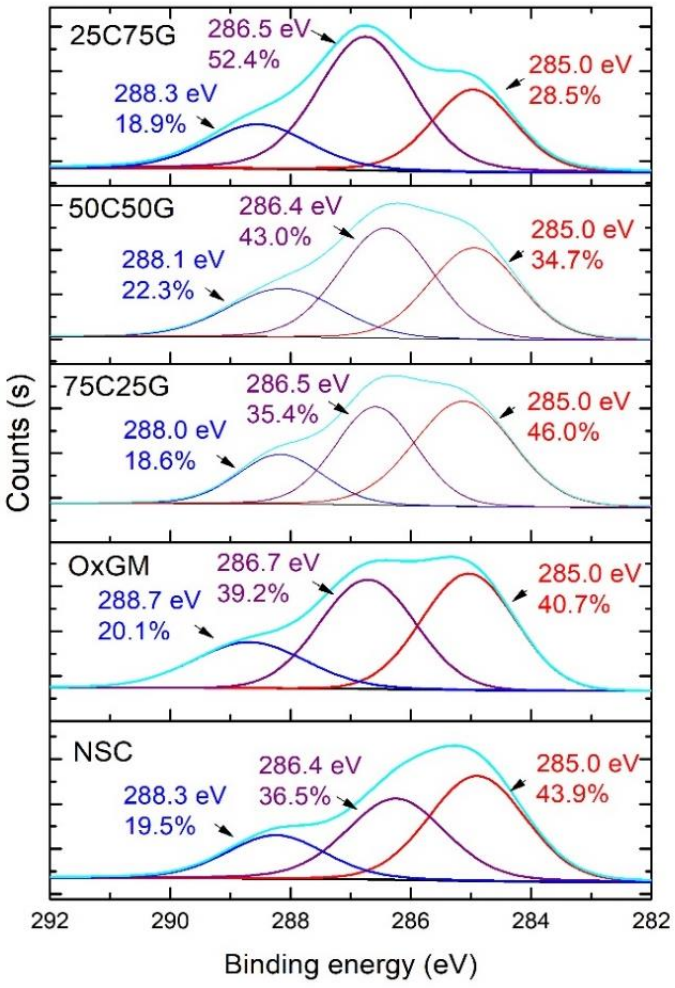

3.5 Thermogravimetric analysis (TGA)

The thermal stabilities of the NSC, OxGM, and (75C25G, 50C50G and 25C75G) hydrogels were analyzed by TGA and their thermogravimetric curves are shown in Figure 16A. The first peaks are related to moisture loss, and hydrogels presented the highest moisture loss compared to polymers, due to vaporization of water molecules trapped in the porous structure, which was still present after lyophilization.

Figure 16 ─ Thermogravimetric analysis (A) and derived weight (B) of NSC, OxGM, and (75C25G, 50C50G and 25C75G) hydrogels under synthetic air.

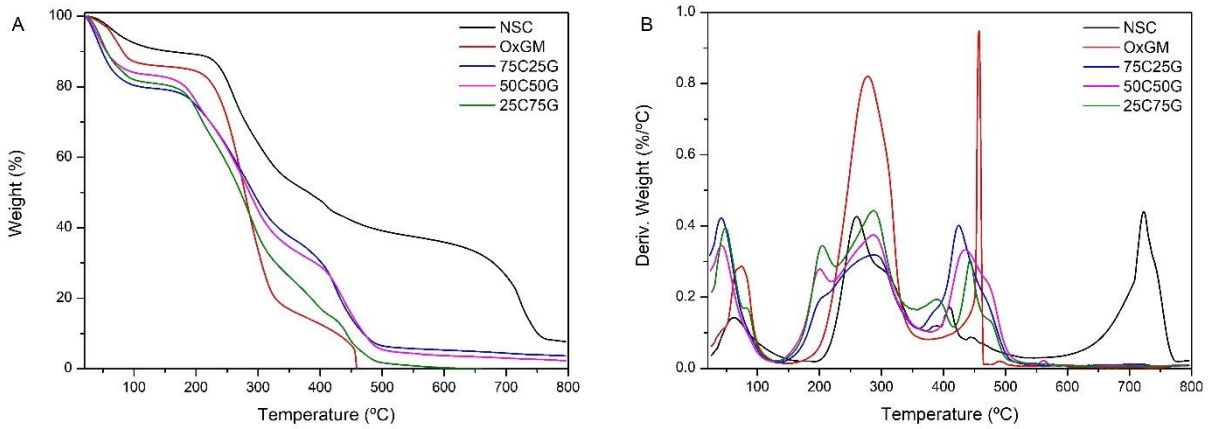

Increasing the NSC content decreased the thermal degradation, while more residue weight was left at high temperatures. The blends showed intermediate thermal stability between NSC and OxGM, due to relatively unstable Schiff's bases (-C=N-). The TGA profile of OxGM showed the largest weight loss (68%), corresponding to an exothermic event, detected by DTG analysis (Figure 16B) in the temperature range of 190 – 348 °C and attributed to the first thermal decomposition of the polysaccharide skeleton. OxGM presented the lowest thermal stability because of the cleavage of oxidized side chains (Rossi *et al.*, 2017). For NSC, a third stage of weight loss was observed in the range of 350 and 435 °C, due to the degradation of the succinyl group (pH responsive N-succinyl chitosan/Poly (acrylamide-co-acrylic acid) hydrogels and in vitro release of 5-fluorouracilBashir *et al.*, 2017). All samples exhibited a second

decomposition event, associated with the complete degradation of the polymer chains, occurring at temperatures ranging from 400 to 500 °C. The decomposition was more pronounced in samples with higher OxGM content, since the oxidized product showed less stability. The exothermic peaks are evident in the DTA profiles (Figure 16B) above 400 °C. NSC exhibited a high peak at 722 °C residual mass, probably due to salt formation (sodium succinate) during its modification (Table 6).

Table 6 ─ Thermal events of NSC, OxGM, 75C25G, 50C50G, and 25C75G according to temperature range (ºC) and mass loss (%)

	1st event		**2nd event**		**3rd event**	
Sample	Range (ºC)	Mass (%)	Range (ºC)	Mass (%)	Range (ºC)	Mass (%)
NSC	25–200	10.09	200-300	53.53	350-435	26.55
OxGM	25-200	14.19	200-400	74.66	400-460	10.41
75C25G	25-150	20.35	150-360	38.05	360-500	35.16
50C50G	25-150	15.72	150-360	49.41	360-500	29.59
25C75G	25-150	18.17	150-360	53.29	360-500	25.39

3.6 Gelation time via rheology

Time-dependent rheological behavior was assessed to investigate the influence and kinetics of crosslinking degree on the gelation. G' (storage modulus) and G" (loss modulus) values were measured during the crosslinking process. It is fundamental to examine how the degree of crosslinking affects the gelation time for the selection of an optimal formulation for future application. Optimal gelation time is crucial for successful application of hydrogels in biomedical contexts. If the gelation time is excessively prolonged, the hydrogel precursor solutions may disperse within the body before gel formation. Conversely, if the gelation time is too short, it can hinder the incorporation of other pharmaceutical reagents for therapeutic purposes, leading

to a loss of injectability. Thus, achieving an appropriate gelation time is essential, ensuring that the hydrogel allows for uncomplicated formulation and convenient administration under physiological conditions.

As illustrated in Figure 17, the storage modulus (G') of all pre-gel solutions gradually increased with time, which means that the pre-gel solution gradually became hydrogel, along with the formation of more Schiff base groups. This behavior also indicated that gelation could occur within a very short time. Among the hydrogels, 75C25G demonstrated its crossover point (G' = G'') at 80 s, whereas, for 25C75G and 50C50G, G' values surpassed the G'' values throughout the entire experimental period, which is a gelation time lower than 30 s. Such a change in gelation time in association with concentration is expected, as the gelation reaction is bimolecular and depends on the concentration of amines of NSC and aldehydes of OxGM. NSC/OxGM hydrogels were rapidly formed, mainly due to the Schiff base reaction between abundant aldehyde groups along the OxGM molecular chains and the amino groups on NSC. This fast and controllable gel formation ability is particularly important for biological applications as an injectable hydrogel (Li, S. *et al.*, 2020). Additionally, with the increase in NSC/OxGM molar ratio, the hydrogel displayed lower G' values, probably due to a slower crosslinking reaction in the hydrogel network.

Figure 17 — Evolution of storage (G') and loss (G'') modulus over time at 37 °C

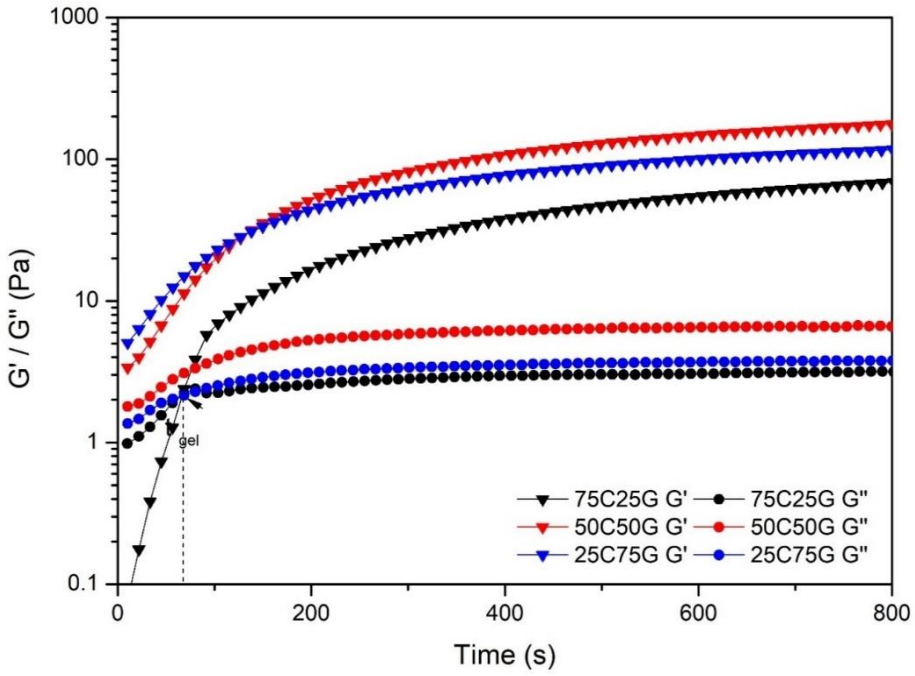

Hydrogels crosslinked through Schiff base reactions are reported to exhibit a gelation time of around 1 minute. This timeframe is dependent upon the polymer concentration, with higher solution concentrations correlating to shorter durations for phase transitions to occur (Yu, Z. J. *et al.*, 2023). However, an even faster gelation time (t_{gel} = 20 s) was obtained by Liu *et al*, 2020 (Liu, J. *et al.*, 2020) for hydrogels based on carboxymethyl chitosan and aldehyde hydroxyethyl starch.

3.7 Evaluation of swelling degree

The swelling equilibrium of hydrogels is an important parameter for their biological application, as highly swollen hydrogels are capable of retaining and absorbing large amounts of tissue fluids and nutrients. Furthermore, swelling facilitates both cell attachment and penetration during the process of tissue regeneration (Li, J. *et al.*, 2020). Figure 18 shows the swelling ratio of lyophilized hydrogels in PBS. All samples exhibited a significant increase in swelling rate within a short time period (t< 30 min). This rapid swelling is attributed to the scaffold's high porosity, as detailed in the morphology section, facilitating fast penetration of PBS into its structure. Subsequently, equilibrium was reached at approximately 3 hours. The rehydrated material preserved its original shape (cylindrical) and did not demonstrate any erosion/fragmentation during the swelling process due to the crosslinked network formation. All developed hydrogels presented high equilibrium fluid content, with swelling between 32 and 37 times its initial mass, suggesting that they could maintain a significant amount of body fluid when applied *in vivo*. These materials presented high swelling rates due to the presence of hydrophilic groups in the NSC and OxGM structures. The equilibrium PBS content decreased gradually with OxGM content, indicating that the retaining capacity was also dependent upon the degree of cross-linking and the polymer volume fraction of NSC and OxGM. The 75C25G hydrogel had a slightly higher capacity to retain PBS.

In general, the swelling ratio is dependent upon, not only the degree of cross-linking, but also the volume fraction of polymers, since these have different water affinities. A greater density of crosslinking sites or volume fraction will lead to a lower swelling ratio. Similar swelling results were obtained by Lin Jun *et al.* (Li, J. *et al.*, 2020), where lyophilized hydrogels consisting of oxidized hydroxyethyl starch (O-HES)

and modified carboxymethyl chitosan (M-CMCS) showed great swelling capability. As the volume fraction of the O-HES increased, both the swelling ratio and equilibrium water content decreased gradually.

Figure 18 ─ Swelling behaviors of the NSC/OxGM hydrogels with different polymer ratios in PBS buffer (0.01 M and pH 7.4).

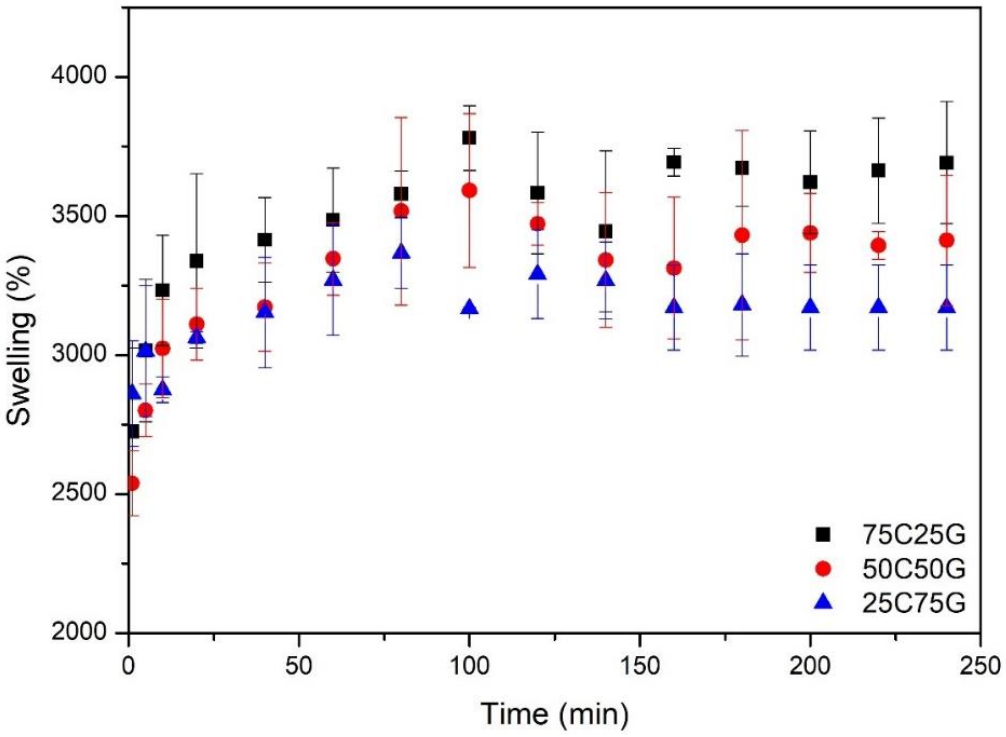

3.8 *In vitro* biodegradation study

Biodegradation is an important property required for the ideal scaffold and hydrogel, where the rate of degradation should be similar to that of tissue generation, as well as for a more controlled drug delivery. The *in vitro* biodegradation of NSC/OxGM freeze-dried hydrogels in PBS without and with lysozyme was observed for 28 days and is shown in Figure 19. During the entire experimental period, all formulated NSC/OxGM hydrogels degraded over time. The cylindrical samples were observed to erode from the surface to the core, decreasing in volume with time.

Figure 19 ─ Weight loss (%) related to the degradation of the different freeze-dried hydrogels in PBS and PBS/Lysozyme (*) over 28 days.

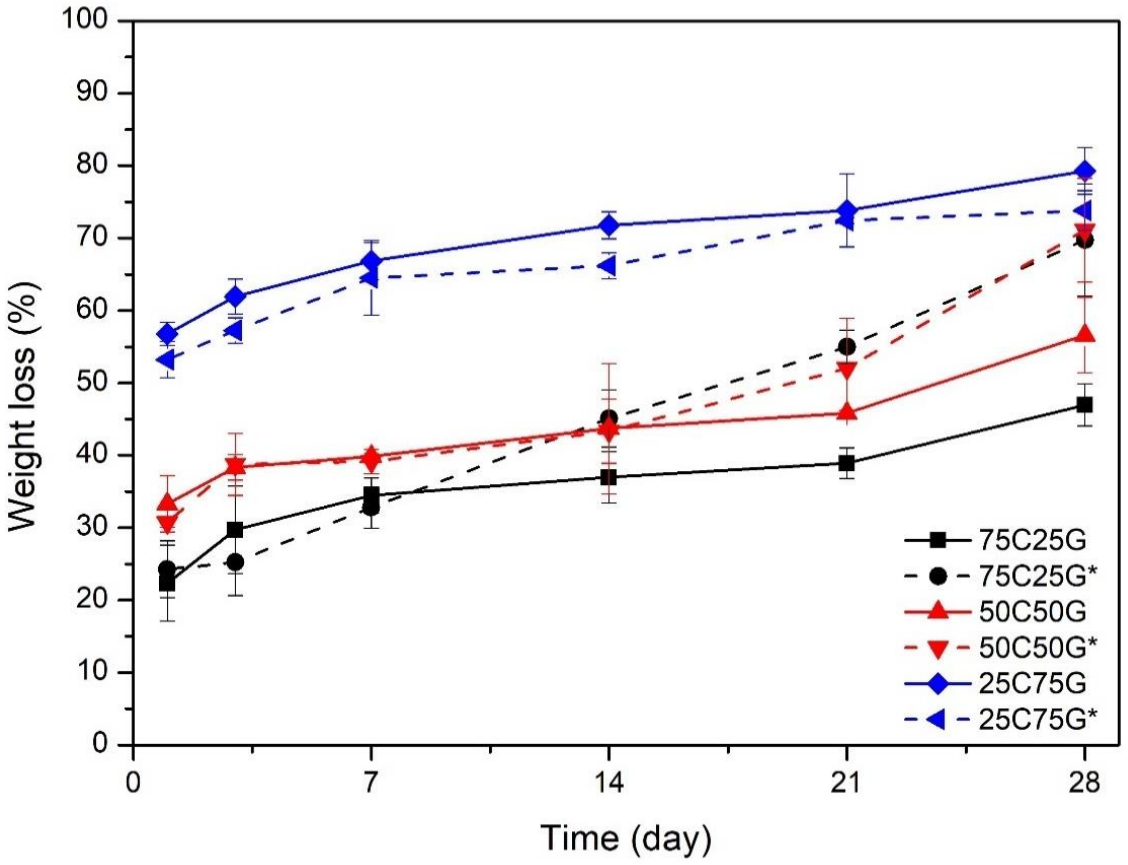

After 28 days, the 75C25G hydrogel presented the lowest degradation rate (46.7 ± 2.9 % / 69.8 ± 7.7 %), the 25C75G hydrogel had the highest (79.2 ± 3.2 / 73.8 ± 2.8 %) and the 50C75G hydrogel presented an intermediate behavior (56.6 ± 5.2% / 71.1 ± 7.2 %). Hydrolysis of the Schiff bond is the primary mechanism of the degradation of NSC/OxGM hydrogels, as the cross-linking reaction is reversible. Therefore, the degradation of the hydrogels depends upon the accessibility of water to the polymeric matrix. Additionally, OxGM that is not crosslinked might be solubilized. Dialdehyde polysaccharides, modified by ring-opening oxidation, are reported to be more susceptible to hemiacetal hydrolysis and β-elimination in alkaline medium (Hozumi *et al.*, 2018).

There were two distinct phases of degradation process in PBS/lysozyme medium. During the first 7 days, there was an insignificant change in the degradation profile, compared to PBS, ascribed to the hydrolysis of hydrogels, a rapid degradation

process, which included the physical process of dissolution and the cleavage of three-dimensional polymer network structure. Over the following days, weight loss changed significantly with the presence of the enzyme, ascribed to chemical degradation of the chitosan backbone, since this lysozyme is known to hydrolyze linkages between the glucosamine-glucosamine units (Liu, J. *et al.*, 2020; Lončarević; Ivanković; Rogina, 2017).

Moreover, the content of the aldehyde and amino groups significantly influenced the degradation rate of hydrogels. As the amino groups from NSC increased, the degradation rate decreased. This phenomenon is related to the crosslinking density, since a high crosslink density can slow the degradation process. As the number of amino groups increased in the hydrogel, more crosslinking sites were formed.

3.9 Morphology and porosity

The morphology of the freeze-dried hydrogel was evaluated during the degradation process by SEM images, which are shown in Figure 20. In order to promote adequate tissue growth and good drug diffusivity, the biomaterial should contain a porous and interconnected network, which are important factors for cell adhesion, proliferation, and for stimulating the diffusion and exchange of nutrients and oxygen (Sivashankari; Prabaharan, 2020).

The average pore diameter of samples was manually measured using ImageJ® software (Table 7). The scaffold pore size decreased from 186 ± 45 µm to 84 ± 20 µm with the addition of OxGM, with an intermediate value of 118 ± 44 µm (Figure 21). According to Perez and Mestres (Perez; Mestres, 2016), the optimal pore size for scaffolds used in musculoskeletal tissue engineering falls within the range of 100 and 400 µm. Within this range, scaffolds may facilitate integration with the host tissue and increase the chances for key processes such as blood vessel neogenesis. Therefore, the 75C25G scaffolds would be ideal for this application, as they exhibited pores within this recommended range.

Figure 20 – SEM images of different volumetric ratios of NSC/OxGM during the degradation process in PBS/Lysozyme media (4.0 kV, 500 µm)

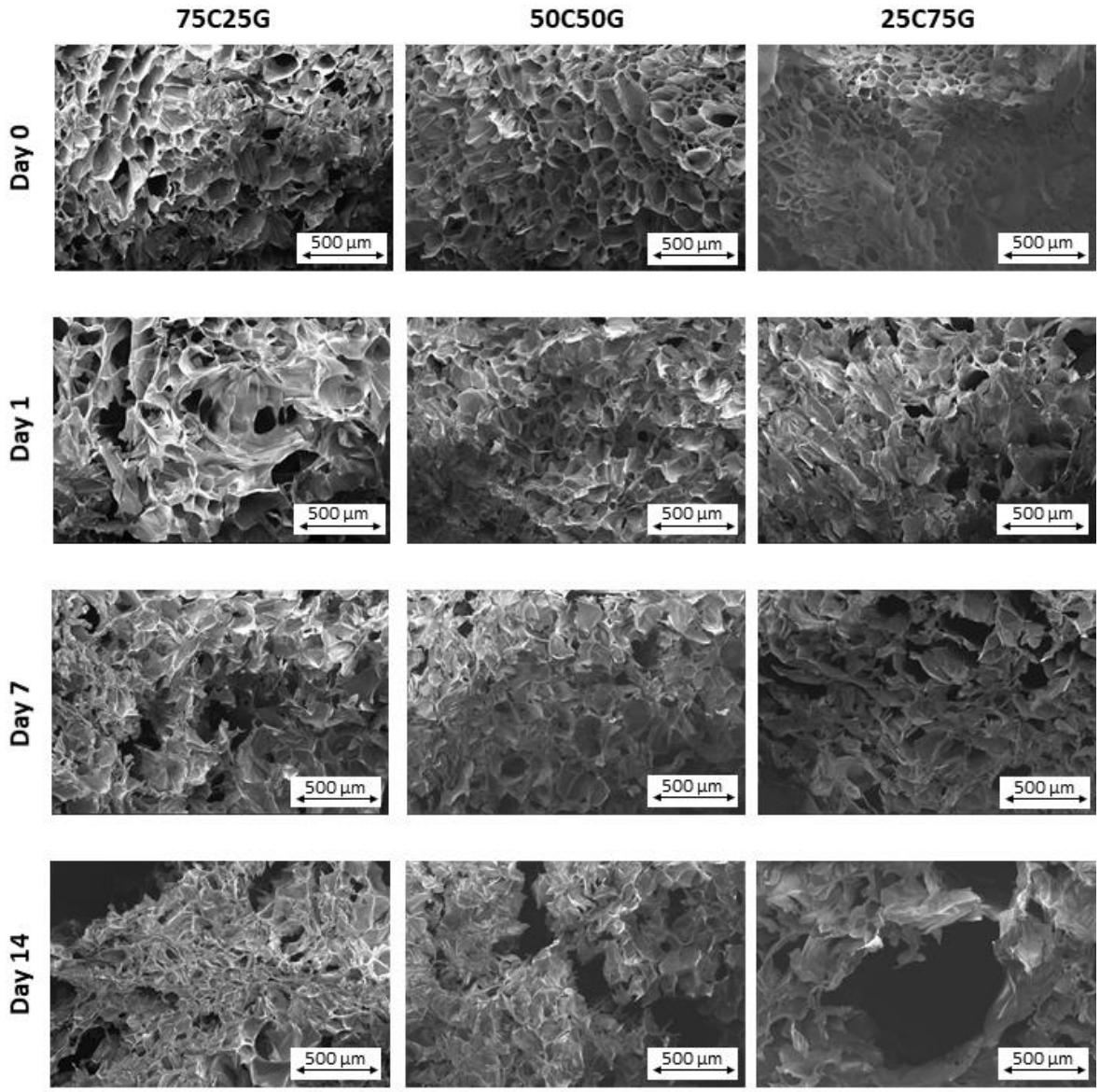

The SEM images of NSC/OxGM hydrogels before degradation showed that the two polymers were uniformly distributed in the polymeric matrix and that their components were tightly connected, since there were no evident empty spaces (bubbles) or color contrast between them. After degradation, the materials presented a clear surface collapse, forming a ‘donut-like’ shape. The morphology changes indicated that the NSC present on the surface was easily accessible to the lysozyme and was partially degraded.

Figure 21— Pore size distribution for the different ratios of the freeze-dried hydrogels

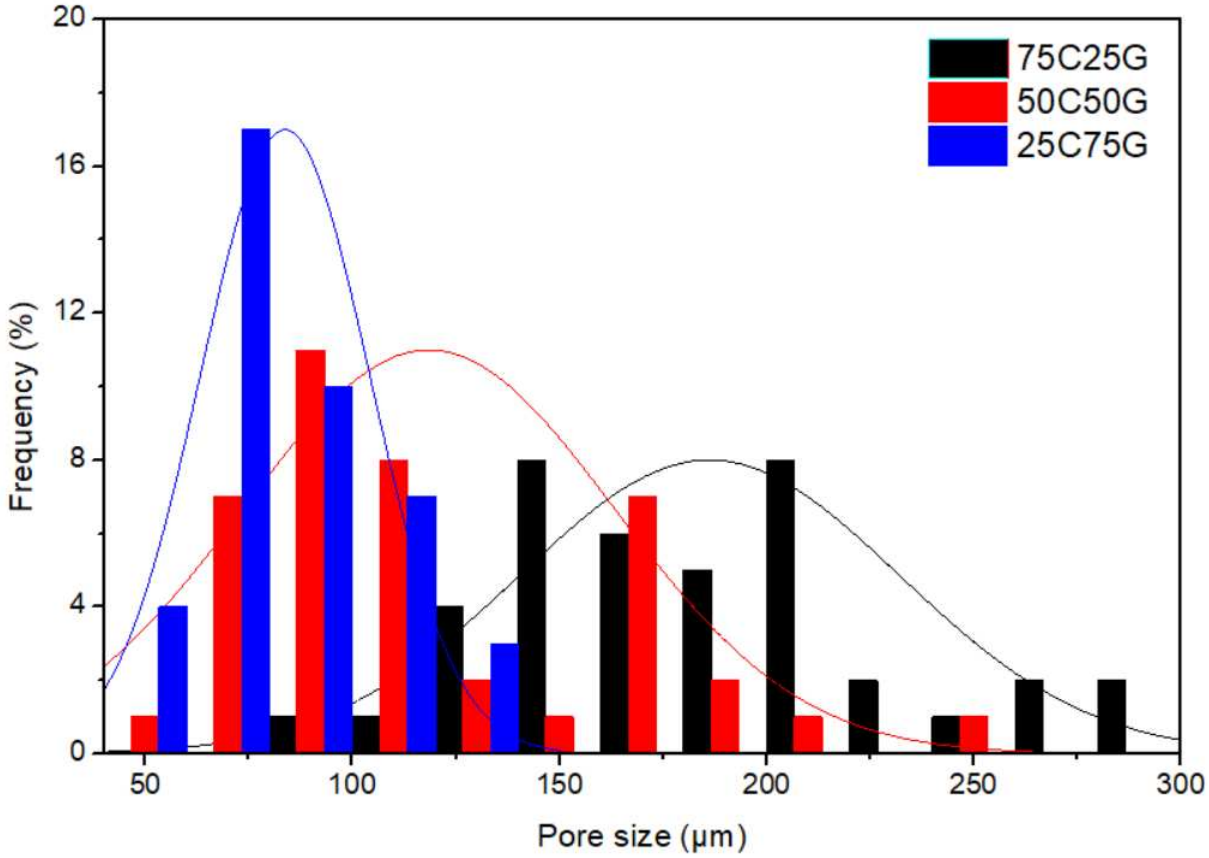

The liquid displacement method was used to determine the porosity of the 75C25G, 50C50G and 25C75G freeze-dried hydrogels. The 75C25G hydrogel had the lowest porosity (26.6 ± 3.5%) and the 25C75G hydrogel had the highest (52.7 ± 0.7%). This observation confirmed that higher amino groups available for the crosslinking greatly influenced the porosity of the freeze-dried hydrogels. The higher crosslinking density of 75C25G hydrogel resulted in the formation of smaller pore diameters and a denser network structure (Li, S. *et al.*, 2020). Similar results were observed by Xin Meng *et al.* (Meng *et al.*, 2021), who, using the same methodology, showed that porosity significantly decreased when the chitosan content increased, in chitosan/alginate/hyaluronic acid material.

Table 7 ─ Porosity and average pore size, determined by liquid displacement and measured by ImageJ® software, respectively

Sample	Porosity (%)	STD (%)	Avg Pore size (μm)	STD (μm)
75C25G	26.6	3.5	186	45
50C50G	40.8	1.6	118	44
25C75G	52.7	0.7	84	20

3.10 Indirect cell viability

The cytocompatibility of the developed hydrogels was firstly evaluated via an indirect cytotoxicity assay using L929 fibroblasts. The cell viability after contact with the material extracts of the hydrogels is shown in Figure 22. The 75C25G and 50C50G hydrogels presented low cytotoxicity, where the fibroblast cell viabilities were 91.5% and 82.1%, at 24 h, and 108.8% and 92.9%, at 48 h, respectively. According to ISO 10993-5, the hydrogels were considered to be non-cytotoxic materials (cell viability > 70%) (Biological Evaluation of Medical Devices—Part 5: Tests for In Vitro Cytotoxicity, 2009). Cell viability increased with time, which was a considerable advantage, and there was no significant difference in cell viability between the times. Findings indicated that these two hydrogels were able to promote cell growth, instead of being toxic to the cells, showing that these two natural polysaccharides were still biocompatible after crosslinking via the Schiff base reaction. As such, these hydrogels could be safely used for biomedical applications. Co-culture of the fibroblasts with the 25C75G hydrogel resulted in a cell viability of 67.1% at 24h and 56.9% at 48 h, representing the lowest cell viability out of the three samples.

Cell viability decreased in association with the increase in the OxGM concentration. As previously explained, 25C75G had the highest degradation rate due to low crosslinking density, increasing the concentration of free aldehyde groups in the extract. These aldehyde groups might have bonded with the primary amine functional groups of proteins in the cell membrane, which could have damaged the cells and

affected the cell proliferation (Aziz *et al.*, 2015; Zhang *et al.*, 2020). Several oxidized polysaccharides are reported to cause cytotoxicity related to the higher oxidation degree (Muhammad *et al.*, 2020). NSC has no significant cytotoxicity, as reported by Tang *et al.* (Tang *et al.*, 2016) using the L929 cell line and the MTT assay. Similar results were observed with N-succinyl-chitosan and oxidized carboxymethylcellulose hydrogels, using HEK 293 cells, where the higher aldehyde content slightly decreased cell viability (Lü; Liu; Ni, 2010).

Figure 22 ─ Cell viability of the L929 fibroblasts cells when co-cultured with the studied hydrogels for 24 and 48 h (in % compared to DMEM control, n= 4) (*p < 0.05)

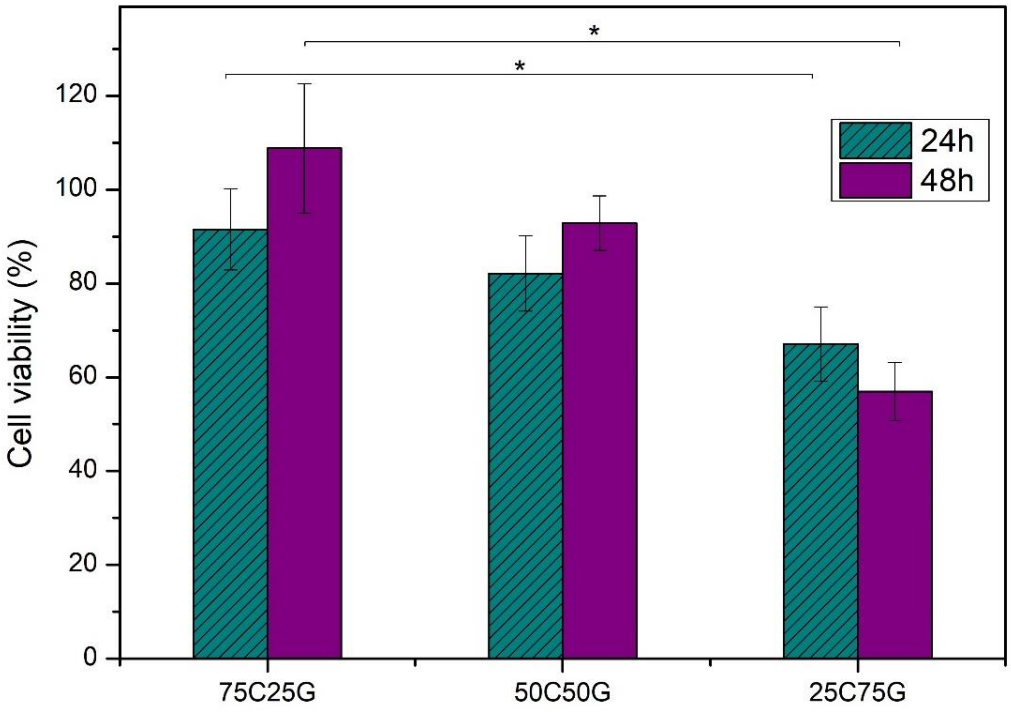

3.11 Direct cell viability

To assess the interaction between the fabricated hydrogel and cells, the viability of neo–Human Dermal Fibroblasts (nHDF) was evaluated in direct contact with the hydrogels. Fibroblasts were seeded onto the hydrogel surface, and cell viability was measured after 1, 2, and 3 days of culture to monitor cell adhesion and proliferation. On the first day, viability results were primarily associated to the ability of

cells to anchor to the matrix and spread. Cell adhesion to hydrogels involves various membrane receptors (Palladino *et al.*, 2023). While the high-water content in hydrogels is crucial for nutrient transport, chemical signaling, and metabolite exchange, it can negatively affect cell adhesion. The highly hydrated surface of the hydrogels creates an environment where cells perceive it as a water or liquid surface, hindering attachment and leading to reduced cell viability (Gao *et al.*, 2014).

As shown in Figure 23, during the first 24 hours, the 50C50G and 25C75G hydrogels exhibited the highest cell viability. This observation may be attributed to effective interactions between the cells and the hydroxyl, epoxy, and carboxyl groups present in OxGM. Additionally, the polycationic nature of chitosan macromolecules might interact electrostatically with fibroblast membranes, potentially interfering with cell adhesion (Veleirinho *et al.*, 2013). At later time points, the number of cells decreased for 25C75G and 50G50C, likely due to the toxicity of aldehyde groups released by the high OxGM content in these hydrogels.

Figure 23 ─ Direct cell viability of the nHDF fibroblasts (in % compared to DMEM control, n= 4) (*p < 0.05)

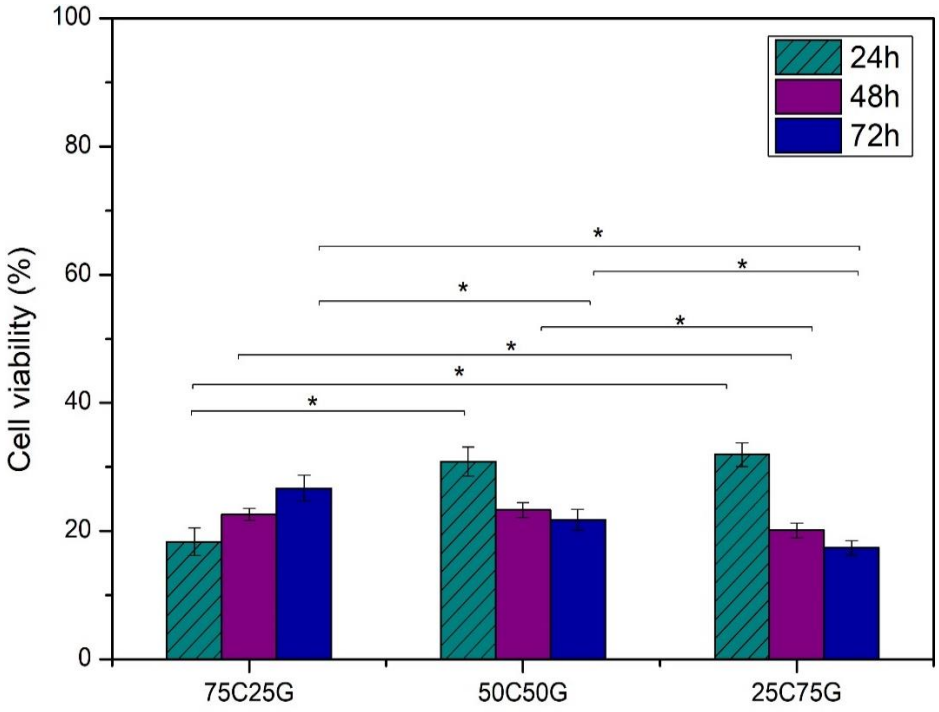

The hydrogels demonstrated a gradual breakdown that correlated with the increase in culture time with cells (data not shown). This was likely due to the combined

effect of hydrolytic degradation and enzymes produced by the fibroblasts, which accelerated the degradation of the hydrogel's polymer network structure (Weng *et al.*, 2008). Despite the reduced cell viability, fibroblasts on the 75C25G hydrogel continued to proliferate over the 72 hours of culture, as shown by the relative cell population growth (Figure 24).

Figure 24 – Relative cell population growth compared to day 1 (24h)

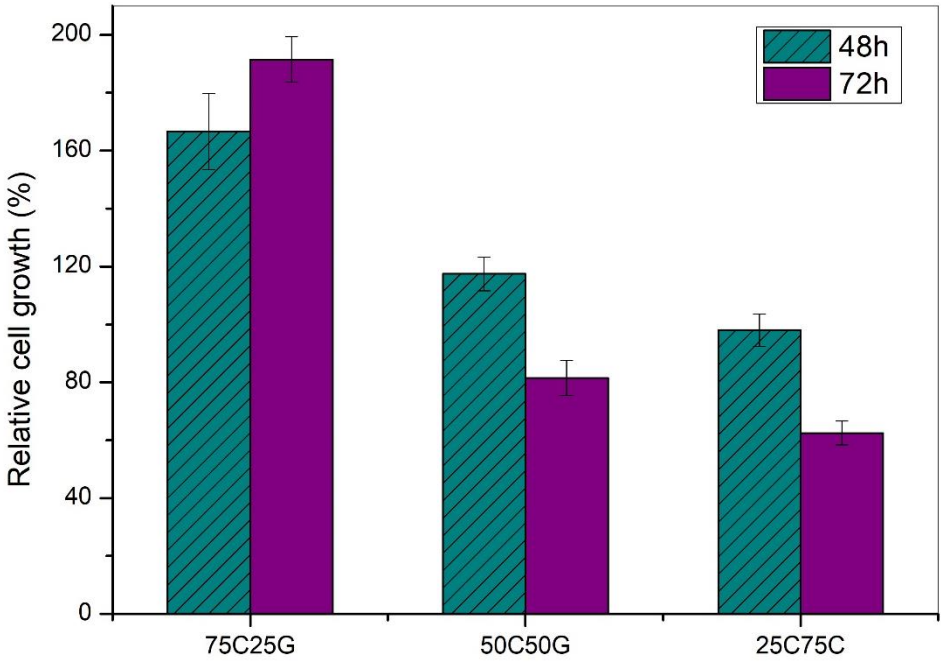

3.12 Mechanical properties of hydrogels

The ability to withstand substantial stresses and to restore the material structure upon unloading is crucial for the repair of load-bearing tissues. These tissues are frequently subjected to various stresses over time, making resilience an essential characteristic for effective repair.

The compressive mechanical behavior of the hydrogels in shown in Figure 25. Young's modulus values of 67.2 kPa (±8.5) and maximum stress of 30.0 kPa (±5.7) were obtained. These values are consistent with those reported by Cui *et al*, 2023 (Cui; Zhang; Coseri, 2023), who obtained a compressive strength of 51.3 kPa in a hydrogel based on gelatin and oxidized alginate, crosslinked by the Schiff base reaction.

Additionally, authors of this study enhanced the mechanical properties of such hydrogels by employing cellulose fibers as reinforcement, which represents an interesting strategy to overcome low mechanical values.

Figure 25 ─ Representative compressive stress-strain curve for 75C25G hydrogels

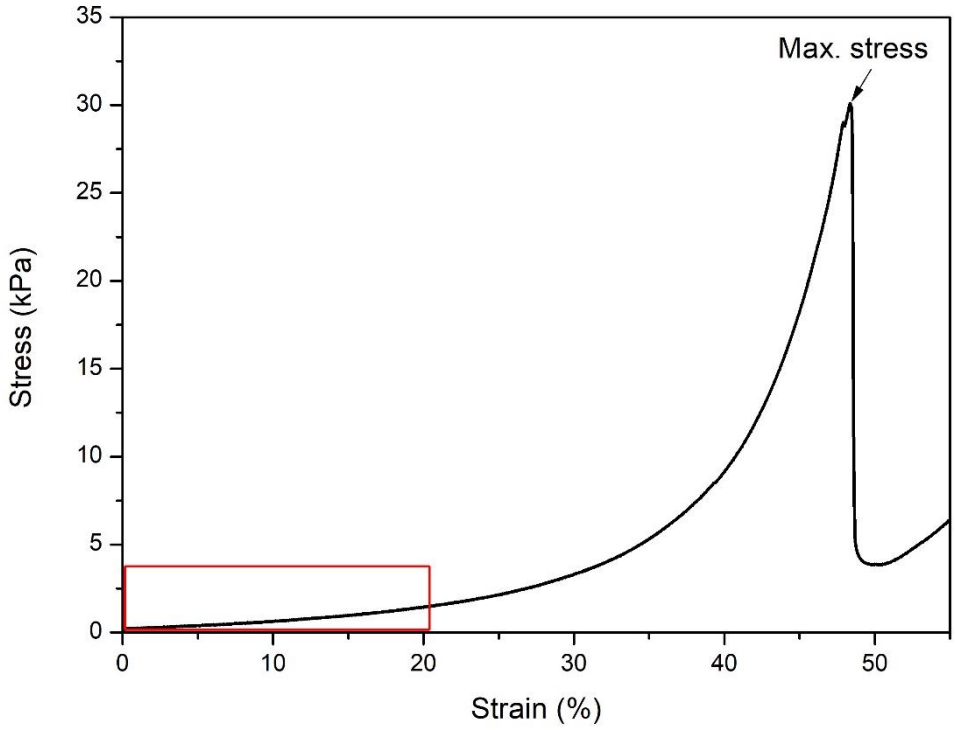

Self-healing hydrogels offer a promising solution for injecting materials. For instance, the material can infiltrate irregular bone defects, even in very narrow sites, and then reform to form a complete hydrogel in the target zone, which is crucial for effective bone repair (Huang *et al.*, 2021). In this study, two semicircular hydrogels merged to form an intact disk, demonstrating remarkable resilience against gravity and stretching in a direction perpendicular to the cutting plane, without exhibiting any signs of cracking (Figure 26).

Figure 26 — Self-healing behavior of 75C25G hydrogels

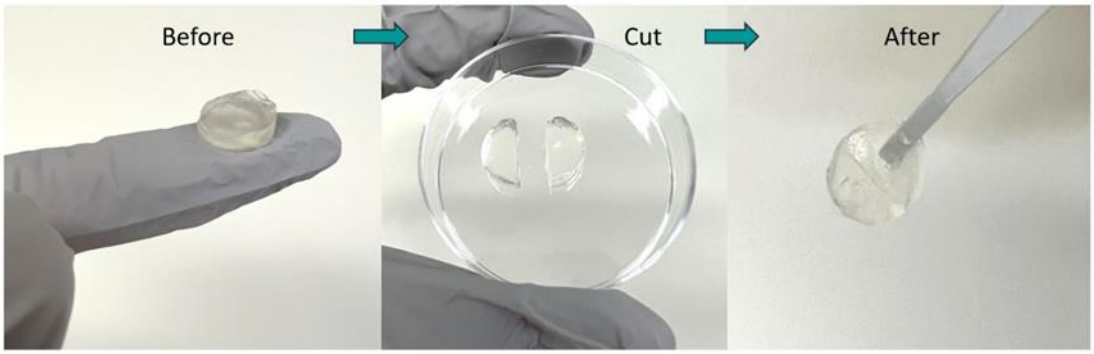

4 CONCLUSION

In this comprehensive study, we demonstrated the potential of two natural-based polymers, specifically guar gum (GM) modified into OxGM through periodate oxidation, serving as a macromolecular crosslinking agent for N-succinyl chitosan (NSC) via the Schiff base reaction. The hydrogels were fabricated using different functional group ratios, directly influencing the crosslinking degree. The physicochemical characterization through FTIR, TGA, XPS, swelling and SEM provided a profound understanding of the polymetric matrix. We evaluated the biodegradability and biocompatibility of the hydrogels and looked at how the crosslinking density affects these properties. Mass variation in PBS/Lysozyme assessed the biodegradability, revealing that hydrogels with a higher availability of amine groups for crosslinking displayed lower degradation rates and reduced porosity. Concurrently, cell viability studies demonstrated that, overall, the hydrogels were non-cytotoxic when co-cultured with a fibroblastic cell line. Hydrogels with higher crosslinking density favored better cell viability. Nevertheless, an increment in OxGM content correlated with a slight decrease in cell viability, due to the increased number of free aldehyde groups. The 75C25G hydrogel exhibited Young's modulus values of 67.2 kPa (±8.5). Hence, 75C25G formulation proven biodegradability, non-cytotoxic characteristics, and customizable properties make this hydrogel highly promising candidate for diverse applications, including regenerative tissue engineering and controlled drug delivery.

CHAPTER 2: LIDOCAINE RELEASE FROM INJECTABLE HYDROGEL BASED ON CHITOSAN / GUAR GUM FOR POSTOPERATIVE PAIN MANAGEMENT

ABSTRACT

Local anesthetics are widely used for pain management, particularly in post-surgical musculoskeletal cases, by blocking nerve impulse transmission. However, conventional applications often face limitations such as short half-lives, local side reactions, and systemic toxicity. To overcome these challenges, controlled *in situ* administration using injectable hydrogels emerges as a promising solution. These hydrogels offer excellent biological performance, providing less invasive applications that improve pain management, enhance patient safety, and increase comfort. This study investigated injectable hydrogels composed of *N*-succinyl chitosan (NSC) and oxidized galactomannan (OxGM), crosslinked through a Schiff base reaction, as carriers for local anesthetic lidocaine. The hydrogels were characterized using FTIR, TGA, and SEM analyses. In vitro lidocaine release in PBS was monitored, with the kinetics fitting the Korsmeyer-Peppas model, demonstrating sustained drug release potential. This novel hydrogel formulation represents a promising solution for improving local anesthetic delivery, addressing key limitations of traditional methods.

Keywords: Biomaterial; injectable hydrogel; anesthetic; drug delivery kinetics.

1 INTRODUCTION

Pain in the musculoskeletal region can cause inconvenience for patients who have undergone a surgical procedure, such as total or partial knee or hip replacement, shoulder repair and fracture correction. A variety of medications are available to patients dealing with postoperative pain, such as acetaminophen, non-steroidal anti-inflammatory drugs, corticosteroids, anesthetics, and opioids (Sun *et al.*, 2020). However, most of these treatments fail to effectively control the local pain and may even result in severe side effects after prolonged use, such as cardiovascular events, opioid dependence, and mortality (Costa *et al.*, 2021).

Local anesthetics are the most commonly used to alleviate pain. They can be administered locally for more immediate action. Traditionally, its application requires continuous infusions or repetitive injection to achieve the desired effect, which can lead to short effect duration, local tissue site reaction and systemic toxicity, since they are quickly absolved by the surrounding tissues and eliminated from the systemic circulation (Al Homsi *et al.*, 2022; Khanal *et al.*, 2018).

Local anesthetic molecules typically consist of three structural components: a hydrophilic amine group, a lipophilic aromatic ring, and an intermediate chain that contains either an amide or an ester group. Molecules containing an amide group have been found to be more stable and carry a lower risk of allergic reactions compared to those with an ester group. These anesthetics work by diffusing through the plasma membrane and reversibly blocking the sodium channels of neurons, thereby inhibiting the propagation of nerve impulses and resulting in both motor and sensory blockade (Shah; Votta-Velis; Borgeat, 2018).

Lidocaine (LD) is a widely used local anesthetic amide that serves as an ideal model molecule for studying hydrophobic drug binding due to its low molecular weight, as shown in Figure 27, and poor water solubility. Its clinical application is favored because of its efficacy, rapid controlled release, moderate duration of effects, and topical anesthetic activity (Physicochemical and pharmacological investigations of polyvinylpyrrolidone - tetrahydroxyborate hydrogel containing the local anesthetic lidocaineLi *et al.*, 2021).

Despite the benefits of using local anesthetics for the treatment of chronic and acute pain, the use of these drugs can lead to large fluctuations in blood plasma concentration levels, consequently causing side effects in patients (Tu, 2017). Therefore, the development of a local delivery system that manages to retain these molecules for longer time and releases them in a controlled manner could significantly increase its efficiency, minimizing the number of injections and reducing side effects.

Figure 27 ─ Chemical structure of lidocaine molecule

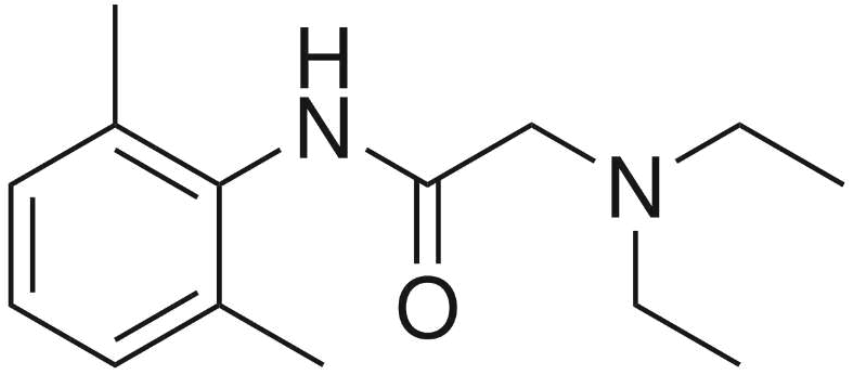

Source: MedChemExpress

Injectable hydrogels are gaining interest as minimally invasive carriers for sustained local anesthetic release due to its unique properties that facilitate the entrapment, adhesion and permeability of drug molecules, which enhance their drug loading capacity and control release at predetermined rate (Kesharwani *et al.*, 2021).

Many injectable hydrogels based on natural polymers have been extensively studied for the sustained release of local anesthetics. These systems and their specific features, as reported in the literature, are systematically summarized in Table 8. Different crosslinking agents, such as calcium for alginate and enzymes for chitosan, have been employed to simulate *in vitro* the release of local anesthetics from the polymeric matrix. Numerous studies have utilized *in vivo* anesthetic models, demonstrating the excellent biocompatibility of these hydrogels and their effective ability to induce local anesthesia. (Davis *et al.*, 2020; Khanal *et al.*, 2018; Qiao *et al.*, 2022).

Table 8 – Summary of the reported natural polymer-based injectable hydrogels for local anesthetic delivery system

Injectable hydrogel	**Anesthetics**	**Comments**	**Ref**
Alginate / Graphene oxide	Lidocaine	Good biocompatibility biodegradability and controlled release	(Luu *et al.*, 2022)
Carboxymethyl chitosan / Alginate	Lidocaine	Prolonged in vitro release and non-toxicity	(Wu *et al.*, 2023)
Chitosan/ Graphene oxide	Bupivacaine	Sustained release *in vitro* and *in vivo*.	(Al Homsi *et al.*, 2022)
Hydroxypropyl chitin / Hyaluronan	Ropivacaine	Great *in vivo* sciatic nerve blockage	(Qiao *et al.*, 2022)
Hyaluronic acid	Bupivacaine	Drug- loaded lipid emulsion and increased *in vivo* anesthetic effect	(Davis *et al.*, 2020)
Glycol chitosan	Ropivacaine	Sustained release from the hydrogel carrier *in vitro* and *in vivo*	(Khanal *et al.*, 2018)

Source: Own elaboration

Selecting an optimal drug delivery system is challenging, as multiple factors can simultaneously impact delivery efficiency. Therefore, further systematic research is essential to develop hydrogels that are clinically viable for local anesthetic delivery.

In this study, *N*-succinyl chitosan injectable hydrogel was developed using oxidized galactomannan as crosslinking agent and loaded with a local anesthetic (lidocaine) that can provide a sustained anesthetic effect to increase the efficiency of pain management in postoperative patients (Figure 28). This novel formulation uses Schiff's base reaction as the crosslinking process, which is a safe and rapid reaction,

an advantage over possible toxic crosslinkers.

Figure 28 – Graphical abstract of the studied injectable hydrogel being used as drug delivery carrier

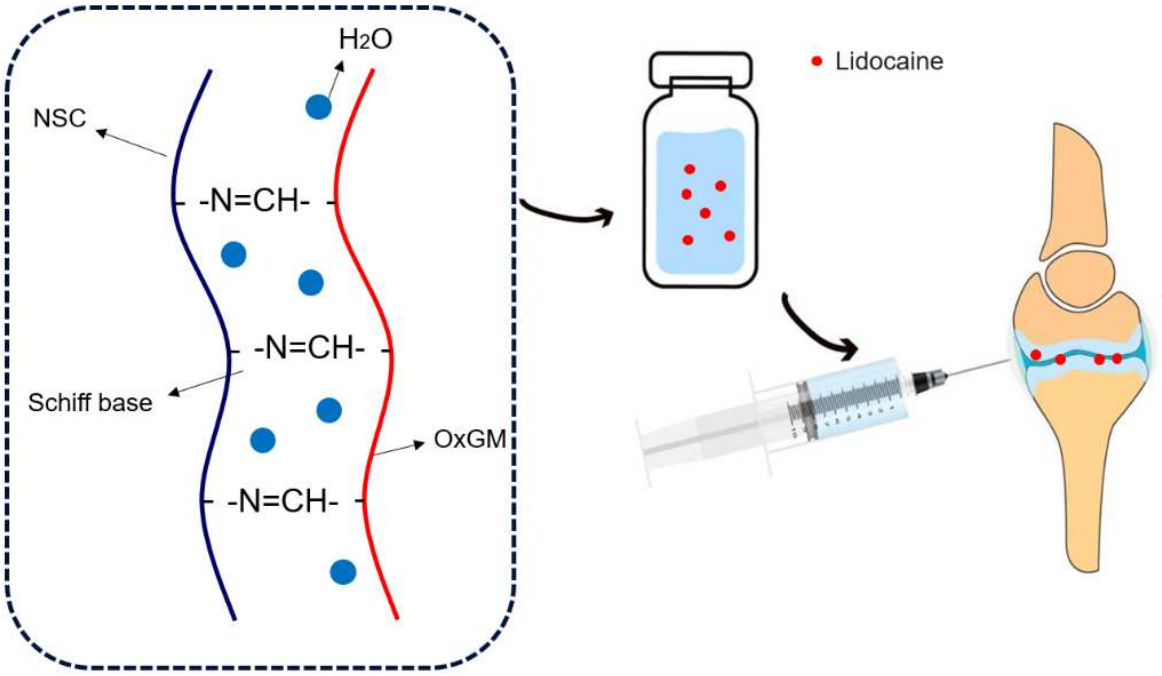

Source: Own elaboration

2 MATERIALS AND METHODS

All experiments were conducted at the Laboratory of Polymer (LabPol – DQOI-UFC) and the Laboratory of Biomaterials and Bioproducts (LPB – DEQ - UFC). The exception is the Scanning Electronic Microscopy (SEM) images, which were obtained at Laboratory of Biomaterials and Bioengineering (LBB - Université Laval, Canada).

2.1 Materials

Low molecular chitosan from shrimp shells (77% degree of deacetylation, Mw = 84.2 kDa), gum guar (galactomannan), and lidocaine were purchased from Sigma Aldrich, Brazil. Commercially available methanol, ethanol, acetone, ethylene glycol and glacial acetic acid were purchased from Synth, São Paulo, Brazil. Succinic anhydride (Sigma Aldrich, Brazil), sodium hydroxide (Vetec, Brazil), sodium periodate (Vetec, Brazil), and hydroxylamine hydrochloride (Vetec, Brazil) were all acquired in analytic grade (>99% purity).

.

2.2 Hydrogel formulation

NSC was dissolved in distilled water under continuous stirring at 50 °C for 30 minutes to obtain a 3% (w/v) solution, while OxGM was dissolved in distilled water at 60 °C for 24 hours to prepare a 2% (w/v) solution. For lidocaine incorporation, 20 mg of the drug was added to 100 mL of hydrogel precursor immediately before crosslinking and magnetically stirred to ensure homogeneous dispersion. The lidocaine concentration was selected to reach same levels commonly used in commercially available topical gel formulation for similar applications (Favatela *et al.*, 2021).

2.3 FTIR and TGA of lidocaine-loaded hydrogels

Lidocaine-loaded hydrogels underwent chemical characterization to determine any interactions between the drug and the polymeric matrix. The spectra of 75C25G hydrogel, pure lidocaine and lidocaine-loaded hydrogel were obtained using potassium bromide (KBr) pellets on the Shimadzu IR-Trace 100 spectrophotometer. The spectra were recorded in the wave number range of 4000 to 400 cm^{-1}. Thermogravimetric analysis (TGA) of the NSC/OxGM hydrogel, pure lidocaine and lidocaine-loaded hydrogel was conducted using a Mettler-Toledo model (TGA/SDTA) 851^e. Samples (~5mg) were weighed using an analytical mill, placed in an alumina crucible, and scanned from 25 to 800 °C at a heating rate of 10 $°C \cdot min^{-1}$ under oxidizing atmosphere (synthetic air).

2.4 Scanning Electronic Microscopy (SEM)

The morphology of the freeze-dried hydrogels was examined using scanning electron microscopy (SEM) with a Quanta-FEG FEI 450 instrument. Before imaging, the samples were sputter-coated with platinum/silver under an argon atmosphere using a Polaron SC500 Sputter Coater. The SEM images were obtained under a high vacuum by detecting secondary electron signals, with an acceleration voltage of 4 kV and a working distance of 10 mm.

2.5 *In vitro* lidocaine release

Lidocaine base was added to 1 mL hydrogel 75/25 NSC/OxGM for a drug formulation of 2% (w/v) and mixed by magnetic stirring. The *in vitro* lidocaine release from NSC:OxGM hydrogel was studied in PBS buffer (pH = 7.4) under sink condition. It was performed according to modified method described (Foley *et al.*, 2013). Hydrogels containing lidocaine were inserted into dialysis membrane (12,000 Da MWCO) with 5 mL PBS buffer and sealed. The dialysis bag was incubated in a 1 L

PBS bath at 37 ºC under shaking (100 rpm), as shown in Figure 29. At predetermined time intervals, samples (3 mL) were collected from the PBS bath and equal volume of PBS was replaced to maintain the total volume. The drug release was determined using UV-VIS spectrophotometer at 263 nm, while PBS was used as the reference standards. The release profile was mathematically analyzed using the Korsmeyer-Peppas model (Equation 1).

Figure 29 – Pictures illustrating the *in vitro* experimental release system

Source: Own elaboration

2.6 Cytotoxicity

Cell viability assay was performed to evaluate the biocompatibility and cell viability of NSC/OxGM hydrogel with and without lidocaine. For this purpose, L929 cell line (mouse fibroblast cells) was cultured at with DMEM media in CO_2 incubator at 37 °C for 24 h. And the extractives of the studied materials were used as culture for cells.

3 RESULTS AND DISCUSSION

3.1 FTIR and TGA of lidocaine-loaded hydrogel

The FTIR spectra of the NSC/OxGM hydrogel, lidocaine, and lidocaine-loaded hydrogel are shown in Figure 30. The characteristic bands of lidocaine appear at 3250 cm $^{-1}$ for N-H symmetric stretching; 2980 and 2910 cm^{-1} for CH stretching vibration; 2870 cm^{-1} for C-H stretching in $–CH_2$ group; 1670 cm^{-1} for C-O stretching; 1500 cm^{-1} for C=C stretching vibration in aromatic ring; and five bands between 1040 and 1210 cm^{-1}, attributed to CH in-plane bending. The 490 – 500 cm^{-1} region corresponds to C-N-C bending vibrations. In the FTIR spectrum of the lidocaine-loaded hydrogel, some distinctive lidocaine peaks show reduced intensity compared to the pure lidocaine spectrum. Notably, the C=C stretching vibration in the aromatic ring at 1500 cm^{-1} decreased in the lidocaine-loaded hydrogel. This reduction indicates weak interactions between the drug and hydrogel, such as van der Waals forces and hydrogen bonding, leading to a lower energy state and decreased peak intensity (Zhou *et al.*, 2022).

Figure 30 ─ FTIR of hydrogel (NSCOxGM), lidocaine (LD), and lidocaine loaded hydrogel (NSCOxGM+LD)

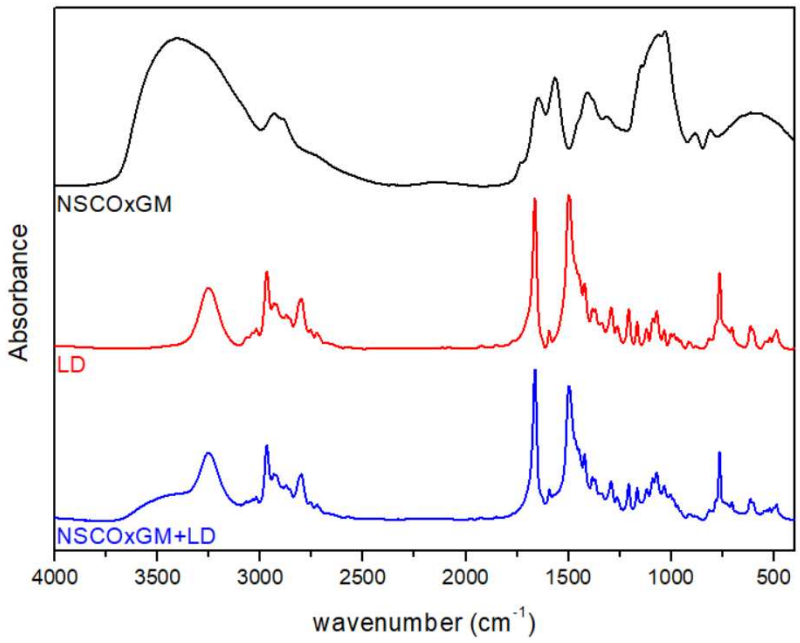

Figure 31 shows the TGA of the hydrogel (NSC-OxGM), lidocaine and lidocaine-loaded hydrogel. Lidocaine showed one thermal event with a weight loss of 99.5% at 217 °C. The same thermal event was observed in the lidocaine loaded hydrogel with a weight loss of 85.5% due to the significant amount of lidocaine (the system was freeze-dried). TGA thermograph showed weight losses below 100 °C due to water loss.

The thermal degradation process of the NSC/OxGM+LD hydrogel did not show significant differences compared to the pure hydrogel, indicating no strong or covalent interaction between the hydrogel matrix and the drug. TGA analysis of the lidocaine-loaded hydrogel revealed that the stability of lidocaine remained unchanged compared to its free form. Any minor variations in thermal behavior could be attributed to the physical encapsulation of lidocaine within the hydrogel network, rather than chemical modifications.

Figure 31 – TGA of hydrogel (NSCOxGM), lidocaine (LD) and lidocaine loaded hydrogel (NSCOxGM+LD)

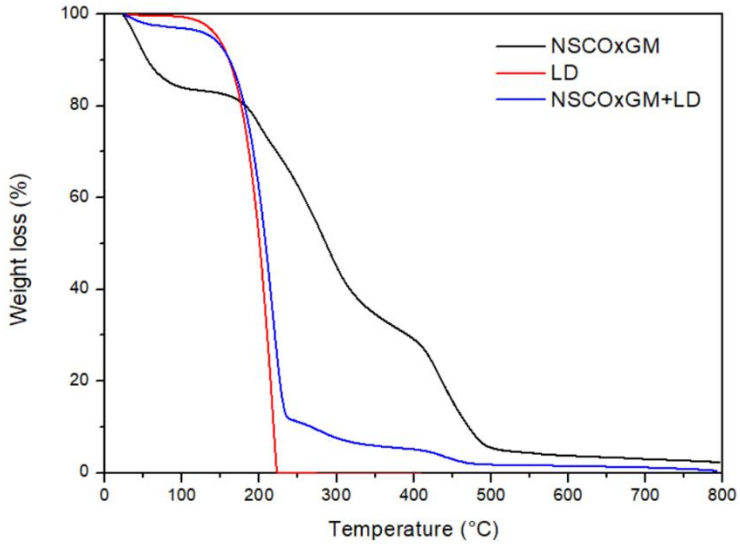

3.2 Morphology and Porosity

The large surface area and high porosity of hydrogels enable efficient drug loading. Moreover, porosity significantly influences diffusion, with larger pores tending

to accelerate the release kinetics of encapsulated substances (Thang; Chien; Cuong, 2023). Scanning electron microscopy (SEM) was employed to examine the surface morphology and porosity of NSC-OxGM and NSC-OxGM/LD hydrogels, as shown in Figure 32. The rapid sublimation of frozen water within the polymer matrix resulted in the formation of voids and pores, accurately reflecting the 3D porous structure of the hydrogels without altering their integrity. No significant differences in pore size or porosity were observed after the incorporation of LD, with both hydrogel formulations maintaining a highly interconnected porous structure. This phenomenon can be attributed to the weak interaction between NSC-OxGM and LD. LD was loaded by the existing interconnected porous spaces of the NSC-OxGM hydrogels network. Morphology of NSC-OxGM/LD hydrogels using SEM images reveals spheres relatively well dispersed and uniform distribution of LD in the NSC-OxGM hydrogels matrix. In Figure 32 c,d nanometric particles of LD can be seen on the hydrogel pore surface. This suggests effective incorporation and dispersion of lidocaine within the hydrogel network, potentially enhancing its drug delivery capabilities.

Figure 32 ─ SEM images of NSC-OxGM hydrogel magnitude 350x (a), 2000x (b); and NSC-OxGM/LD hydrogel magnitude 350x (c) and 2000x (d).

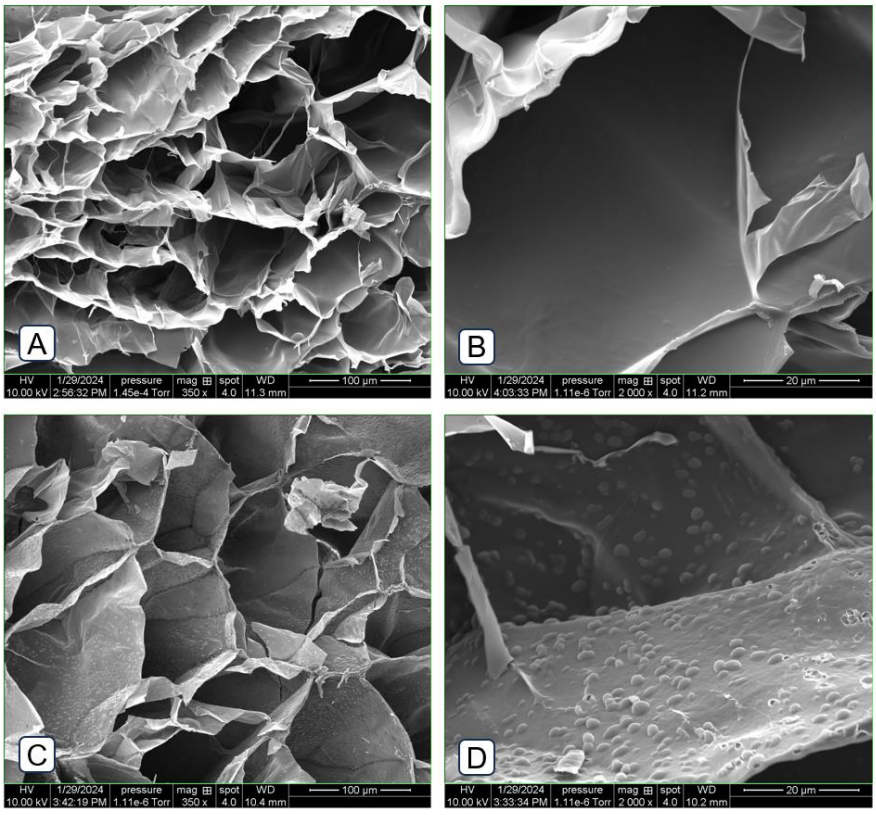

3.3 *In vitro* drug release

Understanding drug release mechanisms from hydrogel-based carriers is crucial for the development of more effective drug delivery systems. The *in vitro* drug release profile was conducted to evaluate the sustained release properties of the novel system under simulated physiological conditions.

Figure 33 illustrates the cumulative release profile of lidocaine from the NSC-OxGM hydrogel. The data shows that lidocaine was released from the hydrogel and characterized by a typical initial burst effect during the first 24 h, followed by a gradual percentage of LD delivered, likely due to the presence of free lidocaine not fully entrapped within the polymeric matrix. Over a period of 72 hours, 96% of the lidocaine was released, exhibiting a consistent and sustained release pattern that could contribute to prolonged analgesia without adverse effects (Zhou *et al.*, 2022). A similar lidocaine release profile from a polymeric hydrogel were reported by Li *et al.* (Facile design of lidocaine-loaded polymeric hydrogel to persuade effects of local anesthesia drug delivery system: complete in vitro and in vivo toxicity analysesLi *et al.*, 2021). However, their release equilibrium was reached after only 76.5% cumulative release within 36 h due to interaction between the lidocaine and the hydrogel matrix, leading to a fast and incomplete release of the drug. Therefore, in our work, it may infer that the prolonged release of LD by the NSC-OxGM hydrogels is due to the weak interaction between LD and NSC-OxGM.

Lidocaine is released from the hydrogel as water diffuses through the polymeric network, causing the hydrogel to swell and the drug to dissolve into the surrounding solution. To elucidate the release mechanisms of lidocaine from NSC-OxGM hydrogels, the release kinetics were modeled using the Korsmeyer-Peppas equation for cylinder (Figure 34). The model showed an excellent fit to the experimental data, with an R^2 value of 0.96. The release exponent ‘n’ was determined to be 0.59, indicating a non-Fickian transport mechanism, where both diffusion and degradation contribute to the drug release. This finding aligns with the work of Rasool *et al.* (Rasool *et al.*, 2020), who reported a non-Fickian release profile (n = 0.83) for lidocaine from carrageenan and alginate-based hydrogels. The release rate results indicate that the LDC-loaded NSC-OxGM hydrogels hold significant promise as a novel approach for extending the use of local anesthetics in clinical pain management.

Figure 33 ─ Sustained-release profile of lidocaine from NSC-OxGM hydrogels according to initial mass (%) in 37 °C PBS solution.

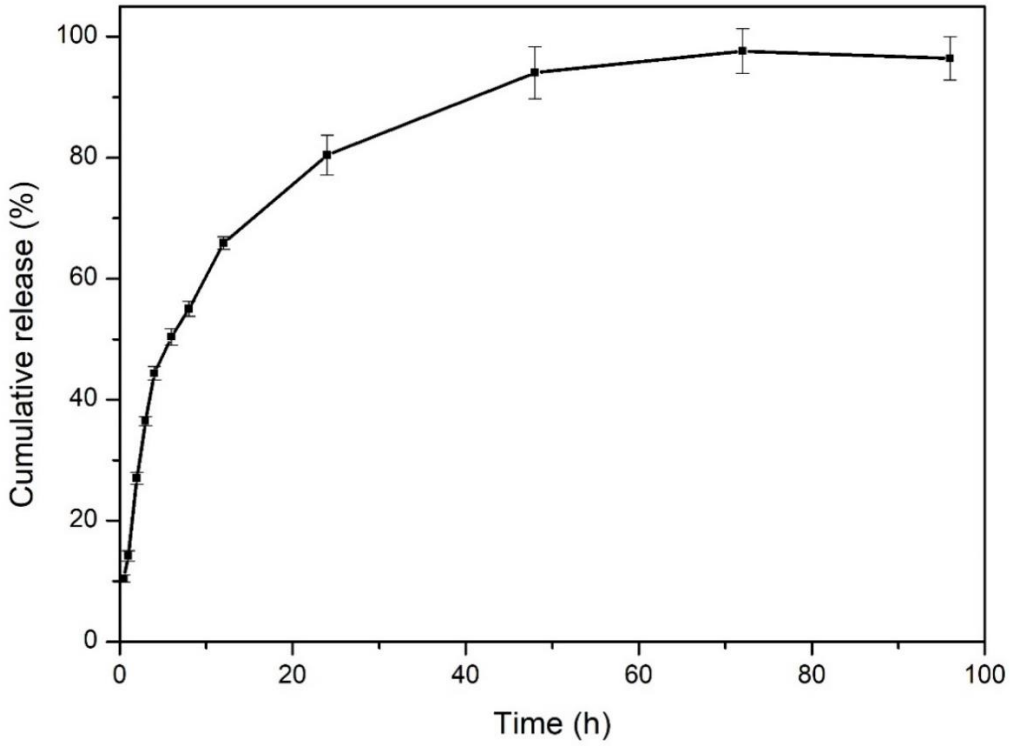

Figure 34 ─ Release profile data (dots) and Korsmeyer-Peppas model (red line). The model was obtained using OriginPro with the parameters shown in the table

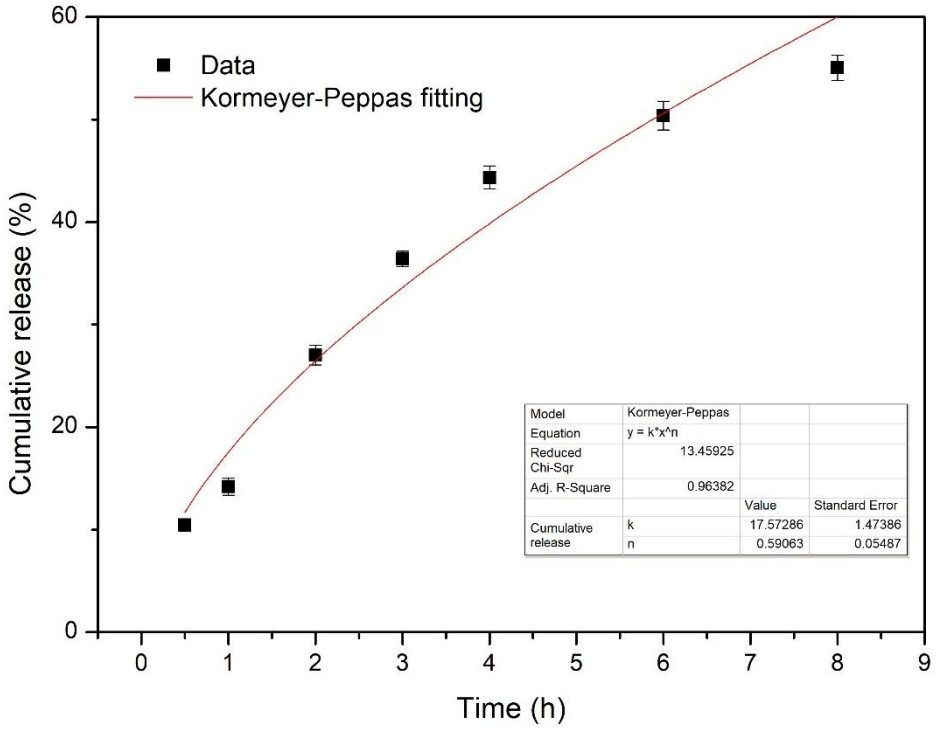

3.4 Cell viability

Due to the high concentration of lidocaine in the NSC/OxGM hydrogels (HG), there was a greater amount of free drug medication available to interact with membrane components, resulting in decreased cellular viability. The lidocaine loaded hydrogel (HGLid) showed high cytotoxicity, and it decreased drastically when compared to the hydrogel (Figure 35). Most studies show that the addition of lidocaine into the hydrogel increases its cell viability but using smaller concentration (20-100 µg/mL), while in this study it was used the commercial formulation of 2 % (Physicochemical and pharmacological investigations of polyvinylpyrrolidone - tetrahydroxyborate hydrogel containing the local anesthetic lidocaineLi *et al.*, 2021; Wu *et al.*, 2023).

Figure 35 ─ Indirect cell viability of L929 in contact with the extractive of the materials

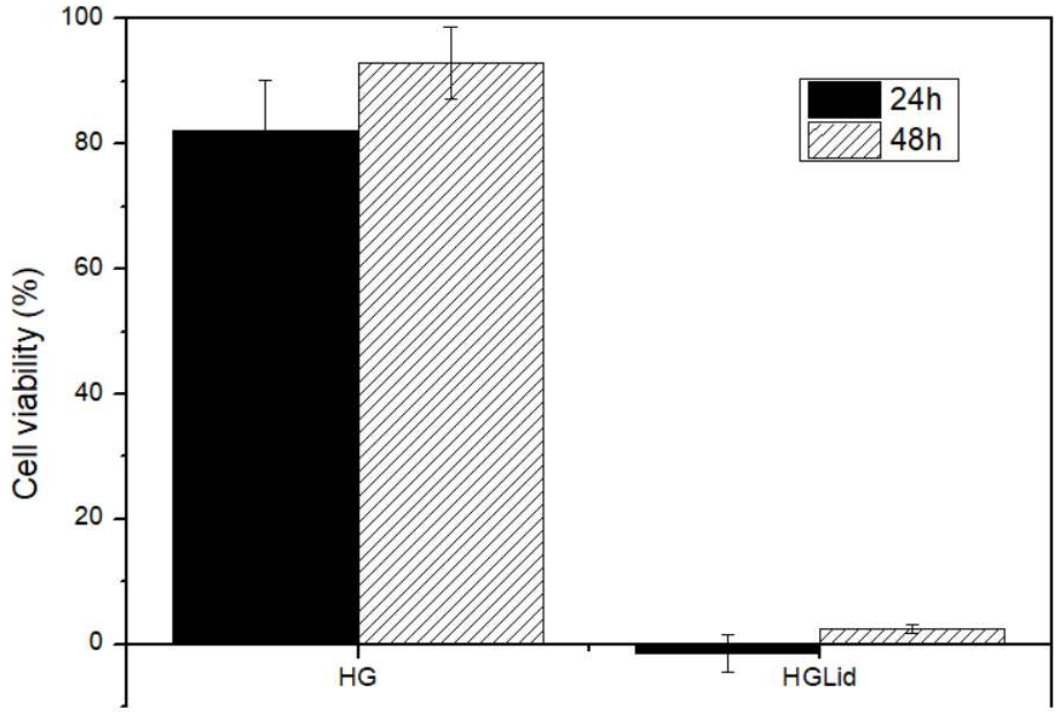

4 CONCLUSION

NSC-OxGM hydrogel was able to sustained delivery of lidocaine as the system was able to release the drug for 5 days. The model indicated that the hydrogel was degraded (erosion) and this contributed to the release of the bioactive molecules. The results obtained so far indicate that they are capable of sustained release lidocaine from the polymetric matrix for postoperative pain management. Unfortunately, the studied concentration was considered cytotoxic even though it is commercially used, a study with lower and progressive concentration may show better results.

CHAPTER 3: INJECTABLE HYDROGEL BASED ON CHITOSAN / GUAR GUM REINFORCED WITH BACTERIAL CELLULOSE NANOFIBER FOR TISSUE ENGINEERING

ABSTRACT

The increasing demand for devices suitable for regenerating or replacing damaged tissues highlights the need for advanced biomaterials. Hydrogels are promising candidates for regenerative medicine but often lack mechanical strength. To overcome this limitation, we developed a novel nanocomposite material using bacterial cellulose nanofibers (BCF) as reinforcement for hydrogels based on N-succinyl chitosan (NSC) and Oxidized guar gum (OxGG). These hydrogels were produced through a simple and safe Schiff base reaction and hydrogen bonding, without potentially toxic crosslinker or external stimuli. Comprehensive chemical characterization was performed using FTIR, XPS, and TGA. SEM images revealed significant changes in the hydrogel internal structure after BCF incorporation, resulting in a more compact and organized porous matrix, which also affected the swelling behavior of the hydrogel by reducing PBS uptake due to the rigid polymeric network. Both hydrogels exhibited fast gelation time (<30 s), ensuring excellent injectability for minimally invasive therapy. The incorporation of BCF into the NSC/OxGG hydrogel resulted in a 240% increase in both storage and compressive moduli compared to the initial formulation. Additionally, both hydrogels demonstrated excellent biocompatibility, with high viability of neonatal human dermal fibroblast (nHDF) cells. These results suggest that the multifunctional NSC/OxGG/BCF hydrogels have promising potential for tissue engineering applications.

Keywords: Biomaterials; polymers; polysaccharides; hydrogels; chitosan.

1 INTRODUCTION

Organ failure and tissue loss represent significant challenges in healthcare worldwide, mainly due to the limited availability of organ and tissues for donation or transplantation. Tissue engineering offers a promising strategy for clinical treatment by using there-dimensional (3D) biomaterials to emulate the extracellular matrix (ECM), thus providing a novel approach for regenerating lost tissues and damaged organs. Hydrogels are frequently investigated as biomaterials for tissue engineering matrices due to their diverse properties, including their ability to retain a significant amount of water within their hydrophilic polymeric backbone, which is essential for supporting enclosed cells. Additionally, hydrogels exhibit macroscopic physicochemical characteristics and rheological behavior comparable to native soft tissues, thereby enhancing the tissue regeneration process (Khan *et al.*, 2024).

Although hydrogels have been developed primarily to mimic native tissue properties, many can exhibit low mechanical durability. To address this challenge, researchers are continually exploring diverse compositions and crosslinking methods (GhavamiNejad *et al.*, 2020). Furthermore, hydrogels can be engineered to exhibit appropriate physicochemical behavior and structural similarity to various tissues through different processing techniques.

Natural polymer-based hydrogels are among the most promising biomaterials for tissue engineering applications due to their excellent biocompatibility, biodegradability, and similarity to ECM (Elkhoury *et al.*, 2021). Among natural polymers, chitosan is one of the most studied in the biomedical field, including applications such as wound dressing (Xue *et al.*, 2019), treatment against tumor cells (Choi *et al.*, 2019; Yu, Y. *et al.*, 2023), matrix for tissue engineering, drug release (Foley *et al.*, 2013), and 3D printing (Rajabi *et al.*, 2021). Despite its advantageous biological properties, chitosan limited solubility in acidic media has been a significant drawback (Muxika *et al.*, 2017; Shariatinia, 2019). *N*-succinyl chitosan (NSC) emerges as a promising acyl chitosan derivative with a simple preparation procedure, free from toxic reagents, and low production cost. NSC exhibits highly attractive characteristics including excellent water solubility, mucoadhesive properties, and notable bioavailability and biodegradability. Importantly, NSC retains the biocompatibility and non-toxicity inherent in chitosan (Bashir *et al.*, 2015).

Schiff base reactions have gained interest in synthesizing injectable hydrogels for biomedical applications (Maciel *et al.*, 2019; X. Junpeng, L. Yi, 2019). These reactions, forming imine bonds between carbonyl and primary amine groups, occur under mild conditions with water as the sole byproduct, offering a safer alternative to potentially toxic crosslinking agents, such as glutaraldehyde and carbodiimide (Khunmanee; Jeong; Park, 2017). For instance, Yu *et al.* (Yu, Z. J. *et al.*, 2023) developed injectable hydrogels with complex structures by 3D printing using Schiff base reaction between carboxymethyl chitosan (CMCS) and oxidized hyaluronic acid (OHA) for tissue engineering.

Oxidation reactions have been widely employed to functionalize polysaccharides as crosslinking agents, offering a simple method to introduce aldehyde groups into macromolecules through the selective oxidation of vicinal diols (Reakasame; Boccaccini, 2018). Guar gum (GG) is particularly suitable for oxidation using sodium periodate, allowing it to serve as a macro crosslinking agent by forming Schiff base bonds with amino-rich biopolymers such as chitosan.

However, the mechanical properties of naturally derived hydrogels often limit their use in tissue repair applications. To overcome these limitations, a novel class of materials known as nanocomposite hydrogels has recently emerged. These hydrogels combine traditional hydrogel with nanometer-sized fillers, typically leading to enhanced mechanical properties or the introduction of new functionalities (Xing; Tang, 2022). Unlike conventional hydrogels, which consist solely of soluble polymeric chains, nanocomposite hydrogels are formed from crosslinked 3D networks of nanofibers, such as cellulose nanofibers (CNFs). The interfiber hydrogen bonding within these nanoscale networks can significantly improve their mechanical properties, making them more suitable for tissue repair (Guan *et al.*, 2021).

Cellulose nanofibers (CNFs) have been incorporated as enhancers and hydrophilic interpenetrating polymers, which are created by integrating a secondary polymer within a crosslinked hydrogel (Cui; Zhang; Coseri, 2023). The unique properties of CNFs, including biocompatibility, high mechanical strength and suitable rheological characteristics, have made them suitable for tissue engineering applications. Unlike most common reinforcing particles, CNFs have a fibrous shape and abundant hydrogen bonding capacity, enabling them to form interconnected porous structure with chitosan hydrogels. This structure can distribute stress and

mitigate permanent damage under compressing.

Bacterial cellulose nanofibers (BCF) are formed of an ultrathin, three-dimensional network of randomly oriented and interlaced nanofibrils. These nanofibers are produced through the sporadic motion of the bacteria during the fermentation process. The bacteria diffuse into the culture medium and create a nanofibrillar network that permeates throughout it (Vasconcelos *et al.*, 2020). Compared to cellulose of plant origin, BCF offers unique advantages, such as high purity, superior mechanical strength, a crystalline structure, exceptional flexibility, and excellent biocompatibility, which are promising properties for biomedical applications (van Zyl; Coburn, 2019).

In this study, we present a novel system consisting of oxidized guar gum (OxGG) and *N*-succinyl chitosan (NSC) hydrogels reinforced with bacterial cellulose fibers (BCF) (Figure 36). Based on existing literature, we hypothesize that this system can provide a mechanically stiff and multifunctional material suitable for tissue engineering applications. This material is expected to offer enhanced mechanical properties and excellent biocompatibility. The chemical modification of chitosan addresses its limited solubility in water, while the oxidation process introduces aldehyde groups capable of crosslinking chitosan. This crosslinking via Schiff base reaction is rapid, safe and does not require external stimulation. Incorporating BCF overcomes the weak mechanical properties of NSC/OxGG hydrogels, forming a network through various intermolecular interactions.

Figure 36 ─ Schematic representation of a bacterial cellulose reinforced-hydrogel based on *N*-succinyl chitosan and dialdehyde galactomannan

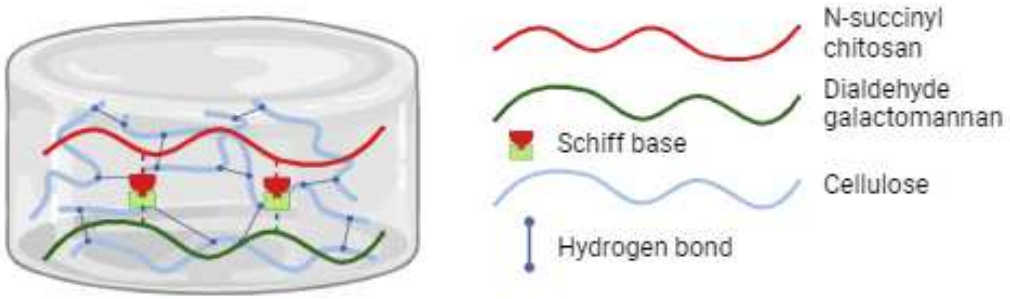

Source: Own elaboration

2 MATERIALS AND METHODS

All experiments were conducted at the Laboratory of Biomaterials and Bioengineering at Université Laval, Canada, as part of a sandwich program financially supported by CNPq, under the supervision of Prof. Diego Mantovani.

2.1 Materials

Low molecular chitosan from shrimp shells (77% degree of deacetylation, Mw = 84.2 kDa), and gum guar (galactomannan) were purchased from Sigma Aldrich, Brazil. Commercially available methanol, ethanol, acetone, ethylene glycol and glacial acetic acid were purchased from Synth, São Paulo, Brazil. Succinic anhydride (Sigma Aldrich, Brazil), sodium hydroxide (Vetec, Brazil), sodium periodate (Vetec, Brazil), potassium chloride (Sigma Aldrich, Brazil), potassium carbonate (Sigma Aldrich, Brazil), and hydroxylamine hydrochloride (Vetec, Brazil) were all acquired in analytic grade (>99% purity). Resazurin sodium salt was purchased from Sigma (USA). Neonatal Human Dermal Fibroblasts (nHDF, 106-05n) were obtained from Cell Applications, San Diego, CA, USA. Dulbecco's Modified Eagle Medium (DMEM, Gibco, Invitrogen Corporation, Burlington, ON, Canada), fetal bovine serum (FBS, Gibco), Penicillin/Streptomycin (P/S, Gibco), and Hepes were purchased from ThermoFisher.

2.2 Bacterial cellulose nanofiber fabrication

Komagataeibacter hansenii (ATCC 53582) was used in static fermentation process to produce bacterial cellulose (BC). The cultivation procedure followed established protocols with minor modifications (Vasconcelos *et al.*, 2020). Initially, the bacterial strain was propagated in a culture medium comprised of 20 g/L glucose, 5 g/L peptone, 5 g/L yeast extract, 1.15 g/L citric acid, and 2.7 g/L disodium phosphate, which were dissolved in water and agar. The pH of the medium was adjusted to 5 using 0.1 mol/L NaOH or HCl. After autoclave, the medium was inoculated with *K. hansenii* (3% v/v). BC membranes were synthesized in Schott bottles containing 100 mL of the culture medium. The fermentation process was performed statically in a refrigerated

incubator (B.O.D. TE 391, Tecnal, Brazil) at 30 °C for 10 days.

Afterward, membranes underwent purification to remove impurities, such as microorganisms and residual substances. Initially, the membranes were washed with distilled water to remove excess materials, followed by two warm baths in distilled water at 80 °C for 1 h each. To eliminate bacteria and medium, the BC was treated with 0.3 mol/L K_2CO_3 at 80 °C for 1 hour. Finally, the membranes were washed with distilled water until achieve pH 7.

Subsequently, the BC membranes underwent deconstruction to obtain a power that improve dispersion in the hydrogel. The membranes with water were processed in a blender to maximize fiber breakage. The resulting material was then frozen and freeze-dried, yielding a white powder (BCF). The overall process to obtain BCF are shown in Figure 37.

Figure 37 ─ Schematic representation of the BCF fabrication

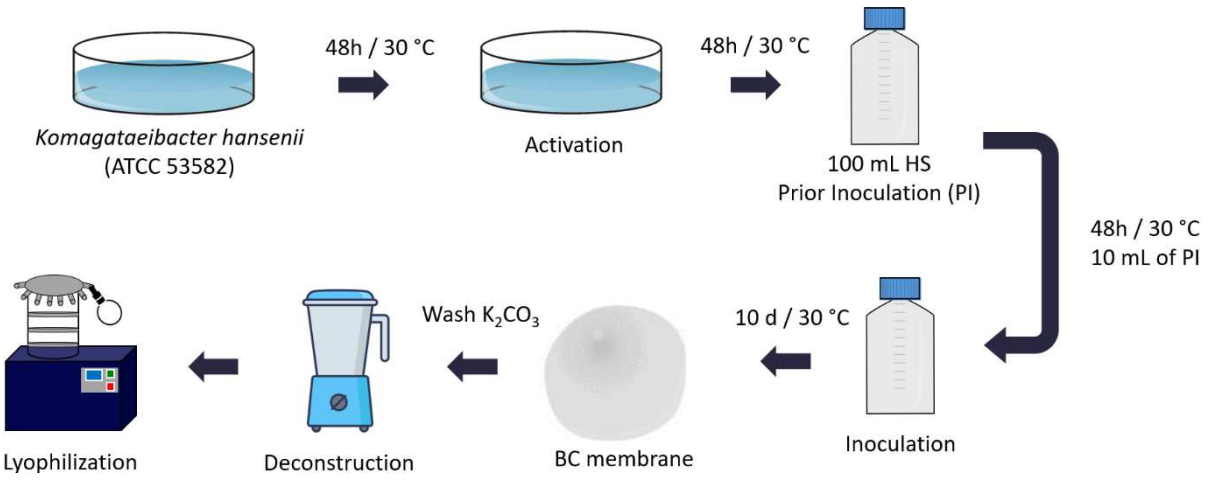

2.3 Nanocomposite hydrogel fabrication

Nanocomposite hydrogels were prepared by combining NSC, OxGG, and BCF. First, 3% (w/v) NSC and 2% (w/v) OxGG solutions were stirred individually using magnetic stirring for 24 h. To prepare the BCF suspension, BCF were dispersed in the NSC solution using an ultrasonic cell crusher to achieve a final hydrogel content of 1% (w/v) (Figure 38). The formulation was optimized to avoid any agglomeration of BCF in

excess amount. Parameters of the crushing process were optimized to achieve homogeneous solution (6 cycles of 60 s, 50% output).

Figure 38 ─ Illustrations of the BCF suspension in NSC solution before and after the ultrasonic crush process

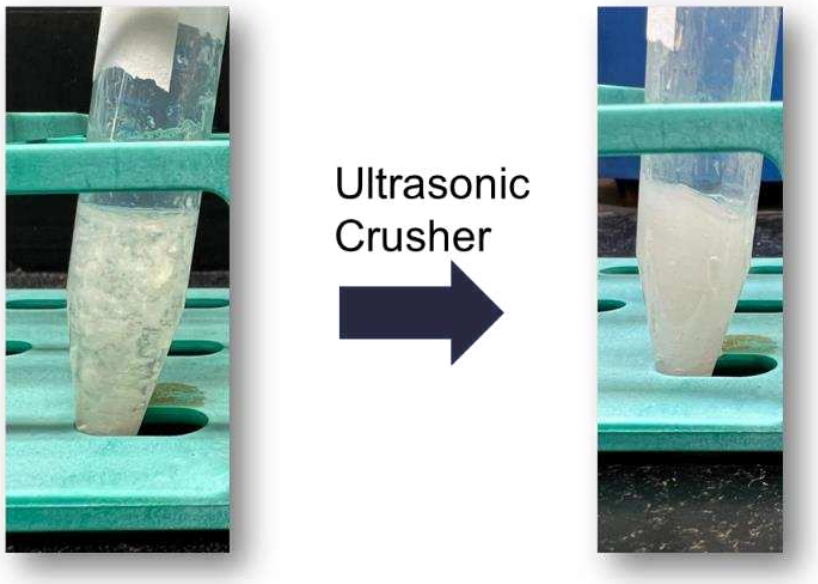

A 3:1 volume ratio of NSC/BCF to OxGG was used in the hydrogel fabrication to ensure full crosslinking. Samples were left to crosslink at room temperature for 24 h.

2.4 Fourier Transform Infrared (ATR-FTIR)

The hydrogel functional groups were investigated by Fourier-transform infrared-attenuated total reflectance (FTIR-ATR) spectroscopy using a commercial spectrometer (Agilent Cary 660 FTIR, Agilent Technologies, Santa Clara, CA, USA) equipped with a deuterated L-Alanine- doped triglycine sulphate (DLa-TGS) detector and a Ge-coated KBr beam splitter. Spectra were recorded in the absorbance mode, and 64 scans were recorded between 500 and 4000 cm^{-1} with a spectral resolution of 4 cm^{-1}. Three measurements were taken at different surface locations on each sample to confirm the homogeneity of the chemical composition.

2.5 X-ray Photon Spectrum (XPS)

XPS analyses were conducted using Physical Electronics PHI 5600-ci equipment (Chanhassen, MN, USA). A standard aluminum X-ray source (1486.6 eV) recorded the survey spectra with charge compensation. High-resolution C 1s XPS spectra were recorded using a standard magnesium X-ray source (1253.6 eV) without charge neutralization and then curve-fitted by referencing each spectrum to carbon at 285.0 eV. Detection was carried out at an angle of 45º concerning the surface normal, and the analyzed area was 0.5 mm^2. Three measurements for each sample were taken to confirm the homogeneity of the chemical composition.

2.6 Thermogravimetric analysis (TGA)

Thermal gravimetric analysis (TGA) was obtained using the Mettler-Toledo model (TGA/SDTA, USA) 851e. Approximately 2 mg of each sample was weighed into the crucible and scanned from 25 to 800°C at a heating rate of 10 °C/min under an inert nitrogen atmosphere. TGA curves were derived using OriginPro® 8.5 software to obtain the differential thermogravimetry (DTG) curves.

2.7 Scanning Electron Microscopy (SEM)

The morphology of the freeze-dried hydrogels was examined using scanning electron microscopy (SEM) with a Quanta-FEG FEI 450 instrument (Canada). Before imaging, the samples were sputter-coated with platinum/silver under an argon atmosphere using a Polaron SC500 Sputter Coater. The SEM images were obtained under a high vacuum by detecting secondary electron signals, with an acceleration voltage of 4 kV and a working distance of 10 mm.

2.8 Swelling capacity

To measure the swelling capacity, 2 mL of hydrogel was precisely weighed (mg) and then immersed in 30 mL of PBS at 37 °C. After, the surface PBS was carefully blotted using a paper tower, and the samples were reweighed at predetermined intervals (m_F). All experiments were performed in triplicate.

2.9 Rheological behavior

The rheological behavior of hydrogels was assessed using ElastoSens™ Bio (Rheolution Inc., Canada), which uses vibrations to obtain contactless viscoelastic measurements in a non-destructive manner. The sample holder, with dimensions of 23.1 mm in diameter and 19 mm in height, was firmly attached to a mechanical unit inside the instrument. A 3 mL of NSC solution, both with and without BCF, was added to the sample holder, followed by 1 mL of OxGG. The contents were gently mixed, and then the readings were initiated at 37°C. The mechanical unit applied a vertical pulse vibration at each measurement point to the bilayer structure. The sample height was measured using an ultrasonic probe located at the center top of the sample holder. By knowing the geometrical properties of the bilayered structure (measured height and known diameter) and the mechanical properties of the flexible membrane, the resonance properties of the bilayer structure were determined, which depended on the viscoelastic properties of the sample.

2.10 Stress-Relaxation Assay

The stress-relaxation unconfined compression tests were performed on the hydrogels using a MACH-1 Mechanical Tester System (Biomomentum Inc., Canada). Cylindrical test specimens (10 mm in diameter, and 6-7 mm in height) were carefully prepared to ensure uniformity (Yu *et al.*, 2021). The stress/relaxation test parameters were as follows: ramp amplitude was set to 10% of the initial sample thickness; ramp velocity was set to 5% of the initial sample thickness per second and three ramps. The tests were performed in a bath containing PBS solution (0.01M, pH 7.4) at room

temperature. The fixed relaxation time was 15000 seconds. Load and deformation, measured in Newtons and millimeters, respectively, were recorded at 10 ms intervals. For each sample (n=3), stress was calculated using Equation 9 and expressed in kPa:

$$\sigma = \frac{F}{A} \tag{9}$$

where F is the force measured (N) and A is the sample cross-section area (mm^2). For each sample, in addition, the elastic modulus was calculated according to the equation (Equation 10):

$$E = \frac{\sigma}{\varepsilon} = \frac{F}{A * \varepsilon} \tag{10}$$

where σ is the stress, ε is the strain (the deformation the samples underwent, nondimensional) and A is the cross-section area (mm^2). ε was calculated through the formula (Equation 11):

$$\varepsilon = \frac{l - l_0}{l_0} \tag{11}$$

where l is the sample height deformation recorded at each point, while l_0 is the initial height.

Stress/Time and Stress/Strain curves were obtained from the recorded data. The elastic modulus has been calculated as the slope of the linear segment of the stress/strain curve.

2.11 Indirect cell viability

For cell viability assay, neonatal Human Dermal Fibroblasts (nHDF, 106-05n Cell Applications, San Diego, CA, USA) were cultured in DMEN+, composed by Dulbecco's modified Eagle's medium (DMEM) supplemented with 10% foetal bovine serum (FBS) and 1% of 10 000 U/mL Penicillin-Streptomycin (P/S), at 37°C in a humidified atmosphere with 5 % CO_2. Cells were subcultured when they reach 80% confluency, according to supplier protocols. For this assay, nHDF at passage 7 were seeded at a cell density of 15 000 cells/cm^2 in a 96-well-plate and incubated in DMEM+.

Hydrogel extracts (n = 3/condition) were prepared according to the procedure recommended by International Organization for Standardization (ASTM 10993-12) (Biological Evaluation of Medical Devices—Part 5: Tests for In Vitro Cytotoxicity, 2009). Briefly, 500 µL of hydrogel were immersed in 1mL DMEM supplemented with 1% P/S and incubated under standard culture conditions for 1, 3, and 7 days. At each incubation period, the extracts obtained were collected for the assay. After, 100 µL of each hydrogel extract supplemented with 10 % FBS were added to the cells (n = 3/condition) and incubated for 24 h. As a positive control, DMEM+ was used for cell treatment.

Subsequently, hydrogel extracts and DMEM+ (control +) were removed and 0.01 $mg.mL^{-1}$ resazurin sodium salt in DMEM+ was added to the cells, followed by 4 h at 37 °C, protected from light. After incubation, three aliquots of 100 µL for each sample were transferred into a 96-well plate for reading. The reduction of resazurin into resorufin in the presence of metabolically active cells was detected by fluorescence reading (λ_{ex} = 560 nm, λ_{em} = 590 nm) using a SpectraMax i3X spectrophotometer (Molecular Devices, USA). The cell viability percentages were calculated from normalized values, based on the negative control fluorescence.

2.12 Statistical analysis

All experiments were performed at least in triplicate and data was presented as mean ± standard deviation (SD). Statistical analysis was performed using one-way analysis of variance (ANOVA) using software Prism® and Origin®. Differences between groups were considered significant at $p < 0.05$.

3 RESULTS AND DISCUSSION

3.1 Fourier Transform Infrared (ATR-FTIR)

Figure 39 — FTIR spectrum of NSC, OxGG, BCF, NSC/OxGG, and NSC/OxGG/BCF

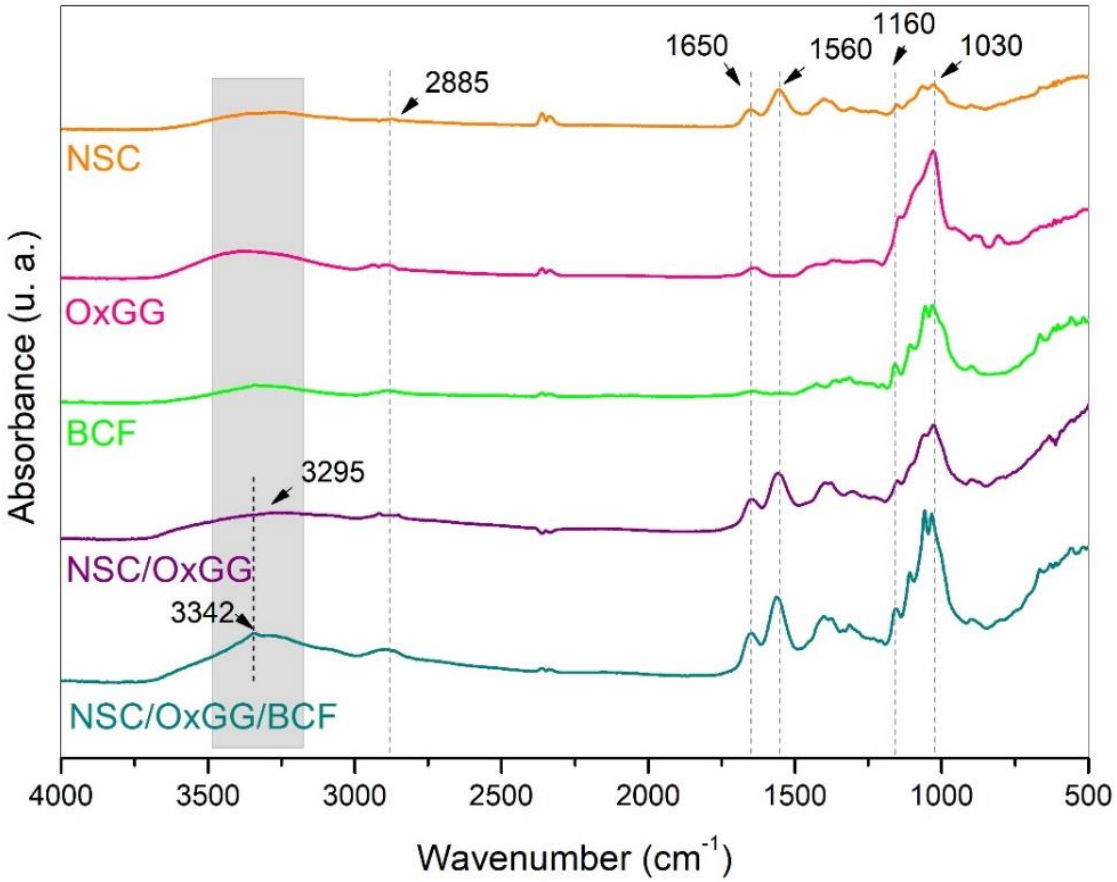

The FTIR spectra for precursor materials (NSC, OxGG, BCF), and freeze-dried hydrogels (NSC/OxGG, and NSC/OxGG/BCF) are shown in Figure 39. The band observed between 3490 and 3170 cm^{-1} corresponds to the stretching of O-H bonds. Characteristic bands associated with the pyranose ring were observed between 1160 and 1030 cm^{-1}, and were attributed to the stretching of C-O, C-O-C and C-C bonds (Oliveira *et al.*, 2023). The amide bands for NSC were shown at 1650 and 1560 cm^{-1}. The stretching of the C═N imine bond (Schiff base) in NSCOxGG hydrogels typically generates an absorption in the range of 1650 to 1690 cm^{-1}, but this was not possible to distinguish due to the overlap with the amide band (1650 cm^{-1}) of NSC (Carlos *et*

al., 2021). The BCFs presented peaks at 2885 cm^{-1} (C–H stretching), and at 1650 cm^{-1} (O–H bending vibrations due to absorbed water with some contributions from carboxylate groups) (Abouzeid *et al.*, 2018). The intensity of the O-H band increased with the addition of BCF to the hydrogel, and shifted from 3295 cm^{-1} in NSC/OxGG to 3342 cm^{-1}, suggesting the formation of hydrogen bonds in NSC/OxGG/BCF and weak interactions between BCF and the NSC/OxGG hydrogel (Wang *et al.*, 2020).

3.2 X-ray Photon Spectrum (XPS)

The surface composition of the biopolymers and their blends was characterized by X-ray photoelectron spectroscopy (XPS) survey analyses, and the results are presented in Table 9. The analyses revealed the presence of carbon (C), nitrogen (N), oxygen (O), and sodium (Na) elements in the hydrogels. The presence of sodium in the atomic composition of NSC and its hydrogels is attributed to the electrostatic equilibrium dynamics during the synthesis reaction, where the pH was adjusted to 12, promoting the formation of negatively charged COO- groups.

The high-resolution C 1s spectra for NCS show peaks at 288.3 eV, attributed to N-succinyl groups (O=C-NHx) and acetal moieties (C-O-C), along with the lower-energy peaks at 286.4 eV and 285.0 eV corresponding to C-N/C-O and C-C/C-H bonds, respectively, aligned well with the typical characteristics of functionalized carbons. Similarly, in the C 1s spectra for OxGG, the peaks at 285.0 eV, 286.7 eV, and 288.7 eV indicate the presence of C-C/C-H, C-O, and C=O/O-C-O groups (aldehyde and acetal functionalities), reflecting the compound's structural complexity. For the NSC/OxGG spectra, the C 1s peak was deconvoluted into three distinct peaks: 285.0 eV (C-C/C-H), 286.5 eV (C-N/C-O), and 288.2 eV (O-C-O/O=C-NHx) (Zhou *et al.*, 2014). Upon the addition of BCF, the hydrogel exhibited an increase in binding energy at 288.2 eV for the O-C-O species, compared to 288.0 eV in the NSC/OxGG spectrum. This shift suggested a change in the chemical and bonding environment of the oxygen-containing functional groups in the hydrogel after treatment with BCF.

Table 9 – Atomic composition of biopolymers NSC, OxGG, BCF, and hydrogels NSCOxGG, and NSCOxGGBCF obtained through XPS

	Atomic composition			
Sample	% C	% O	% N	% Na
NSC	59.6 (± 1.3)	30.4 (± 1.3)	4.6 (± 0.8)	5.5 (± 0.8)
OxGG	65.3 (± 0.7)	34.4 (± 0.6)	-	-
BCF	63.6 (± 0.6)	34.7 (± 0.4)	1.7 (± 0.2)	-
NSCOxGG	61.0 (± 0.9)	31.4 (± 0.9)	4.4 (± 0.3)	3.7 (± 0.4)
NSCOxGGBCF	67.9 (± 0.4)	19.2 (± 1.8)	4.4 (± 0.6)	2.2 (± 0.8)

Figure 40 – C 1s spectra of NSC, OxGG, BCF, NSCOxGG, and NSCOxGGBCF

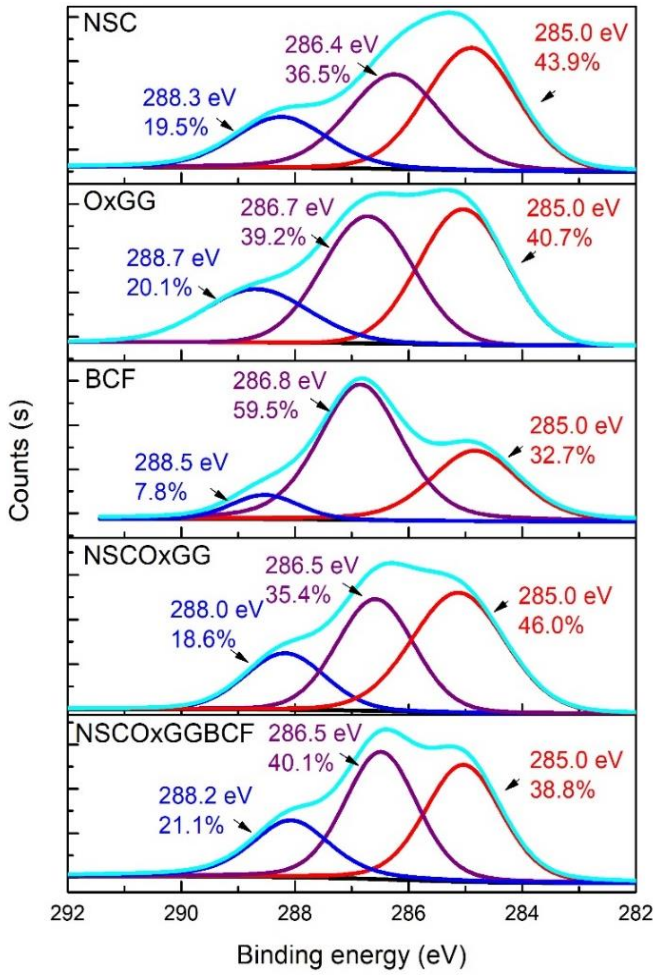

3.3 Thermogravimetric analysis (TGA)

The TGA test was performed to determine the thermal behavior of the obtained hydrogels. As shown in Figure 41, the thermograms of NSC/OxGG and NSC/OxGG/BCF hydrogels revealed approximately 9.5% and 7.6% material loss at 40–150 °C, respectively, due to the evaporation of the adsorbed water. The weight loss from 200 to 400 °C is related to thermal degradation of polymer backbone. The addition of BCF increased the degradation temperature peak from 276 °C to 305 °C. This result indicates that the introduction of BCF enhanced the structural stability of the hydrogel, likely due to the formation of a double-network structure between BCF and NSC/OxGG (Wang *et al.*, 2020). Moreover, breaking the O-H groups in the NSC/OxGG/BCF hydrogen bonds contributed to a second degradation step at 203 °C (Karzar Jeddi; Mahkam, 2019). Degradation beyond 400 °C corresponds to further and complete decomposition of the biopolymers. The final residual mass at 800 °C was lower for the BCF-reinforced hydrogel (8.5%) than NSC/OxGG (23.8%) (Table 10).

Figure 41 – TGA of the biopolymers NSC, OxGG, BCF,NSCOxGG, and NSCOxGGBCF

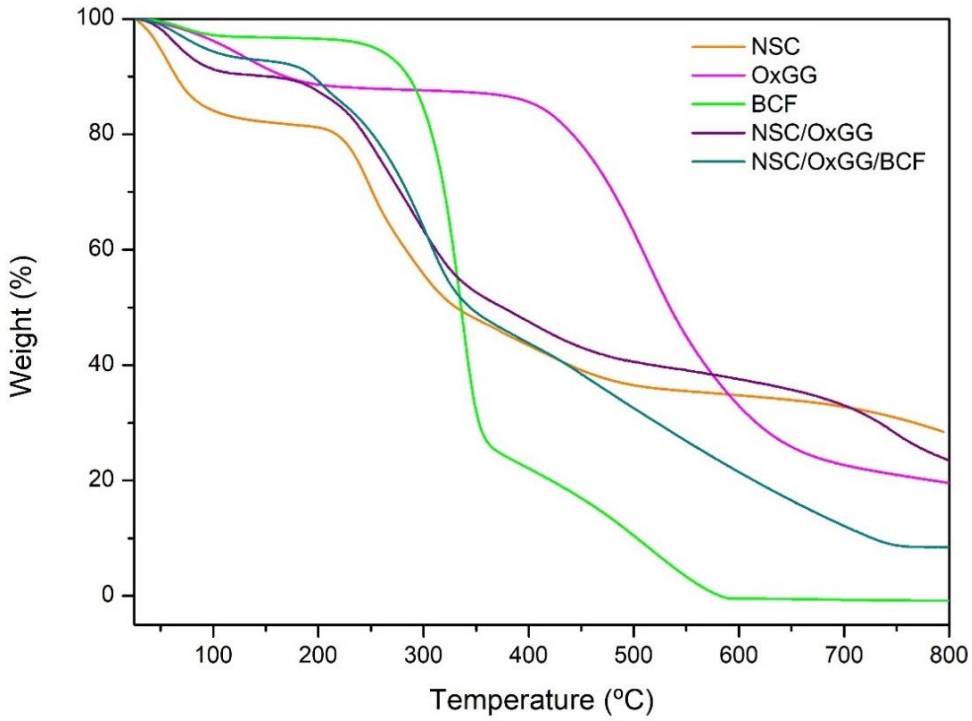

Figure 42 – TGA and DGA of freeze-dried NSC/OxGG, and NSC/OxGG/BCF hydrogels

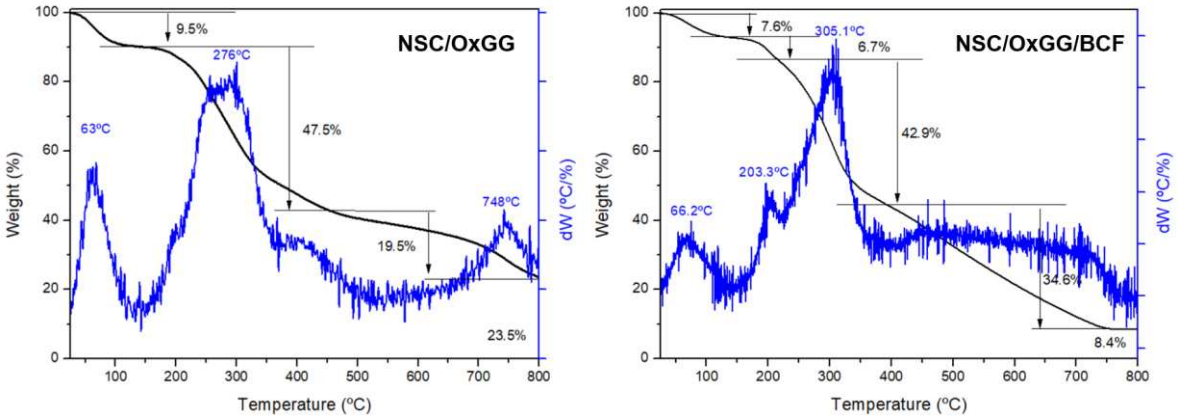

Table 10 ─ Thermal events of NSC, OxGM, BCF, NSCOxGG, and NSCOxGGBCF according to temperature range (ºC) and mass degradation (%)

Sample	1st event		2nd event		3rd event	
	Range (ºC)	Mass (%)	Range (ºC)	Mass (%)	Range (ºC)	Mass (%)
NSC	25–200	19.9	200-500	45.2	500-800	8.1
OxGM	25-200	11.7	200-400	4.3	400-800	66.2
BCF	25-150	2.4	150-360	71.6	360-600	26.5
NSCOxGG	25-150	9.5	150-400	47.5	400-800	19.5
NSCOxGGBCF	25-150	7.6	150-400	50.6	400-800	34.6

3.4 Scanning Electron Microscopy (SEM)

The morphologies of the hydrogels, with and without BCF, were analyzed using SEM. As shown in Figure 43, the hydrogels exhibited a porous structure, which is important for cell adhesion, proliferation, and migration (Gupta *et al.*, 2019). Notably, upon the incorporation of BCF, the pore sizes decreased, and more compact and

organized network structure formed. This suggests that BCF may integrate into the covalent cross-linking network, enhancing the compactness and structural coherence of the hydrogel, which could potentially influence its mechanical properties. In previous work by our group, we characterized the morphology of the bacterial cellulose nanofibrils (Vasconcelos *et al.*, 2020), identifying diameters ranging from 53 to 160 nm, with an average diameter of 80.9 ± 9.6 nm. Due to their extremely small size compared to the hydrogel pores, these nanofibers were not discernible in the microscopic analysis.

Figure 43 ─ SEM imagens of NSC/OxGG and NSC/OxGG/BCF

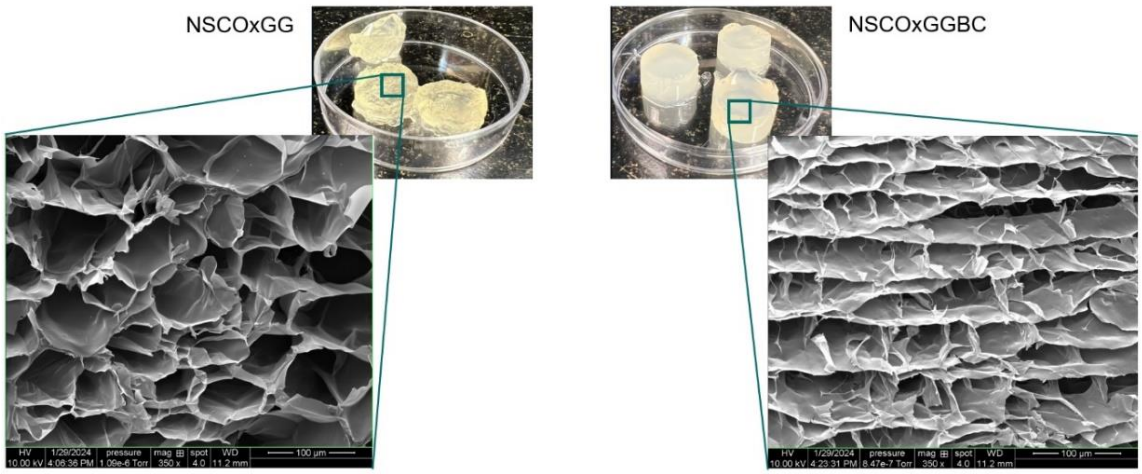

The average pore size of the hydrogels was determined from SEM images using ImageJ software, obtaining values of 72 ± 13 µm for NSC/OxGG and 41 ± 10 µm for NSC/OxGG/BCF. Incorporating cellulose into chitosan hydrogels has been reported to reduce their pore size, with an increase in cellulose content resulting in a further decrease in pore size (Wang *et al.*, 2021). In the context of bone tissue engineering, the optimal pore size for osteoblast is still controversial. However, studies have indicated that osteoblasts tend to proliferate more in smaller pores (around 40 µm) than larger ones (100 µm), although larger pores can enhance cell migration. In addition, for effective blood vessel regeneration, a minimum pore size of approximately 30 to 40 µm is essential to facilitate the exchange of metabolic components and enable endothelial cell infiltration (Loh; Choong, 2013). Therefore, NSC/OxGG/BCF hydrogels are suitable for those applications.

3.5 Swelling capacity

The swelling behavior is a crucial parameter for evaluating hydrogels, as this property allows hydrogel-based biomaterials to seed cells (Favi *et al.*, 2016). As shown in Figure 44, the swelling profiles of NSC/OxGG and NSC/OxGG/BCF hydrogels indicated that both samples reached equilibrium within 48 hours, effectively retaining fluid within their structures. The swelling capacity of NSC/OxGG hydrogel was higher than that of NSC/OxGG/BCF hydrogel. This difference might be attributed to the added BCF, which provided a tighter, denser network and decreased porosity, as observed in SEM images. The numerous large and interconnected pores in the NSC/OxGG hydrogels faciliated a rapid swelling rate and retaining water. However, in the NSC/OxGG/BCF system, the presence of BCF restricted polymer relaxation and hindered the swelling process. Additionally, BCF contain crystalline regions that limit water absorption (Cui; Zhang; Coseri, 2023).

Figure 44 ─ Swelling capacity of NSC/OxGG and NSC/OxGG/BCF hydrogels in PBS at 37 ºC. The data are presented as mean ± standard deviation (n = 3).

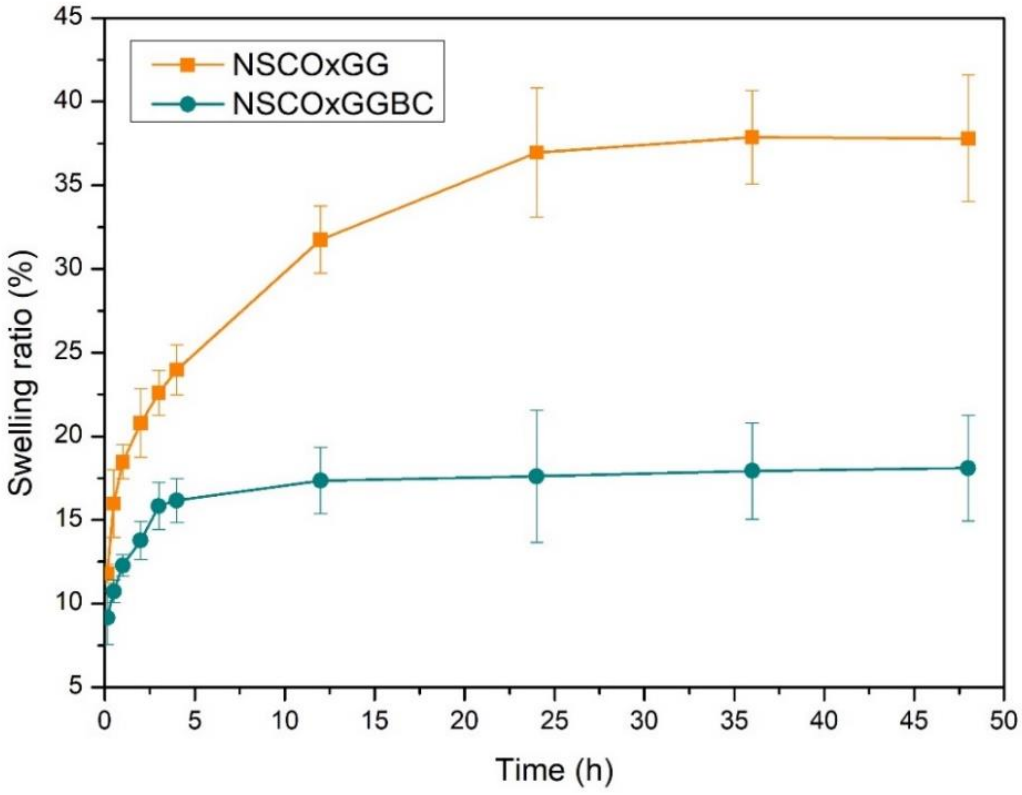

Swelling is a key characteristic of hydrogels, but excessive swelling can significantly compromise their mechanical performance. In tissue engineering, excessive swelling in body fluids weakens the hydrogel and may also compress or damage surrounding organs or tissues due to volume expansion. This phenomenon can also cause the hydrogel to detach from the targeted site when applied *in vivo* (Zhan *et al.*, 2021). Therefore, NSC/OxGG/BCF hydrogels offer an advantage over NSC/OxGG by providing enhanced stability during swelling, mitigating these issues.

3.6 Rheological behavior

A relatively new method for measuring the viscoelastic properties of hydrogels and soft materials involves a contactless and non-destructive approach. Laser technology detects system deformation and converts the measurements into storage (G') and loss (G'') moduli (Ceccaldi *et al.*, 2017).

Figure 45 illustrates the evolution of the shear storage modulus (G') and loss modulus (G'') of the formulated hydrogels over the initial 300 seconds. The results indicated a significant increase in the storage modulus, demonstrating a rapid transition from a viscous liquid to a soft viscoelastic solid. Initially, the gelation kinetics for both formulations were similar and fast (< 30 s), with the crossover point of G' and G'' - indicating gelation time - not observed in the measurement. Fast gelation time is particularly advantageous in biomedical contexts because it reduces the risk of hydrogel dispersion within the body before gel formation when injected *in* situ, and of compromising shape fidelity and the collapse of 3D-printed layers, ensuring the structural integrity and functional performance of the hydrogel in tissue engineering applications (Li; Yang; Lee, 2021; Rajabi *et al.*, 2021). Liu *et al.* (2020) (Liu, Q. *et al.*, 2020) similarly reported a rapid gelation time (< 30 s) for chitosan-based hydrogels, their viscoelastic curves did not exhibit the crossover point (G' = G''), with G' values remaining greater than G'' values throughout the experiment.

The addition of BCF did not significantly affect the gelation kinetics of the hydrogels. However, it positively influenced the viscoelastic properties. Both G' and G'' increased with the addition of BCF, indicating that the viscoelastic properties were significantly influenced by the presence of BCF in the NSC/OxGG hydrogels. BCF

acted as a multifunctional crosslinker, and the resulting physical entanglement and crosslinking within the hydrogel system contributed to the improved G' and G''.

Figure 45 ─ Shear storage (G') and loss (G'') modulus as a function of time for NSC/OxGM (orange) and NSC/OxGM/BCF (cyano).

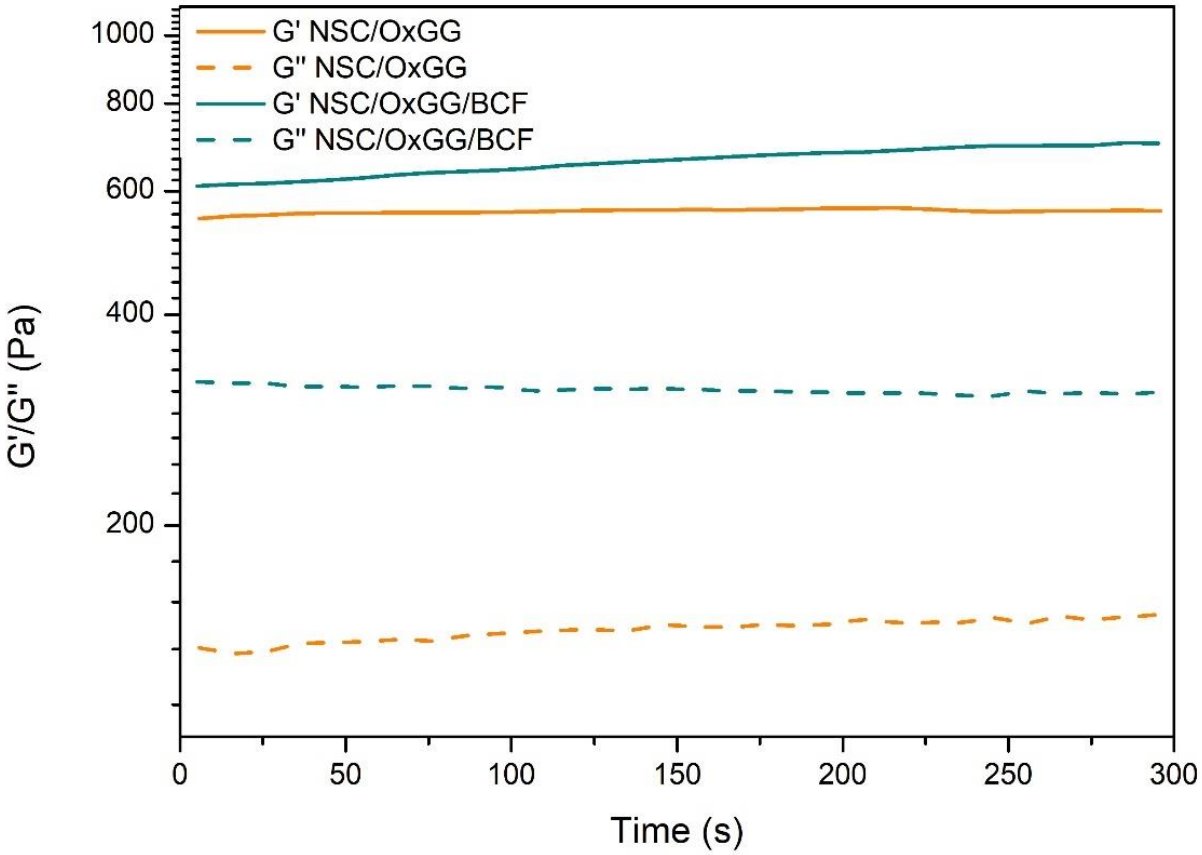

With the capability of the equipment to perform multiple measurements over different periods, a longer G' measurement was conducted to observe the behavior of G' values over an extended period. As shown in Figure 46 the maximum G' value was reached after 4 days, suggesting that the crosslinking reaction is still ongoing within the hydrogel network. The G' value for NSC/OxGG/BCF was 3.97 ± 0.59 kPa, compared to 1.65 ± 0.12 kPa for NSC/OxGG, representing an increase of 240%. Additionally, there is minimal relative change over time for NSC/OxGG/BCF, indicating that the addition of BCF did not significantly alter the crosslinking dynamics. Similar results were observed in the study by Deng *et al.* (2021) (Deng *et al.*, 2021), where the addition of cellulose nanofibrils increased the G' and G'' values of alginate/chitosan

hydrogels. Interestingly, a high cellulose content (2 wt. %) drastically decreased these values, likely due to the agglomeration caused by an excess amount of nanofibrils.

Figure 46 ─ Storage modulus (G') NSCOxGG and NSCOxGGBCF hydrogels over time.

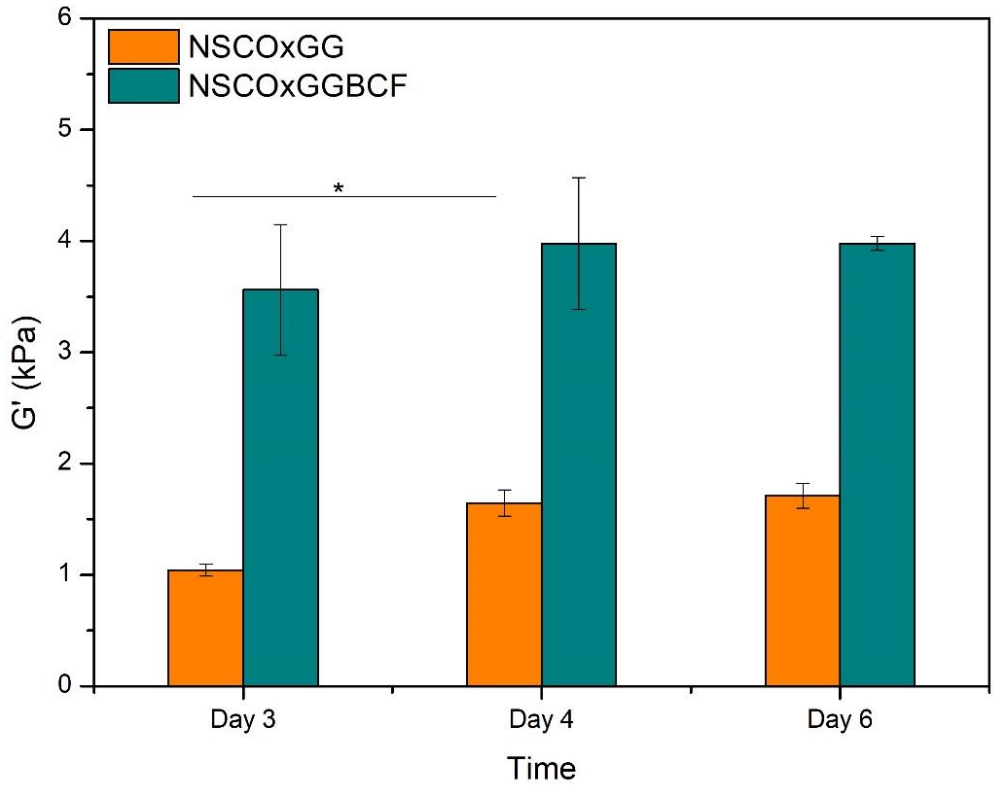

3.7 Stress-relaxation assay

Mechanical properties are an important parameter for hydrogels used in tissue engineering. Compression testing offers several advantages, such as its ability to assess soft materials under physiologically relevant loads in a hydrated environment. Since many load-bearing tissues in the body are subjected to compressive forces, this method provides a more accurate measurement of their mechanical properties. Compression testing allows for straightforward determination of properties directly from stress-strain curves. However, the technique has some drawbacks, particularly in sample preparation. Samples must be cut to precise specifications, and their surfaces must be free of any irregularities (Navindaran; Kang;

Moon, 2023).

Hydrogels with suitable stiffness not only provide a static environment for tissue regeneration but also influence cellular response at the implantation site (Ding *et al.*, 2021). Stress-relaxation tests were conducted on the formulated hydrogels with and without bacterial cellulose fibers (BCF) to evaluate the mechanical behavior. The compression modulus of the hydrogels was calculated from the initial stress-strain curves, focusing on the linear curve corresponding to up 5% strain (Figure 47A). The results, presented in Figure 47B, demonstrated that the incorporation of BCF significantly affected the compression properties, leading to an overall enhancement of the hydrogel's mechanical properties. The Young's modulus increased from 92.7 ± 7.1 kPa to 197.1 ± 35.7 kPa after adding BCF, an approximately 240% increase.

This improvement can be attributed to the continuous and interconnected structure formed by the winding and overlapping BCF, which shares chemical similarity with the chitosan in the hydrogel matrix. Moreover, the interconnected, compacted, and organized pores help to evenly distribute loads and provide ductility to the hydrogel (Wang *et al.*, 2021). Cui *et al.* (2023) (Cui; Zhang; Coseri, 2023) also reported that incorporating 1% (w/v) cellulose fibers into a Schiff base crosslinked hydrogel composed of gelatin and oxidized alginate improved its mechanical properties, but increasing the compressive modulus from 164.2 ± 10.6 kPa to 184.9 ± 6.4 kPa, which represents a modest improvement of 12%.

Figure 47 — (A) Initial stress-strain curves and (B) Young's Modulus values of NSC/OxGG and NSC/OxGG/BCF hydrogels

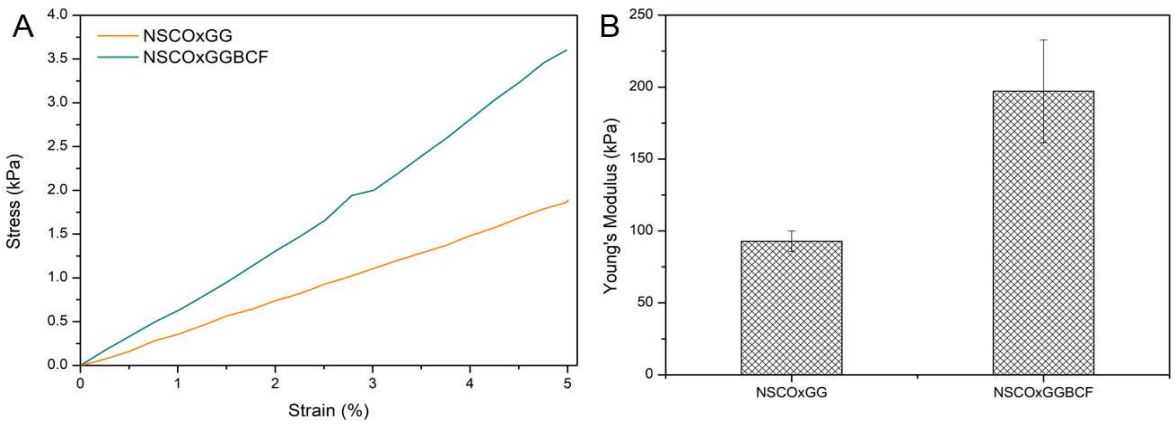

The stress/relaxation test is an interesting characterization method for understanding the viscoelastic behavior of hydrogels and soft biological tissues. In such tests, the sample is subjected to a sudden deformation up to a predefined strain, and the subsequent decay in stress is recorded as a function of time. Beyond the elastic and viscous moduli, a detailed analysis of stress/relaxation results can offer insights into the structural reorganization of hydrogels under mechanical stress. Conducting multiple stress relaxation tests allows the evaluation of the hydrogel in a large range of strains (Meghezi; Drouin; Mantovani, 2017).

Figure 48 ─ (A) Stress/Strain and (B) Stress/Time curves of the NSC/OxGG and NSC/OxGG/BCF hydrogels

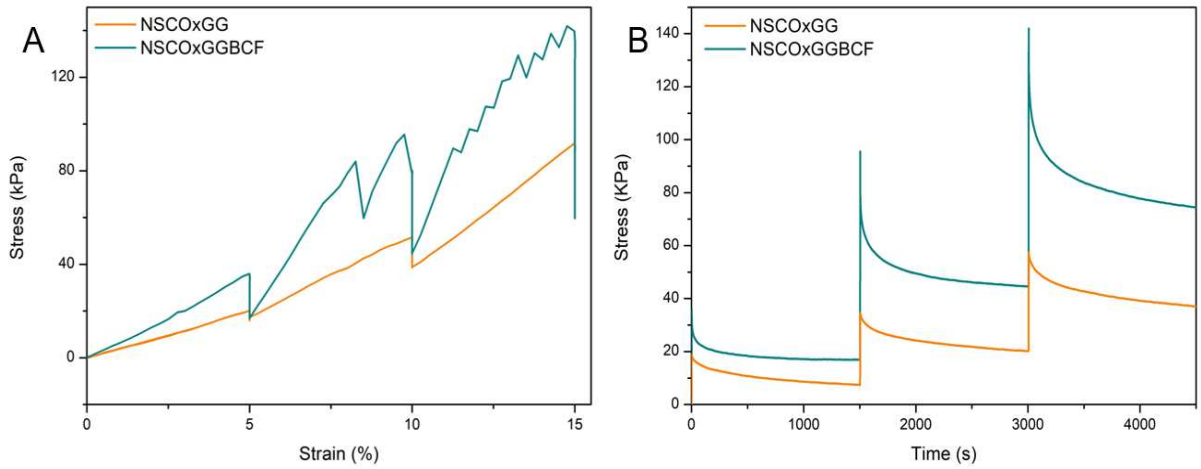

Figure 48 shows the stress/strain curves (A) and stress/time (B) for both studied hydrogels, revealing noteworthy observations: 1) the increase in stress followed by relaxation periods altered the compressive modulus, as indicated by the slope of the curve. This suggests that the polymeric matrix underwent realignment and reorganization in response to external stimuli, enhancing its mechanical properties. 2) The NSC/OxGG/BCF hydrogel experienced abrupt decreases in stress, or "cracking," likely due to the breaking of hydrogen bonds between molecular chains. BCF has crystalline regions that might act as weak points, leading to mechanical failure under high stress (Wang *et al.*, 2021). 3) The stress/time curves showed that the NSC/OxGG hydrogel gradually regained its original shape, exerting a weak and slow force against the equipment during relaxation periods, indicating a more elastic behavior. In contrast,

NSC/OxGG/BCF exhibited a stronger response with higher force applied against the equipment, suggesting a more robust and less elastic behavior.

3.8 Cell viability

Regenerative medicine products, especially those intended for biological interfaces in contact with living tissues or body fluids, require thorough biocompatibility assessment, including an evaluation of their degradation product (Hama *et al.*, 2023). For the biological characterization of the designed hydrogels, primary human cells were cultured with extracts from the NSC/OxGG and NSC/OxGG/BCF formulations. Figure 49 shows the cell viability results using extracts from hydrogel cultures after 1, 3, and 7 days.

Both hydrogels exhibited high cell viability at all time points, and according to ISO 10993-5, they were considered to be non-cytotoxic materials (cell viability > 70%). These results demonstrated the excellent biocompatibility of the hydrogels, making them suitable for long-term biological applications. This could be attributed to the successful fabrication of a bioadaptive, extracellular matrix (ECM)-mimetic environment that supports cellular health and function. In fact, chitosan is widely used as biomaterial due to their high biocompatibility, non-toxic properties, and molecular structure that resembles glycosaminoglycans, the main polysaccharide components of the ECM (Ahsan *et al.*, 2018). Furthermore, both hydrogels were fabricated without the use of any extraneous toxic cross-linking agents, ensuring a safer and more biocompatible product.

For day 1, NSC/OxGG exhibited lower cell viability than NSC/OxGG/BCF. This could be attributed to the rapid release of degradable products from its polymetric matrix, which is associated with its greater porosity and swelling capacity. In contrast, for day 7, NSC/OxGG/BCF showed lower cell viability, possibly due to further hydrogen bonding cleavage within its hydrogel network, increasing the concentration of degradable products. No statistical difference was observed for day 3. However, the addition of bacterial cellulose fibers (BCF) did not compromise the biocompatibility of the NSC/OxGG hydrogels. Incorporating BCF into the NSC/OxGG hydrogel may enhance the structural framework, providing superior anchorage sites for cells within

the matrix network. This structural enhancement can improve cell viability, adhesion, and growth. As demonstrated by Maharjan *et al.* (2021) (Maharjan *et al.*, 2021), which reported that the addition of cellulose nanofibers into chitosan hydrogels significantly improved the viability, adhesion, and proliferation of MC3T3-E1 pre-osteoblast cells.

Figure 49 ─ Cell viability of nHDF cultured with different time extracts from NSC/OxGG and NSC/OxGG/BCF hydrogels. Data are presented as mean ± standard deviation. Statistical significance is indicated as *p < 0.05; **p < 0.01.

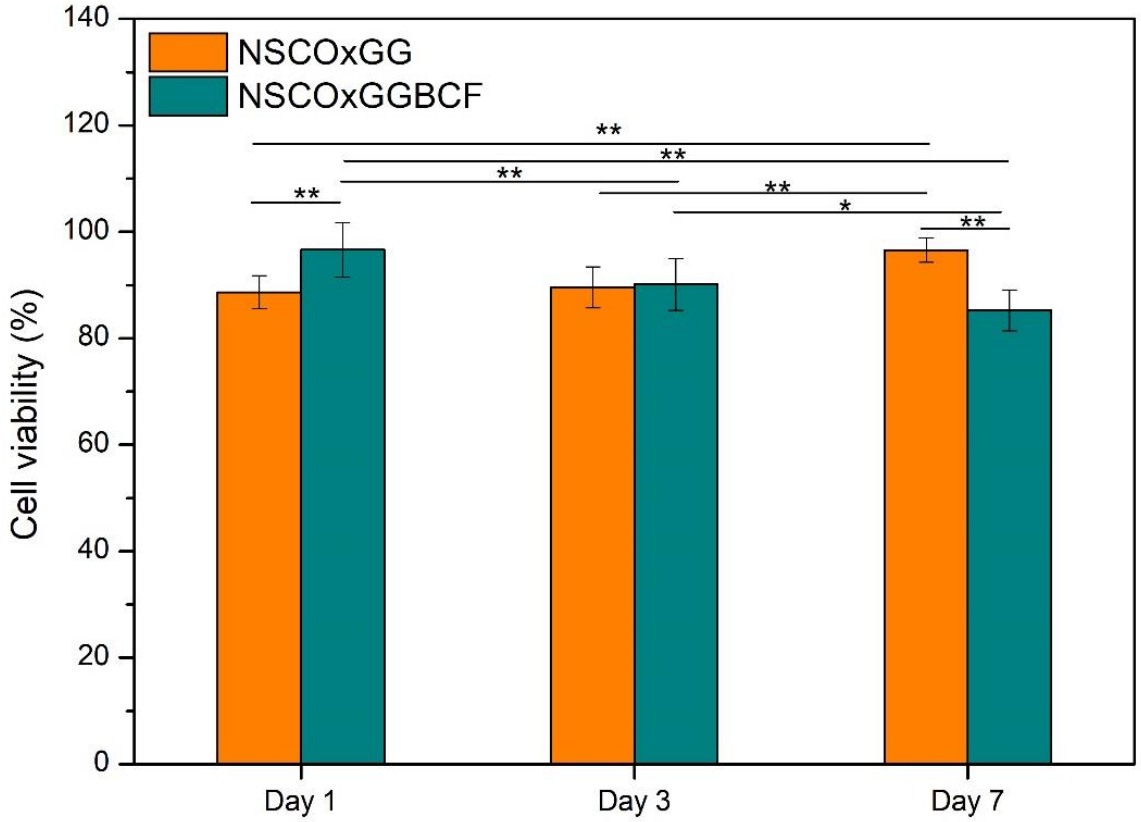

The cellular morphology of nHDF cells can be observed in Figure 50, which shows microscopic images of the *in vitro* culture. The images are coherent with the data shown in Figure 49. All cells exhibited complete adherence and spreading, with very few visible clusters observed throughout the culture substrate. The fibroblasts displayed a healthy and uniform distribution across the surface. These results reinforce the excellent biological performance of the designed formulation, which is fundamental for its biomedical application.

Figure 50 – Microscopic images of the fibroblast cultivated with different time extractives NSC/OxGG and NSC/OxGG/BCF hydrogels

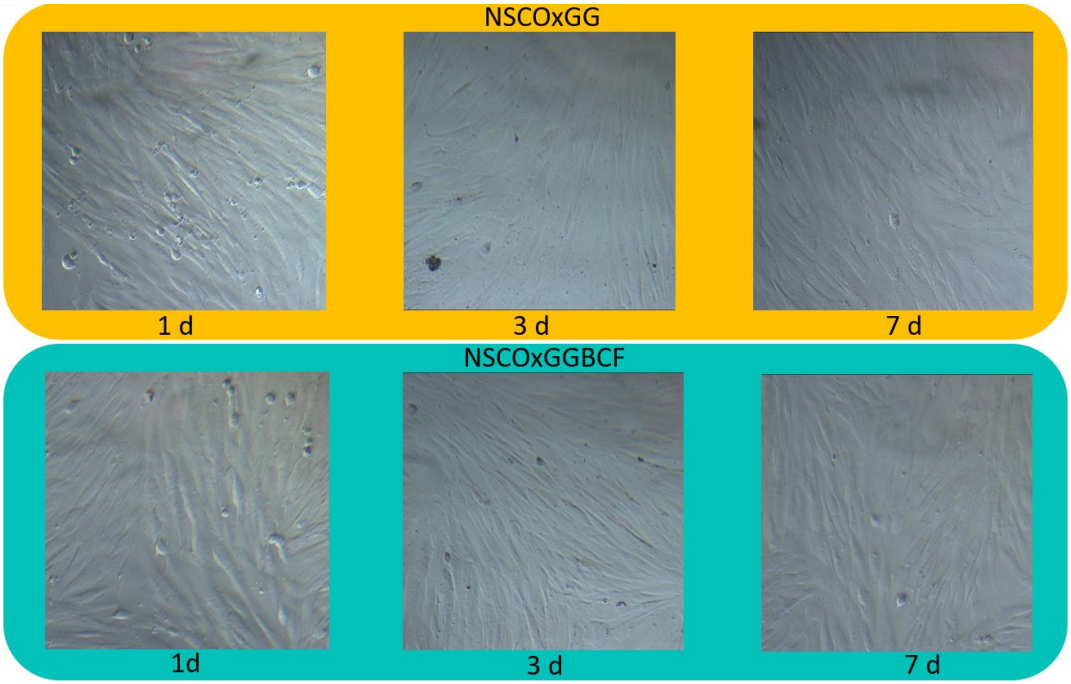

4 CONCLUSION

In this study, we successfully developed BCF-reinforced NSC/OxGG nanocomposite hydrogels using a rapid and safe Schiff base reaction combined with hydrogen bonding crosslinking. The incorporation of BCF in the hydrogels resulted in tunable swelling behavior. The dynamic imine and hydrogen bonds provided synergistic effects that guarantee injectability. Furthermore, incorporating BCF significantly increased the storage and compressive moduli of the hydrogels. In addition to these mechanical improvements, NSC/OxGG/BCF hydrogels demonstrated excellent biocompatibility. These advantageous properties suggest that these novel multifunctional hydrogels hold considerable potential in tissue repair applications.

REFERENCE

ABDUL KHALIL, H. P. *et al.* Cellulosic Nanocomposites from Natural Fibers for Medical Applications: A Review. **Handbook of Polymer Nanocomposites. Processing, Performance and Application: Volume C: Polymer Nanocomposites of Cellulose Nanoparticles**, [*S. l.*], p. 475–511, 2015. Disponível em: https://link.springer.com/chapter/10.1007/978-3-642-45232-1_72. Acesso em: 18 set. de 2024.

ABOUZEID, R. E. *et al.* Biomimetic Mineralization of Three-Dimensional Printed Alginate/TEMPO-Oxidized Cellulose Nanofibril Scaffolds for Bone Tissue Engineering. **Biomacromolecules**, [*S. l.*],v. 19, n. 11, p. 4442–4452, 2018. Disponível em: https://pubs.acs.org/doi/abs/10.1021/acs.biomac.8b01325. Acesso em: 18 set. de 2024.

ADEPU, S. *et al.* Controlled Drug Delivery Systems: Current Status and Future Directions. **Molecules**, [*S. l.*], v. 26, n. 19, p. 5905, 2021. Disponível em: https://www.mdpi.com/1420-3049/26/19/5905/htm. Acesso em: 18 set. 2024.

AHSAN, S. M. *et al.* Chitosan as biomaterial in drug delivery and tissue engineering. **International Journal of Biological Macromolecules**, [*S. l.*], v. 110, p. 97–109, 2018. Disponível em: https://www.sciencedirect.com/science/article/pii/S0141813017318846. Acesso em: 19 set. 2024.

AL HOMSI, R. *et al.* Thermosensitive injectable graphene oxide/chitosan-based nanocomposite hydrogels for controlling the in vivo release of bupivacaine hydrochloride. **International Journal of Pharmaceutics**, [*S. l.*], v. 621, p. 121786, 2022. Disponível em: https://doi.org/10.1016/j.ijpharm.2022.121786. Acesso em: 18 set. 2024.

ALIZADEH-OSGOUEI, M.; LI, Y.; WEN, C. A comprehensive review of biodegradable synthetic polymer-ceramic composites and their manufacture for biomedical applications. **Bioactive Materials**, [*S. l.*], v. 4, p.22-36, 2019. Disponível em: https://doi.org/10.1016/j.bioactmat.2018.11.003 Acesso em: 18 set. 2024.

AZIZ, M. A. *et al.* In vitro biocompatibility and cellular interactions of a chitosan/dextran-based hydrogel for postsurgical adhesion prevention. **Journal of Biomedical Materials Research Part B: Applied Biomaterials**, [*S. l.*], v. 103, n. 2, p. 332–341, 2015. Disponível em: https://onlinelibrary.wiley.com/doi/full/10.1002/jbm.b.33206. Acesso em: 18 set. 2024.

BASHIR, S. *et al.* N-succinyl chitosan preparation, characterization, properties and biomedical applications: A state of the art review. **Reviews in Chemical Engineering**, [*S. l.*], v. 31, n. 6, p. 563–597, 2015. Disponível em: https://doi.org/10.1515/revce-2015-0016. Acesso em: 10 ago. 2024.

BASHIR, S. *et al.* pH responsive N-succinyl chitosan/Poly (acrylamide-co-acrylic acid) hydrogels and in vitro release of 5-fluorouracil. **PLOS ONE**, [*S. l.*], v. 12, n. 7, p. e0179250, 2017. Disponível em: https://journals.plos.org/plosne/article?id=10.1371/journal.pone.0179250. Acesso em: 18 set. 2024.

BASHIR, S. *et al.* Physico-chemical characterization of pH-sensitive N-Succinyl chitosan-g-poly (acrylamide-co-acrylic acid) hydrogels and in vitro drug release studies. **Polymer Degradation and Stability**, [*S. l.*], v. 139, p. 38–54, 2017. Disponível em: https://www.sciencedirect.com/science/article/pii/S014139101730068X. Acesso em: 18 set. 2024.

BASHIR, S. *et al.* Synthesis, characterization, properties of N-succinyl chitosan-g-poly (methacrylic acid) hydrogels and in vitro release of theophylline. **Polymer**, [*S. l.*], v. 92, p. 36–49, 2016. Disponível em: https://www.sciencedirect.com/science/article/pii/S0032386116301859. Acesso em: 10 ago. 2024.

BELLA, F. R.; WIDIYANTI, P.; AMINATUN. The Effect of Glycerol Concentration on Biocomposite Bacterial Cellulose-Chitosan Characterization as Dura Mater Artificial. **Journal of Biomimetics, Biomaterials and Biomedical Engineering**, [*S. l.*], v. 45, p. 40–48, 2020. Disponível em: https://www.scientific.net/JBBBE.45.40. Acesso em: 18 set. 2024.

BIL, M. *et al.* Studies on enzymatic degradation of multifunctional composite consisting of chitosan microspheres and shape memory polyurethane matrix. **Polymer Degradation and Stability**, [*S. l.*], v. 182, p. 109392, 2020. Disponível em: https://doi.org/10.1016/j.polymdegradstab.2020.109392 Acesso em: 18 set. 2024.

BIOLOGICAL EVALUATION OF MEDICAL DEVICES—PART 5: TESTS FOR IN VITRO CYTOTOXICITY. **International Organization for Standardization,** Geneva, Switzerland (ISO 10993-5), 2009. Acesso em: 10 ago. 2024.

BLUME, C. *et al.* Vascular implants – new aspects for in situ tissue engineering. **Engineering in Life Sciences**, [*S. l.*], v. 22, n. 3–4, p. 344–360, 2022. Disponível em: https://onlinelibrary.wiley.com/doi/full/10.1002/elsc.202100100. Acesso em: 18 set. 2024.

CARLOS, C. R. *et al.* Synthesis and characterization of scaffolds produced under mild conditions based on oxidized cashew gums and carboxyethyl chitosan. **International Journal of Biological Macromolecules**, [*S. l.*], v. 176, p. 26–36, 2021. Disponível em: https://doi.org/10.1016/j.ijbiomac.2021.01.178. Acesso em: 18 set. 2024.

CECCALDI, C. *et al.* Validation and application of a nondestructive and contactless method for rheological evaluation of biomaterials. **Journal of Biomedical Materials Research Part B: Applied Biomaterials**, [*S. l.*], v. 105, n. 8, p. 2565–2573, 2017.

Disponível em: https://onlinelibrary.wiley.com/doi/full/10.1002/jbm.b.33797. Acesso em: 18 set. 2024.

CHANDIKA, P. *et al.* Recent advances in biological macromolecule based tissue-engineered composite scaffolds for cardiac tissue regeneration applications. **International Journal of Biological Macromolecules**, [*S. l.*], v. 164, p. 2329–2357, 2020. Disponível em: https://doi.org/10.1016/j.ijbiomac.2020.08.054. Acesso em: 18 set. 2024.

CHEN, C. *et al.* Bacterial cellulose-based biomaterials: From fabrication to application. **Carbohydrate Polymers**, [*S. l.*], v. 278, p. 118995, 2022. Disponível em: https://doi.org/10.1016/j.carbpol.2021.118995. Acesso em: 18 set. 2024.

CHOI, Y. *et al.* Tumor-targeting glycol chitosan nanocarriers: overcoming the challenges posed by chemotherapeutics. **Expert Opinion on Drug Delivery**, [*S. l.*], v. 16, n. 8, p. 835–846, 2019. Disponível em: https://doi.org/10.1080/17425247.2019.1648426. Acesso em: 18 set. 2024.

COSTA, B. R. *et al.* Effectiveness and safety of non-steroidal anti-inflammatory drugs and opioid treatment for knee and hip osteoarthritis: network meta-analysis. **BMJ**, [*S. l.*], v. 375, p. 2321, 2021. Disponível em: https://www.bmj.com/content/375/bmj.n2321. Acesso em: 18 set. 2024.

CUI, S.; ZHANG, S.; COSERI, S. An injectable and self-healing cellulose nanofiber-reinforced alginate hydrogel for bone repair. **Carbohydrate Polymers**, [*S. l.*], v. 300, p. 120243, 2023. Disponível em: https://doi.org/10.1016/j.carbpol.2022.120243. Acesso em: 18 set. 2024.

DALEI, G. *et al.* In situ crosslinked dialdehyde guar gum-chitosan Schiff-base hydrogels for dual drug release in colorectal cancer therapy. **Chemical Engineering Science**, [*S. l.*], v. 269, p. 118482, 2023. Disponível em: https://doi.org/10.1016/j.ces.2023.118482. Acesso em: 18 set. 2024.

DALEI, G.; DAS, S. Carboxymethyl guar gum : A review of synthesis , properties and versatile applications. **European Polymer Journal**, [*S. l.*], v. 176, p. 111433, 2022. Disponível em: https://doi.org/10.1016/j.eurpolymj.2022.111433. Acesso em: 18 set. 2024.

DAVIS, B. *et al.* Entrapping bupivacaine-loaded emulsions in a crosslinked-hydrogel increases anesthetic effect and duration in a rat sciatic nerve block model. **International Journal of Pharmaceutics**, [*S. l.*], v. 588, p. 119703, 2020. Disponível em: https://doi.org/10.1016/j.ijpharm.2020.119703. Acesso em: 18 set. 2024.

DENG, W. *et al.* Cellulose nanofibril as a crosslinker to reinforce the sodium alginate/chitosan hydrogels. **International Journal of Biological Macromolecules**, [*S. l.*], v. 189, p. 890–899, 2021. Disponível em: https://doi.org/10.1016/j.ijbiomac.2021.08.172 Acesso em: 28 ago. 2024.

DING, X. *et al.* A biopolymer hydrogel electrostatically reinforced by amino-functionalized bioactive glass for accelerated bone regeneration. **Science Advances**, [*S. l.*], v. 7, n. 50, p. 7857, 2021. Disponível em: https://www.science.org/doi/10.1126/sciadv.abj7857. Acesso em: 28 ago. 2024.

DWIVEDI, C. *et al.* Chapter 9 - Electrospun Nanofibrous Scaffold as a Potential Carrier of Antimicrobial Therapeutics for Diabetic Wound Healing and Tissue Regeneration. **Nano- and Microscale Drug Delivery Systems: Design and Fabrication**, [*S. l.*], p. 147–164, 2017. Disponível em: https://doi.org/10.1016/B978-0-323-52727-9.00009-1. Acesso em: 28 ago. 2024.

ELDEEB, A. E.; SALAH, S.; ELKASABGY, N. A. Biomaterials for Tissue Engineering Applications and Current Updates in the Field: A Comprehensive Review. **AAPS PharmSciTech**, [*S. l.*], v. 23, n. 7, p. 1–25, 2022. Disponível em: https://link.springer.com/article/10.1208/s12249-022-02419-1. Acesso em: 18 set. 2024.

ELKHOURY, K. *et al.* Biofabrication of natural hydrogels for cardiac, neural, and bone Tissue engineering Applications. **Bioactive Materials**, [*S. l.*], v. 6, n. 11, p. 3904–3923, 2021. Disponível em: https://doi.org/10.1016/j.bioactmat.2021.03.040. 18 set. 2024.

EMAMI, Z. *et al.* Modified hydroxyapatite nanoparticles reinforced nanocomposite hydrogels based on gelatin/oxidized alginate via Schiff base reaction. **Carbohydrate Polymer Technologies and Applications**, [*S. l.*], v. 2, p. 100056, 2021. Disponível em: https://doi.org/10.1016/j.carpta.2021.100056. Acesso em:18 set. 2024.

FAVATELA, F. *et al.* Gelatin/Cellulose nanowhiskers hydrogels intended for the administration of drugs in dental treatments: Study of lidocaine as model case. **Journal of Drug Delivery Science and Technology**, [*S. l.*], v. 61, p. 101886, 2021. Disponível em: https://doi.org/10.1016/j.jddst.2020.101886. Acesso em: 18 set. 2024.

FAVI, P. M. *et al.* Preparation and characterization of biodegradable nano hydroxyapatite–bacterial cellulose composites with well-defined honeycomb pore arrays for bone tissue engineering applications. **Cellulose**, v. 23, n. 2, p. 1263–1282, 2016. Disponível em: https://link.springer.com/article/10.1007/s10570-016-0867-4. Acesso em: 18 set. 2024.

FOLEY, P. L. *et al.* A chitosan thermogel for delivery of ropivacaine in regional musculoskeletal anesthesia. **Biomaterials**, [*S. l.*], v. 34, n. 10, p. 2539–2546, 2013. Disponível em: https://www.sciencedirect.com/science/article/pii/S0142961212014159?via%3Dihub. Acesso em: 10 set. 2024.

FU, L. *et al.* The Application of Bioreactors for Cartilage Tissue Engineering: Advances, Limitations, and Future Perspectives. **Stem Cells International**, [*S. l.*], v. 2021, n. 1, p. 6621806, 2021. Disponível em: https://onlinelibrary.wiley.com/doi/full/10.1155/2021/6621806. Acesso em: 18 set.

2024.

GAHARWAR, A. K.; SINGH, I.; KHADEMHOSSEINI, A. Engineered biomaterials for *in situ* tissue regeneration. **Nature Reviews Materials,** [*S. l.*], v. 5, n. 9, p. 686–705, 2020. Disponível em: https://www.nature.com/articles/s41578-020-0209-x. Acesso em: 18 set. 2024.

GALANTE, Y. M. *et al.* Enzyme oxidation of plant galactomannans yielding biomaterials with novel properties and applications, including as delivery systems. **Applied Microbiology and Biotechnology**, [*S. l.*], v. 102, n. 11, p. 4687–4702, 2018. Disponível em: https://doi.org/10.1007/s00253-018-9028-z. Acesso em: 10 set. 2024.

GAO, L. *et al.* Effects of genipin cross-linking of chitosan hydrogels on cellular adhesion and viability. **Colloids and Surfaces B: Biointerfaces**, [*S. l.*], v. 117, p. 398–405, 2014. Disponível em: https://doi.org/10.1016/j.colsurfb.2014.03.002. Acesso em: 18 set. 2024.

GHAVAMINEJAD, A. *et al.* Crosslinking Strategies for 3D Bioprinting of Polymeric Hydrogels. **Small**, [*S. l.*], v. 16, n. 35, p. 2002931, 2020. Disponível em: https://onlinelibrary.wiley.com/doi/full/10.1002/smll.202002931. Acesso em: 10 set. 2024.

GOMEZ, C. G.; RINAUDO, M.; VILLAR, M. A. Oxidation of sodium alginate and characterization of the oxidized derivatives. **Carbohydrate Polymers**, [*S. l.*], v. 67, n. 3, p. 296–304, 2007. Disponível em: https://doi.org/10.1016/j.carbpol.2006.05.025. Acesso em: 28 ago. 2024.

GU, B.; BURGESS, D. J. Chapter 20 - Polymeric Materials in Drug Delivery. **Natural and Synthetic Biomedical Polymers**, [*S. l.*], p. 333–349, 2014. Disponível em: https://doi.org/10.1016/B978-0-12-396983-5.00021-1. Acesso em: 11 set. 2024.

GUAN, Q. F. *et al.* Sustainable Cellulose-Nanofiber-Based Hydrogels. **ACS Nano**, [*S. l.*], v. 15, n. 5, p. 7889–7898, 2021. Disponível em: https://pubs.acs.org/doi/full/10.1021/acsnano.1c01247. Acesso em: 20 set. 2024.

GUPTA, D. *et al.* Multiscale Porosity in Compressible Cryogenically 3D Printed Gels for Bone Tissue Engineering. **ACS Applied Materials and Interfaces**, [*S. l.*], v. 11, n. 22, p. 20437–20452, 2019. Disponível em: https://pubs.acs.org/doi/abs/10.1021/acsami.9b05460. Acesso em: 20 set. 2024.

HAMA, R. *et al.* Recent Developments in Biopolymer-Based Hydrogels for Tissue Engineering Applications. **Biomolecules**, [*S. l.*], v. 13, n. 2, p. 280, 2023. Disponível em: https://www.mdpi.com/2218-273X/13/2/280/htm. Acesso em: 18 set. 2024.

HATTORI, H. *et al.* Characterization of a water-soluble chitosan derivative and its potential for submucosal injection in endoscopic techniques. **Carbohydrate Polymers**, [*S. l.*], v. 175, p. 592–600, 2017. Disponível em:

https://www.sciencedirect.com/science/article/pii/S0144861717308950. Acesso em: 28 ago. 2024.

HOZUMI, T. *et al.* Injectable Hydrogel with Slow Degradability Composed of Gelatin and Hyaluronic Acid Cross-Linked by Schiff's Base Formation. **Biomacromolecules**, [*S. l.*], v. 19, n. 2, p. 288–297, 2018. Disponível em: https://doi.org/10.1021/acs.biomac.7b01133. Acesso em: 18 set. 2024.

HU, L. *et al.* pH-sensitive carboxymethyl chitosan hydrogels via acid-labile ortho ester linkage for potential biomedical applications. **Carbohydrate Polymers**, v. 178, p. 166–179, 2017. Disponível em: https://doi.org/10.1016/j.carbpol.2019.115237. Acesso em: 18 set. 2024.

HU, W.; WANG, Z.; XIAO, Y. Advances in crosslinking strategies of biomedical hydrogels. **Biomaterials Science**, [*S. l.*], v. 7, p. 843–855, 2019. Disponível em: https://pubs.rsc.org/en/content/articlehtml/2018/bm/c8bm01246f. Acesso em: 18 set. 2024.

HUANG, W. *et al.* Noncompressible Hemostasis and Bone Regeneration Induced by an Absorbable Bioadhesive Self-Healing Hydrogel. **Advanced Functional Materials**, [*S. l.*], v. 31, n. 22, p. 2009189, 2021. Disponível em: https://onlinelibrary.wiley.com/doi/full/10.1002/adfm.202009189. Acesso em: 18 set. 2024.

KARZAR JEDDI, M.; MAHKAM, M. Magnetic nano carboxymethyl cellulose-alginate/chitosan hydrogel beads as biodegradable devices for controlled drug delivery. **International Journal of Biological Macromolecules**, [*S. l.*], v. 135, p. 829–838, 2019. Disponível em: https://doi.org/10.1016/j.ijbiomac.2019.05.21. Acesso em: 18 set. 2024.

KAZACHENKO, A. S. *et al.* Theoretical and experimental study of guar gum sulfation. **Journal of molecular modeling**, [*S. l.*], v. 27, n. 5, p. 1–15, 2021. Disponível em: https://doi.org/10.1007/s00894-020-04645-5. Acesso em:18 set. 2024.

KEAN, T.; THANOU, M. Biodegradation, biodistribution and toxicity of chitosan. **Advanced Drug Delivery Reviews**, [*S. l.*],v. 62, n. 1, p. 3–11, 2010. Disponível em: https://doi.org/10.1016/j.addr.2009.09.004. Acesso em: 18 set. 2024.

KENAWY, E. *et al.* Fabrication of biodegradable gelatin/chitosan/cinnamaldehyde crosslinked membranes for antibacterial wound dressing applications. **International Journal of Biological Macromolecules**, [*S. l.*], v. 139, p. 440–448, 2019. Disponível em: https://doi.org/10.1016/j.ijbiomac.2019.07.191. Acesso em: 18 set. 2024.

KESHARWANI, P. *et al.* Biomedical applications of hydrogels in drug delivery system: An update. **Journal of Drug Delivery Science and Technology**, [*S. l.*], v. 66, p. 102914, 2021. Disponível em: https://doi.org/10.1016/j.jddst.2021.102914. Acesso em: 18 set. 2024.

KHAN, M. U. A. *et al.* Fundamental properties of smart hydrogels for tissue engineering applications: A review. **International Journal of Biological Macromolecules**, [*S. l.*], v. 254, p. 127882, 2024. Disponível em: https://doi.org/10.1016/j.ijbiomac.2023.127882. Acesso em: 18 set. 2024.

KHANAL, M. *et al.* Injectable nanocomposite analgesic delivery system for musculoskeletal pain management. **Acta Biomaterialia**, [*S. l.*], v. 74, p. 280–290, 2018. Disponível em: https://www.sciencedirect.com/science/article/pii/S1742706118303143. Acesso em: 18 set. 2024.

KHUNMANEE, S.; JEONG, Y.; PARK, H. Crosslinking method of hyaluronic-based hydrogel for biomedical applications. **Journal of Tissue Engineering**, [*S. l.*], v. 8, p. 204173141772646, 2017. Disponível em: https://doi.org/10.1177/2041731417726464. Acesso em: 18 set. 2024.

LI, Y. *et al.* Facile design of lidocaine-loaded polymeric hydrogel to persuade effects of local anesthesia drug delivery system: complete in vitro and in vivo toxicity analyses. **Drug Delivery**, [*S. l.*], v. 28, n. 1, p. 1080–1092, 2021. Disponível em: https://www.tandfonline.com/doi/abs/10.1080/10717544.2021.1931558. Acesso em: 18 set. 2024.

LI, J. *et al.* Moist-Retaining, Self-Recoverable, Bioadhesive, and Transparent in Situ Forming Hydrogels to Accelerate Wound Healing. **ACS Applied Materials and Interfaces**, [*S. l.*], v. 12, n. 2, p. 2023–2038, 2020. Disponível em: https://pubs.acs.org/doi/full/10.1021/acsami.9b17180. Acesso em: 18 set. 2024.

LI, Y. *et al.* Physicochemical and pharmacological investigations of polyvinylpyrrolidone - tetrahydroxyborate hydrogel containing the local anesthetic lidocaine. **Journal of Molecular Liquids**, [*S. l.*], v. 335, p. 116526, 2021. Disponível em: https://doi.org/10.1016/j.molliq.2021.116526. Acesso em: 18 set. 2024.

LI, S. *et al.* Self-healing hyaluronic acid hydrogels based on dynamic Schiff base linkages as biomaterials. **Carbohydrate Polymers**, [*S. l.*], v. 250, p. 116922, 2020. Disponível em: https://doi.org/10.1016/j.carbpol.2020.116922. Acesso em: 18 set. 2024.

LI, Q.; MA, L.; GAO, C. Biomaterials for in situ tissue regeneration: development and perspectives. **Journal of Materials Chemistry B**, [*S. l.*], v. 3, n. 46, p. 8921–8938, 2015. Disponível em: https://pubs.rsc.org/en/content/articlehtml/2015/tb/c5tb01863c. Acesso em: 18 set. 2024.

LI, Y.; YANG, H. Y.; LEE, D. S. Advances in biodegradable and injectable hydrogels for biomedical applications. **Journal of Controlled Release**, [*S. l.*], v. 330, p. 151–160, 2021. Disponível em: https://doi.org/10.1016/j.jconrel.2020.12.008. Acesso em: 18 set. 2024.

LIU, C. *et al.* An injectable alginate/fibrin hydrogel encapsulated with cardiomyocytes

and VEGF for myocardial infarction treatment. **Journal of Materials Science & Technology**, [*S. l.*], v. 143, p. 198–206, 2023. Disponível em: https://www.sciencedirect.com/science/article/pii/S1005030222008222. Acesso em: 18 set. 2024.

LIU, J. *et al.* In situ forming hydrogel of natural polysaccharides through Schiff base reaction for soft tissue adhesive and hemostasis. **International Journal of Biological Macromolecules**, [*S. l.*], v. 147, p. 653–666, 2020. Disponível em: https://doi.org/10.1016/j.ijbiomac.2020.01.005. Acesso em: 18 set. 2024.

LIU, Q. *et al.* Rapid gelling, self-healing, and fluorescence-responsive chitosan hydrogels formed by dynamic covalent crosslinking. **Carbohydrate Polymers**, [*S. l.*], v. 246, p. 116586, 2020. Disponível em: https://doi.org/10.1016/j.carbpol.2020.116586. Acesso em: 19 set. 2024.

LOH, Q. L.; CHOONG, C. Three-Dimensional Scaffolds for Tissue Engineering Applications: Role of Porosity and Pore Size. **Tissue Engineering Part B: Reviews**, [*S. l.*], v. 19, n. 6, p. 485–502, 2013. Disponível em: https://www.liebertpub.com/doi/10.1089/ten.teb.2012.0437. Acesso em: 20 set. 2024.

LONČAREVIĆ, A.; IVANKOVIĆ, M.; ROGINA, A. Lysozyme-Induced Degradation of Chitosan: The Characterisation of Degraded Chitosan Scaffolds. **Journal of Tissue Repair and Regeneration**, [*S. l.*], v. 1, n. 1, p. 12–22, 2017. Disponível em: https://openaccesspub.org/tissue-repair-and-regeneration/article/657. Acesso em: 20 set. 2024.

LÜ, S.; LIU, M.; NI, B. An injectable oxidized carboxymethylcellulose/N-succinyl-chitosan hydrogel system for protein delivery. **Chemical Engineering Journal**, [*S. l.*], v. 160, n. 2, p. 779–787, 2010. Disponível em: https://doi.org/10.1016/j.cej.2010.03.07. Acesso em: 20 set. 2024.

LUU, C. H. *et al.* Graphene Oxide-Reinforced Alginate Hydrogel for Controlled Release of Local Anesthetics: Synthesis, Characterization, and Release Studies. **Gels,** [*S. l.]*, v. 8, n. 4, 2022. Disponível em: https://doi.org/10.3390/gels8040246. Acesso em: 20 set. 2024.

MACIEL, J. S. *et al.* Oxidized cashew gum scaffolds for tissue engineering. **Macromolecular Materials and Engineering**, [*S. l.*], v. 304, n. 3, p. 1–11, 2019. Disponível em: https://doi.org/10.1002/mame.201800574. Acesso em: 20 set. 2024.

MAHARJAN, B. *et al.* Regenerated cellulose nanofiber reinforced chitosan hydrogel scaffolds for bone tissue engineering. **Carbohydrate Polymers**, [*S. l.*], v. 251, p. 117023, 2021. Disponível em: https://doi.org/10.1016/j.carbpol.2020.117023. Acesso em: 20 set. 2024.

MANDAL, A. *et al.* Hydrogels in the clinic. **Bioengineering & Translational Medicine**, [*S. l.*], v. 5, n. 2, p. e10158, 2020. Disponível em: https://doi.org/10.1002/btm2.10158. Acesso em: 20 set. 2024.

MATSUMURA, K.; RAJAN, R. Oxidized Polysaccharides as Green and Sustainable Biomaterials. **Current Organic Chemistry**, [*S. l.*], v. 25, n. 13, p. 1483–1496, 2021. Disponível em: https://doi.org/10.2174/1385272825666210428140052. Acesso em: 20 set. 2024.

MEGHEZI, S.; DROUIN, B.; MANTOVANI, D. Collagen hydrogel-based scaffolds for vascular tissue regeneration: Mechanical and viscoelastic characterization. **Characterization of Polymeric Biomaterials**, [*S. l.*], p. 397–439, 2017. Disponível em: https://doi.org/10.1016/B978-0-08-100737-2.00016-9. Acesso em: 20 set. 2024.

MENG, X. *et al.* Chitosan/alginate/hyaluronic acid polyelectrolyte composite sponges crosslinked with genipin for wound dressing application. **International Journal of Biological Macromolecules**, [*S. l.*], v. 182, p. 512–523, 2021. Disponível em: https://doi.org/10.1016/j.ijbiomac.2021.04.044. Acesso em: 20 set. 2024.

MUHAMMAD, M. *et al.* Synthesis and Characterization of Oxidized Polysaccharides for In Situ Forming Hydrogels. **Biomolecules**, [*S. l.*], v. 10, n. 8, p. 1185, 2020. Disponível em: https://www.mdpi.com/2218-273X/10/8/1185/htm. Acesso em: 20 set. 2024.

MUXIKA, A. *et al.* Chitosan as a bioactive polymer: Processing, properties and applications. **International Journal of Biological Macromolecules**, [*S. l.*], v. 105, p. 1358–1368, 2017. Disponível em: https://www.sciencedirect.com/science/article/pii/S0141813017317579. Acesso em: 20 set. 2024.

NAVINDARAN, K.; KANG, J. S.; MOON, K. Techniques for characterizing mechanical properties of soft tissues. **Journal of the Mechanical Behavior of Biomedical Materials**, [*S. l.*], v. 138, p. 105575, 2023. Disponível em: https://doi.org/10.1016/j.jmbbm.2022.105575. Acesso em: 20 set. 2024.

NEZHAD-MOKHTARI, P.; AKRAMI-HASAN-KOHAL, M.; GHORBANI, M. An injectable chitosan-based hydrogel scaffold containing gold nanoparticles for tissue engineering applications. **International Journal of Biological Macromolecules**, [*S. l.*], v. 154, p. 198–205, 2020. Disponível em: https://doi.org/10.1016/j.ijbiomac.2020.03.112. Acesso em: 20 set. 2024.

OLIVEIRA, M. X. *et al.* Hydrogels dressings based on guar gum and chitosan: Inherent action against resistant bacteria and fast wound closure. **International Journal of Biological Macromolecules**, [*S. l.*], v. 253, p. 127281, 2023. Disponível em: https://doi.org/10.1016/j.ijbiomac.2023.127281. Acesso em: 20 set. 2024.

PADMANABHAN, A.; NAIR, L. S. Chitosan hydrogels for regenerative engineering. **Chitin and Chitosan for Regenerative Medicine**, [*S. l.*], p. 3–40, 2015. Disponível em: https://link.springer.com/chapter/10.1007/978-81-322-2511-9_1. Acesso em: 20 set. 2024.

PALLADINO, S. *et al.* Development of a hyaluronic acid—collagen bioink for shear-

induced fibers and cells alignment. **Biomedical Materials**, [*S. l.*], v. 18, n. 6, p. 065017, 2023. Disponível em: https://iopscience.iop.org/article/10.1088/1748-605X/acfd77. Acesso em: 20 set. 2024.

PEERS, S.; MONTEMBAULT, A.; LADAVIÈRE, C. Chitosan hydrogels for sustained drug delivery. **Journal of Controlled Release**, [*S. l.*], v. 326, p. 150–163, 2020. Disponível em: https://doi.org/10.1016/j.jconrel.2020.06.01. Acesso em: 20 set. 2024.

PEREZ, R. A.; MESTRES, G. Role of pore size and morphology in musculo-skeletal tissue regeneration. **Materials Science and Engineering: C**, [*S. l.*], v. 61, p. 922–939, 2016. Disponível em: https://doi.org/10.1016/j.msec.2015.12.087. Acesso em: 20 set. 2024.

PIRES, P. C. *et al.* Polymer-based biomaterials for pharmaceutical and biomedical applications: A focus on topical drug administration. **European Polymer Journal**, [*S. l.*], v. 187, p. 111868, 2023. Disponível em: https://doi.org/10.1016/j.eurpolymj.2023.111868. Acesso em: 20 set. 2024.

QIAO, Q. *et al.* Ropivacaine-loaded, hydroxypropyl chitin thermo-sensitive hydrogel combined with hyaluronan: an injectable, sustained-release system for providing long-lasting local anesthesia in rats. **Regional Anesthesia & Pain Medicine**, [*S. l.*], v. 47, n. 4, p. 234–241, 2022. Disponível em: https://rapm.bmj.com/content/47/4/234. Acesso em: 20 set. 2024.

RAJABI, M. *et al.* Chitosan hydrogels in 3D printing for biomedical applications. **Carbohydrate Polymers**, [*S. l.*], v. 260, p. 117768, 2021. Disponível em: https://doi.org/10.1016/j.carbpol.2021.117768. Acesso em: 20 set. 2024.

RASOOL, A. *et al.* Kinetics and controlled release of lidocaine from novel carrageenan and alginate-based blend hydrogels. **International Journal of Biological Macromolecules**, [*S. l.*], v. 147, p. 67–78, 2020. Disponível em: https://doi.org/10.1016/j.ijbiomac.2020.01.073. Acesso em: 20 set. 2024.

REAKASAME, S.; BOCCACCINI, A. R. Oxidized Alginate-Based Hydrogels for Tissue Engineering Applications : A Review. **Biomacromolecules**, [*S. l.*], v. 19, p. 3–21, 2018. Disponível em: https://pubs.acs.org/doi/full/10.1021/acs.biomac.7b01331

RESSLER, A. Chitosan-Based Biomaterials for Bone Tissue Engineering Applications: A Short Review. **Polymers**, [*S. l.*], v. 14, n.16, p. 3430, 2022. Disponível em: https://doi.org/10.3390/polym14163430. Acesso em: 20 set. 2024.

ROSSI, B. *et al.* Characterization of aerogels from chemo-enzymatically oxidized galactomannans as novel polymeric biomaterials. **European Polymer Journal**, [*S. l.*], v. 93, p. 347–357, 2017. Disponível em: https://www.sciencedirect.com/science/article/pii/S0014305717306031. Acesso em: 20 set. 2024.

SHAH, J.; VOTTA-VELIS, E. G.; BORGEAT, A. New local anesthetics. **Best Practice**

& Research Clinical Anaesthesiology, [*S. l.*], v. 32, n. 2, p. 179–185, 2018. Disponível em: https://www.sciencedirect.com/science/article/pii/S1521689618300570. Acesso em: 20 set. 2024.

SHARIATINIA, Z. Pharmaceutical applications of chitosan. **Advances in Colloid and Interface Science**, [*S. l.*] v. 263, p. 131–194, 2019. Disponível em: https://www.sciencedirect.com/science/article/pii/S000186861830277X. Acesso em: 20 set. 2024.

SIVASHANKARI, P. R.; PRABAHARAN, M. Three-dimensional porous scaffolds based on agarose/chitosan/graphene oxide composite for tissue engineering. **International Journal of Biological Macromolecules**, [*S. l.*], v. 146, p. 222–231, 2020. Disponível em: https://doi.org/10.1016/j.ijbiomac.2019.12.219. Acesso em: 20 set. 2024.

SUN, Y. *et al.* Recent advances of injectable hydrogels for drug delivery and tissue engineering applications. **Polymer Testing**, [*S. l.*], v. 81, p. 106283, 2020. Disponível em: https://www.sciencedirect.com/science/article/pii/S0142941819320811. Acesso em: 20 set. 2024.

TANG, F. *et al.* Preparation and characterization of N-chitosan as a wound healing accelerator. **International Journal of Biological Macromolecules**, [*S. l.*], v. 93, p. 1295–1303, 2016. Disponível em: https://doi.org/10.1016/j.ijbiomac.2016.09.101

THANG, N. H.; CHIEN, T. B.; CUONG, D. X. Polymer-Based Hydrogels Applied in Drug Delivery: An Overview. **Gels,** [*S. l.*], v. 9, n. 7, p. 523, 2023. Disponível em: https://www.mdpi.com/2310-2861/9/7/523/htm. Acesso em: 20 set. 2024.

TU, F. F. Insights gained from a negative trial of steroid blocks for perineal pain. **BJOG: An International Journal of Obstetrics & Gynaecology**, [*S. l.*], v. 124, n. 2, p. 261, 2017. Disponível em: https://doi.org/10.1111/1471-0528.14394. Acesso em: 20 set. 2024.

ULLAH, H. *et al.* Functionalized Bacterial Cellulose Microparticles for Drug Delivery in Biomedical Applications. **Current Pharmaceutical Design**, [*S. l.*], v. 25, n. 34, p. 3692–3701, 2019. Disponível em: https://doi.org/10.2174/1381612825666191011103851. Acesso em: 20 set. 2024.

VAN ZYL, E. M.; COBURN, J. M. Hierarchical structure of bacterial-derived cellulose and its impact on biomedical applications. **Current Opinion in Chemical Engineering**, [*S. l.*], v. 24, p. 122–130, 2019. Disponível em: https://doi.org/10.1016/j.coche.2019.04.005. Acesso em: 20 set. 2024.

VASCONCELOS, N. F. *et al.* Oxidized bacterial cellulose membrane as support for enzyme immobilization: properties and morphological features. **Cellulose**, [*S. l.*], v. 27, p. 3055-3089, 2020. Disponível em: https://doi.org/10.1007/s10570-020-02966-5. Acesso em: 20 set. 2024.

VELEIRINHO, B. *et al.* Manipulation of chemical composition and architecture of non-biodegradable poly(ethylene terephthalate)/chitosan fibrous scaffolds and their effects on L929 cell behavior. **Materials Science and Engineering: C**, [*S. l.*], v. 33, n. 1, p. 37–46, 2013. Disponível em: https://doi.org/10.1016/j.msec.2012.07.047. Acesso em: 20 set. 2024.

WAHID, F. *et al.* Fabrication of Bacterial Cellulose-Based Dressings for Promoting Infected Wound Healing. **ACS Applied Materials and Interfaces**, [*S. l.*], v. 13, n. 28, p. 32716–32728, 2021. Disponível em: https://pubs.acs.org/doi/full/10.1021/acsami.1c06986. Acesso em: 20 set. 2024.

WANG, C. *et al.* Preparation and characterization of apoacynum venetum cellulose nanofibers reinforced chitosan-based composite hydrogels. **Colloids and Surfaces B: Biointerfaces**, [*S. l.*], v. 199, p. 111441, 2021. Disponível em: https://doi.org/10.1016/j.colsurfb.2020.111441. Acesso em: 20 set. 2024.

WANG, K. *et al.* Preparation of bacterial cellulose/silk fibroin double-network hydrogel with high mechanical strength and biocompatibility for artificial cartilage. **Cellulose**, [*S. l.*], v. 27, n. 4, p. 1845–1852, 2020. Disponível em: https://link.springer.com/article/10.1007/s10570-019-02869-0.

WENG, L. *et al.* Non-cytotoxic, in situ gelable hydrogels composed of N-carboxyethyl chitosan and oxidized dextran. **Biomaterials**, [*S. l.*], v. 29, n. 29, p. 3905–3913, 2008. Disponível em: https://doi.org/10.1016/j.biomaterials.2008.06.025. Acesso em: 20 set. 2024.

WU, I. Y. *et al.* Interpreting non-linear drug diffusion data: Utilizing Korsmeyer-Peppas model to study drug release from liposomes. **European Journal of Pharmaceutical Sciences**, [*S. l.*], v. 138, p. 105026, 2019. Disponível em: https://doi.org/10.1016/j.ejps.2019.105026. Acesso em: 20 set. 2024.

WU, M. *et al.* Local anesthetic effects of lidocaine-loaded carboxymethyl chitosan cross-linked with sodium alginate hydrogels for drug delivery system, cell adhesion, and pain management. **Journal of Drug Delivery Science and Technology**, [*S. l.*], v. 79, p. 104007, 2023. Disponível em: https://doi.org/10.1016/j.jddst.2022.104007. Acesso em: 20 set. 2024.

WU, H. *et al.* Regenerated chitin fibers reinforced with bacterial cellulose nanocrystals as suture biomaterials. **Carbohydrate Polymers**, [*S. l.*], v. 180, p. 304–313, 2018. Disponível em: https://doi.org/10.1016/j.carbpol.2017.10.022. Acesso em: 20 set. 2024.

X. JUNPENG, L. YI, H. S. Hydrogels Based on Schi ff Base Linkages for Biomedical Applications. **Molecules**, v. 24, n. 61, p. 1–21, 2019. Disponível em: https://doi.org/10.3390/molecules24163005. Acesso em: 20 set. 2024.

XIN, Y.; YUAN, J. Schiff's base as a stimuli-responsive linker in polymer chemistry. **Polymer Chemistry**, [*S. l.*], v. 3, n. 11, p. 3045–3055, 2012. Disponível em:

https://pubs.rsc.org/en/content/articlehtml/2012/py/c2py20290e. Acesso em: 20 set. 2024.

XING, L. *et al.* Covalently polysaccharide-based alginate/chitosan hydrogel embedded alginate microspheres for BSA encapsulation and soft tissue engineering. **International Journal of Biological Macromolecules**, [*S. l.*], v. 127, p. 340–348, 2019. Disponível em: https://www.sciencedirect.com/science/article/pii/S0141813018343988. Acesso em: 20 set. 2024.

XING, W.; TANG, Y. On mechanical properties of nanocomposite hydrogels: Searching for superior properties. **Nano Materials Science**, [*S. l.*], v. 4, n. 2, p. 83–96, 2022. Disponível em: https://doi.org/10.1016/j.nanoms.2021.07.004. Acesso em: 20 set. 2024.

XUE, H. *et al.* Quaternized chitosan-Matrigel-polyacrylamide hydrogels as wound dressing for wound repair and regeneration. **Carbohydrate Polymers**, [*S. l.*], v. 226, p. 115302, 2019. Disponível em: https://www.sciencedirect.com/science/article/pii/S0144861719309695.

YAN, S. *et al.* Injectable In Situ Self-Cross-Linking Hydrogels Based on Poly(l-glutamic acid) and Alginate for Cartilage Tissue Engineering. **Biomacromolecules**, [*S. l.*], v. 15, n. 12, p. 4495–4508, 2014. Disponível em: https://pubs.acs.org/doi/full/10.1021/bm501313t. Acesso em: 20 set. 2024.

YIN, Z. *et al.* The adsorption behavior of hydroxypropyl guar gum onto quartz sand. **Journal of Molecular Liquids**, [*S. l.*], v. 258, p. 10–17, 2018. Disponível em: https://doi.org/10.1016/j.molliq.2018.02.105. Acesso em: 20 set. 2024.

YU, Z. J. *et al.* A multifunctional hydrogel based on nature polysaccharide fabricated by Schiff base reaction. **European Polymer Journal**, [*S. l.*], v. 197, p. 112330, 2023. Disponível em: https://doi.org/10.1016/j.eurpolymj.2023.112330. Acesso em: 20 set. 2024.

YU, Xiaoshuang *et al.* A self-healing and injectable oxidized quaternized guar gum/carboxymethyl chitosan hydrogel with efficient hemostatic and antibacterial properties for wound dressing. **Colloids and Surface B: Biointerfaces**, [*S. l.], v. 209, p. 112207,* 2022. Disponível em: https://doi.org/10.1016/j.colsurfb.2021.112207. Acesso em: 20 set. 2024.

YU, Y. *et al.* Injectable carboxymethyl chitosan-based hydrogel for simultaneous anti-tumor recurrence and anti-bacterial applications. **International Journal of Biological Macromolecules**, [*S. l.*], v. 230, p. 123196, 2023. Disponível em: https://doi.org/10.1016/j.ijbiomac.2023.123196. Acesso em: 20 set. 2024.

YU, Y. *et al.* Thermo-responsive chitosan/silk fibroin/amino-functionalized mesoporous silica hydrogels with strong and elastic characteristics for bone tissue engineering. **International Journal of Biological Macromolecules**, [*S. l.*], v. 182, p.

1746–1758, 2021. Disponível em: https://doi.org/10.1016/j.ijbiomac.2021.05.166. Acesso em: 20 set. 2024.

ZHAN, Y. *et al.* Advances in versatile anti-swelling polymer hydrogels. **Materials Science and Engineering: C**, [*S. l.*], v. 127, p. 112208, 2021. Disponível em: https://doi.org/10.1016/j.msec.2021.112208. Acesso em: 20 set. 2024.

ZHANG, C. *et al.* Preparation and characterization of carboxymethyl chitosan/collagen peptide/oxidized konjac composite hydrogel. **International Journal of Biological Macromolecules**, [*S. l.*], v. 149, p. 31–40, 2020. Disponível em: https://doi.org/10.1016/j.ijbiomac.2020.01.127. Acesso em: 20 set. 2024.

ZHAO, H.; HEINDEL, N. D. Determination of Degree of Substitution of Formyl Groups in Polyaldehyde Dextran by the Hydroxylamine Hydrochloride Method. **Pharmaceutical Research: An Official Journal of the American Association of Pharmaceutical Scientists**, [*S. l.*], v. 8, n. 3, p. 400–402, 1991. Disponível em: https://link.springer.com/article/10.1023/A:1015866104055. Acesso em: 20 set. 2024.

ZHOU, Y. *et al.* Acidic ionic liquid catalyzed crosslinking of oxycellulose with chitosan for advanced biocomposites. **Carbohydrate Polymers**, [*S. l.*], v. 113, p. 108–114, 2014. Disponível em: https://doi.org/10.1016/j.carbpol.2014.06.081. Acesso em: 20 ago. 2024.

ZHOU, L.-Y. *et al.* Optimized-dose lidocaine-loaded sulfobutyl ether β-cyclodextrin/hyaluronic acid hydrogels to improve physical, chemical, and pharmacological evaluation for local anesthetics and drug delivery systems. **Journal of Materials Science**, [*S. l.*], v. 57, n. 13, p. 7068–7084, 2022. Disponível em: https://doi.org/10.1007/s10853-022-07072-4. Acesso em: 10 set. 2024.

APPENDIX A

Cálculos de grupos funcionais

-CHO groups:
Oxidation degree: 53%
M.M. (Ox GM) = 162 g/mol
In 100 mL Ox GM solution (2.5%):
162 g → 1 mol
2.5 g → x
x = 0.015 mols of CHO

-NH2 groups:
Deacetylation degree: 77%
Substitution degree: 54%
Composition:
23% N-acetyl-β-D-glucosamine = 213 g/mol
35% β-D-glucosamine = 161.2 g/mol
42% N-succinyl-β-D-glucosamine = 260 g/mol

$$\text{M.M. (NSC)} = \frac{(23\times213) + (35\times161.2) + (42\times260)}{100}$$

= 214.6 g/mol

In 100 mL of NSC 2.5% solution:
214.6 g → 1 mol
2.5 g → y
y = 0.012 mol → 100%
z → 35%
z = 4.08×10^{-3} mols of NH_2

25C 75G
$0.25\times4.08\times10^{-3}$ / $0.75\times0.015 \approx 1/10$

50C 50G
$0.5\times4.08\times10^{-3}$ / $0.5\times0.015 \approx 3/10$

75C 25G
$0.75\times4.08\times10^{-3}$ / $0.25\times0.015 \approx 9/10$